REMOTE SENSING OF SEAMOUNTS: A GEOPHYSICAL STUDY OF LITHOSPHERIC FLEXURE, SEAMOUNT STATISTICS AND INTRAPLATE VOLCANISM

A DISSERTATION SUBMITTED TO THE GRADUATE DIVISION OF THE
UNIVERSITY OF HAWAI'I IN PARTIAL FULFILLMENT OF
THE REQUIREMENTS FOR THE DEGREE OF

DOCTOR OF PHILOSOPHY

IN

GEOLOGY AND GEOPHYSICS

DECEMBER 2010

By
Seung-Sep Kim

Dissertation Committee:

Paul Wessel, Chairperson
L. Neil Frazer
Garrett Apuzen-Ito
Mark Merrifield
Scott Rowland
David T. Sandwell, UCSD

We certify that we have read this dissertation and that, in our opinion, it is satisfactory in scope and quality as a dissertation for the degree of Doctor of Philosophy in Geology and Geophysics.

DISSERTATION COMMITTEE

_____
Chairperson

_____

_____

_____

_____

_____

Acknowledgements

First and foremost I would like to thank my advisor Prof. Paul Wessel for his cheerful support and thorough guidance during my PhD and MS. I also would like to thank my committee members, Profs. Garrett Apuzen-Ito, L. Neil Frazer, Scott Rowland, Mark Merrifield, and David T. Sandwell for their unceasing interest and intellectual input. Financial support was provided by National Science Foundation, Student Engagement Grant from the Maui High Performance Computing Center, International Association for Mathematical Geology, and Fred M. Bullard Scholarship. Many thanks are rightfully due to the University of Hawaii, SOEST, and the Department of Geology and Geophysics. Also, special thanks to Michael T. Chandler, O.-S. Lee, S.-G. Kang, C.-E. Kim, C.-E. Shim, and A. Moon, who have always encouraged me during my long-term journey toward a PhD degree at the University of Hawaii. Finally, I would like to express my deepest gratitude to my family for providing love and support from the far east.

Abstract

Seamounts are underwater volcanic constructs that form in three tectonic settings: near-ridge, island-arc, and intraplate environments. While underwater volcanism at ridges and island-arcs is concentrated along these tectonic boundaries, intraplate volcanism is ubiquitous on the seafloor. Locations of seamounts and the lithospheric deformation they cause provide an important window for Earth scientists seeking to understand variations in intraplate volcanism through time and space. Here, I propose a new dense core flexure model that approximates the effect of observed heterogeneous internal seamount structures and develop an automated inversion method to detect and characterize potential seamounts globally from the revised altimetry-derived vertical gravity gradient (VGG) data. The dense core model is first evaluated with analytic solutions derived for plate flexure beneath axisymmetric dense core loads. I confirm that the conventional flexure model with uniform seamount load underestimates elastic thicknesses of the lithosphere by at least 25% for a given dense core load. The dense core model is applied to predict lithospheric flexure beneath Howland Island in the Tokelau seamount chain. After examining synthetic and real cases, I conclude the dense core model approximates the true mass distribution of a seamount better than the uniform density model. Next, I approximate VGG anomalies at seamounts as sums of individual, partially over-lapping, elliptical polynomial functions and form a nonlinear inverse problem that minimizes the misfit between model and observed VGG data. The automated inversion is guided by two model selection criteria (i.e., Akaike Information Criteria and F-tests) that examine the statistical significance of potential seamounts. My global search produced morphology parameters (i.e., height, geographical location, axes of the basal ellipse, and azimuth of its major axis) for 24,643 potential seamounts with height ≥ 0.1 km. Considering the ambiguity of gravity due to small seamounts and the overlap in scale with abyssal

hills, I have tentatively estimated a new global seamount census of 40,000–55,000 ($h \geq 0.1$ km). Finally, I use my new seamount database to estimate the intraplate volcanic budget and explore how the seamount distribution varies with seafloor properties such as age, spreading rate, and spreading direction.

Contents

Acknowledgements **iii**

Abstract **iv**

List of Tables **viii**

List of Figures **xi**

1 Introduction **1**

1.1 Flexure Modeling at Seamounts 4

1.2 New Global Seamount Census from Altimetry-Derived Gravity Data . 5

1.3 Seamount Volcanism and Its Modulation by the Oceanic Lithosphere 6

2 Flexure Modeling at Seamounts **8**

2.1 Introduction 9

2.2 Analytic Solutions for Axisymmetric Dense Core Loads 12

2.3 Flexure and Gravity Calculations with a Dense Core Load 20

2.3.1 Flexure modeling with a dense core load 20

2.3.2 Flexure modeling with gravity data 23

2.3.3 Flexure modeling with arbitrary dense core loads 29

2.4 Case Study: Howland Island 31

2.5 Concluding Remarks 39

3 New Global Seamount Census from Altimetry-Derived Gravity Data **42**

3.1 Introduction 43

3.2 The Vertical Gravity Gradient (VGG) Grid 45

3.3 Methodology 46

3.3.1 VGG potential seamounts 46
3.3.2 Nonlinear inversion for elliptical polynomial seamounts 50
3.3.3 Data noise and statistical model selection 53
3.3.4 SeaHunt: Automated global seamount search 57
3.3.5 Automatic and manual inspections 65
3.3.6 Seamount height estimation 68
3.4 Results 71
3.4.1 Spatial and height distribution of the potential seamounts . . 72
3.5 Discussion 74
3.5.1 New global seamount census 84
3.6 Conclusions 89

4 Seamount Volcanism and Its Modulation by the Oceanic Lithosphere 90
4.1 Introduction 90
4.2 Analysis and Discussion 91
4.3 Conclusions 104

5 Summary and Future Research Directions 105

Bibliography 109

List of Tables

2.1 Parameters used in flexure and gravity calculations. 15

3.1 Number of seamounts identified for each plate-size domain. 75

List of Figures

1.1 Three major tectonic environments associated with underwater volcanism. 3

2.1 Various flexure models. 11

2.2 Axisymmetric dense core loads. 14

2.3 Large dense core loads on an elastic plate of $T_e = 20$ km. 18

2.4 Maximum deflections for various parabolic seamounts. 22

2.5 Comparison of (a) the dense core disc load and (b) stacked two uniform density discs, with $T_e = 20$ km. 24

2.6 Flexure modeling using the gravity anomaly calculated from the dense core parabolic load of Figure 2.2b as the true data. 25

2.7 Comparison of the best models obtained by the uniform density model with the true models. 28

2.8 Observed geophysical data near Howland Island. 31

2.9 Dense core load for Howland Island. 34

2.10 Comparison of the uniform density and dense core models for Howland Island. 35

2.11 Comparison of predicted gravity and flexure along profile AB in Figure 2.9a. 37

2.12 Elastic thickness estimates for Howland Island as a function of age of the lithosphere at the time of loading. 39

3.1 Polynomial seamount model. 49

3.2 Correlation length of the VGG 16.1 grid. 55

3.3 Regional and residual VGG over the Tokelau seamount chain. 58

3.4 Contouring and base polygons. 59

3.5 Automated step-wise inversion for seamount searching. 63
3.6 Full inversion and inspection. 66
3.7 Height estimation from the predicted bathymetry grid, TOPO 12.1 [Smith & Sandwell, 1997]. 70
3.8 Bathymetric basal ellipses of potential seamounts scaled by the height estimation process. 71
3.9 Global distribution of 24,643 potential seamounts identified by this study. 73
3.10 Comparison of potential seamounts identified by this study (red dots) with Wessel [2001] (yellow squares) and Hillier & Watts [2007] (gray triangles) near Tuamotu Plateau. 76
3.11 Height distribution of potential seamounts. 78
3.12 Spatial distribution of the PW|KW potential seamounts of $h > 5$ km in Figure 3.11. 79
3.13 Modeled detectability zones for seamounts using VGG data. 82
3.14 Limitation of topographic separation from gravity over closely spaced small seamounts. 83
3.15 Height-frequency distributions of potential seamounts from KW (red dots), PW (blue open squares), PW|KW (blue squares), HW (gray open triangles), and HW|KW (gray triangles). 84
3.16 Seamount density for small seamounts ($0.1 < h < 1$ km) as a function of the seafloor age. 86
3.17 Bathymetric map coverage over potential seamounts. 88

4.1 Potential seamounts (crosses) and seafloor age distribution. 92
4.2 Histograms of seamounts, basal area, volume, seafloor area, seamount density, and layer thickness as a function of seafloor age. 93
4.3 Variations of small seamount count and sediment thickness as a function of seafloor age. 95

4.4 Potential seamounts (crosses) and half spreading rates. 97
4.5 Histograms of seamounts, basal area, volume, seafloor area, seamount density, and layer thickness as a function of spreading rate. 98
4.6 Potential seamounts (crosses) and spreading direction. 99
4.7 Distinction between circular and elliptical seamounts. 100
4.8 Comparison between azimuth of basal ellipse and spreading direction. 103

Chapter 1

Introduction

A seamount is traditionally defined as "a more or less isolated elevation of the sea floor with a circular or elliptical plan, at least 1 km of relief, comparatively steep slopes, and relatively small summit area" [Menard, 1964]. This traditional height threshold (1 km), chosen to distinguish seamounts from other non-volcanic geologic features (e.g., uplifted abyssal hills), has been revised down to 100 m, depending on the resolution limit of available bathymetry data [e.g., Fornari et al., 1987; Rappaport et al., 1997; Behn et al., 2004]. Whether small or large, seamounts play an important role in the accretion processes of oceanic crust and their spatial and temporal distributions provide crucial information about undersea volcanism and plate kinematics [Wessel, 1997; Koppers & Watts, 2010].

There are three major tectonic environments associated with underwater volcanism: near-ridge, island-arc, and intraplate settings (Figure 1.1). Each tectonic setting exhibits a unique environment for seamount birth and growth. In the near-ridge setting (Figure 1.1b), seamounts tend to be clustered near transform and fracture zones, large overlapping spreading centers, and ridge segments elevated by anomalously abundant magma supply [Batiza, 1982; Fornari et al., 1987; Smith & Cann, 1990]. Most seamounts produced in this environment are small ($<$ 1 km high), while some may continue to grow as they move away with the plate. Such close proximity of seamounts to active spreading boundaries indicates that the structural controls and magma supply systems of the ridge environment largely govern the seamounts formation and growth. Furthermore, the focused distribution of small seamounts implies that the near-ridge underwater volcanism is another important mechanism for oceanic crust accretion, in addition to the generation of crust by seafloor spreading

itself. In the island-arc setting (Figure 1.1c), seamounts and volcanic islands form an arc parallel to the subduction zone, where an oceanic plate subducts beneath the adjacent oceanic plate and produces magma at depth under the overriding plate [Stern, 2002; Tatsumi, 2005].

As such, both near-ridge and island-arc volcanism are genetically linked to particular tectonic boundaries (i.e., ridges and trenches, respectively). Intraplate volcanism (Figure 1.1a), however, is a widespread phenomenon within all plates and hence the spatial distribution of seamounts must be examined carefully to understand the nature of the intraplate volcanism. Multiple mechanisms for intraplate volcanism have been proposed, including upwelling plumes [Courtillot et al., 2003], small-scale sublithospheric convection [Ballmer et al., 2007], and decompressional melting with lithospheric cracking [Forsyth et al., 2006]. Among these tectonic and magmatic causes, the lithosphere has been recognized as a major factor influencing seamount birth and growth in intraplate settings [Vogt, 1974; Batiza, 1982; Wessel, 2001; Hillier, 2007]. Watts [1978] showed that the elastic thickness reflects the thermal age of the lithosphere at the time of seamount emplacement. The elastic thickness of the lithosphere, thus, as inferred via plate flexure modeling, has been used for indirect seamount dating [Watts et al., 2006; Hillier, 2007] because only a small number of seamounts have been dated radiometrically [Clouard & Bonneville, 2005]. Typically, the flexural model used to predict elastic thickness estimates approximates the volcanic load as a simple homogeneous body. In contrast, seismic and geopotential surveys provide unequivocal evidence of a dense core within many seamounts [Robertson, 1967; Minshull & Charvis, 2001; Contreras-Reyes et al., 2010]. Thus, it remains unsettled whether elastic thicknesses estimated with the simple model may be biased significantly.

In this dissertation, I examine the following hypotheses.

- Seamounts, especially larger ones, have a non-uniform density structure that can be inferred from flexural and potential field studies.

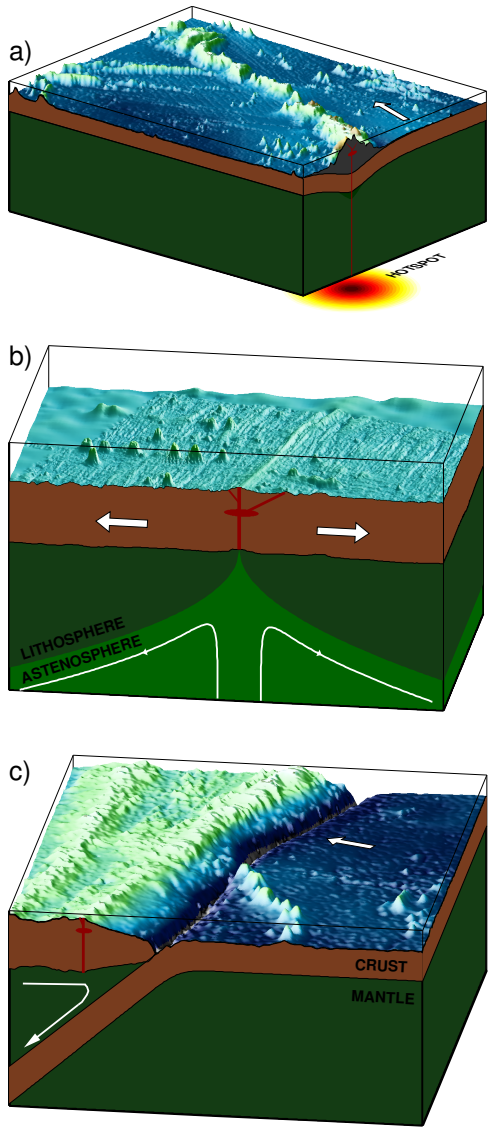

Figure 1.1: Three major tectonic environments associated with underwater volcanism. a) Intraplate volcanism over the Hawaii hotspot. A deep-seated plume feeds the active volcanoes as the plate motion moves the volcanoes away from the hotspot (arrow indicates current direction of plate motion) and forms a linear chain of islands and seamounts . b) Near-ridge volcanism at the East Pacific Rise. Excessive magma is diverted into feeder dikes that sustain seamount formation on ridge flanks. c) Island-arc volcanism in the Kermadec trench. The magma at depth formed by the subducting Pacific plate will eventually erupt to form an arc of volcanoes. Modified from Wessel [2007].

- Improved altimetry data and search algorithms can detect and characterize all seamounts ≥ 1 km tall.

- Initial intraplate volcanism makes the lithosphere more susceptible to later volcanic overprinting [Hillier, 2007].

- There are simple relationships between seamount locations and the age, spreading rate, and spreading direction of the seafloor.

The above hypotheses are tested and explored in the following chapters. Here, I briefly introduce the main topics of each chapter.

1.1 Flexure Modeling at Seamounts

In chapter 2, I develop a flexure model that includes a dense core inside an axisymmetric seamount. Seismic and gravity surveys over several seamounts have revealed that seamounts (including volcanic islands) do not have a homogeneous density structure [Ishihara, 1987; Kellogg et al., 1987; Hildebrand et al., 1989b; Contreras-Reyes et al., 2010]. In flexure modeling, however, such an inhomogeneous body is often approximated as a homogeneous construct [Lambeck & Nakiboglu, 1980; Kruse et al., 1997; Ali et al., 2003], which may distort elastic thickness estimates. Although this possibility has been raised previously [Minshull & Charvis, 2001], no one has investigated in detail the effects of dense cores on the estimation of elastic plate thicknesses. Therefore, in this chapter, I assess the effects of dense cores on flexure modeling and develop an efficient modeling approach, in order to address the following questions:

- Is the uniform density seamount an adequate model or must a dense core be included?

- What is the effect of a dense core on elastic plate thickness estimates?

- How accurate are seamount ages inferred from seamount gravity alone?

As a starting point, I find the analytic solutions for disc and parabolic loads having dense cores and examine the model predictions using various synthetic cases. I also propose a practical application of the dense core model by constructing a uniform density load of the same mass as the dense core model. This approximation allows us to compute the flexural deflection and gravity anomaly of a seamount in the wavenumber domain and minimize the limitations recognized from the analytic tests. Finally, the dense core model is applied to predict the lithospheric flexure beneath Howland Island in the Tokelau seamount chain, showing that the elastic thickness there is underestimated when the uniform model is employed.

1.2 New Global Seamount Census from Altimetry-Derived Gravity Data

Statistical studies of seamount distributions have previously relied on counting the isolated peaks of bathymetric charts [e.g., Batiza, 1982] and have focused mainly on the mid-ocean ridge environment [e.g., Fornari et al., 1987; Smith & Cann, 1990; Rappaport et al., 1997]. Because ship soundings cover only a small fraction of the world's ocean [Becker et al., 2009], the uniform coverage provided by satellite altimetry has been a key reason to investigate global seamount distributions using such remotely-sensed data [e.g., Craig & Sandwell, 1988; Wessel, 1997]. Recently, the resolution of altimetry-derived gravity data has been improved by a factor of two following a rigorous re-tracking of the original radar altimetry waveforms [Sandwell & Smith, 2005, 2009]. Therefore, this is a very opportune time to re-evaluate the global distribution of seamounts using the newly revised satellite-derived vertical gravity gradient (VGG) data and to explore the wider geophysical significance of seamounts in reflecting spatial and temporal aspects of intraplate volcanism.

In Chapter 3, I develop a non-linear inversion method to detect and characterize seamounts from the new VGG 16.1 data, which reveal more detail of the seafloor than previous releases. VGG anomalies over seamounts are approximated as sums of individual, partially over-lapping, elliptical polynomial functions in order to form a nonlinear inverse problem that minimizes the misfit between the polynomial seamount model and observed VGG data. In addition, I use two model selection criteria, Akaike Information Criterion and F-tests, to evaluate statistical significance of potential seamounts. Then, a step-wise and fully automated inversion is executed to find potential seamounts globally from the VGG grid; minor manual inspection was then performed to weed out special cases.

Using the new global seamount database, I address the following questions in Chapter 3:

- Does the size-frequency distribution of seamounts follow an exponential or power-law curve? Can such an empirical statistical model predict the "true" global seamount census?
- Can I reconcile the global seamount distribution from this study with the previous global studies [Wessel, 2001; Kitchingman & Lai, 2004; Hillier, 2007]?
- Can I automatically separate volcanic ridges from seamounts?

1.3 Seamount Volcanism and Its Modulation by the Oceanic Lithosphere

In Chapter 4, I make a first-order analysis that compares geometric quantities (e.g., height and volume) determined from the new global seamount database with seafloor age and examines the variation of underwater volcanism since the Upper Jurassic. In addition, orientations of the basal ellipses of detected seamounts are compared with

the spreading directions at the time of seafloor formation in order to examine the correlation, if any, between seafloor fabric and the orientation of seamounts. Using the new digital grids of age and spreading rate [Müller et al., 2008], I address the following questions in Chapter 4:

- How many global pulses in seamount production have been recorded?
- Is the seafloor formed by fast spreading more susceptible to seamount volcanism than that formed by intermediate and slow spreading?
- Are the orientations of elongated seamounts determined by the pre-existing seafloor fabrics?

Chapter 2

Flexure Modeling at Seamounts

This chapter was published as

Kim, S.-S., and P. Wessel (2010), Flexure modelling at seamounts with dense cores, *Geophys. J. Int.*, 182, 583-598.

The lithospheric response to seamounts and ocean islands has been successfully described by deformation of an elastic plate induced by a given volcanic load. If the shape and mass of a seamount are known, the lithospheric flexure due to the seamount is determined by the thickness of an elastic plate, T_e, which depends on the load density and the age of the plate at the time of seamount construction. We can thus infer important thermo-mechanical properties of the lithosphere from T_e estimates at seamounts and their correlation with other geophysical inferences, such as cooling of the plate. Whereas the bathymetry (i.e., shape) of a seamount is directly observable, the total mass often requires an assumption of the internal seamount structure. The conventional approach considers the seamount to have a uniform density (e.g., density of the crust). This choice, however, tends to bias the total mass acting on an elastic plate. In this study, I will explore a simple approximation to the seamount's internal structure that considers a dense core and a less dense outer edifice. Although the existence of a core is supported by various gravity and seismic studies, the role of such volcanic cores in flexure modeling has not been fully addressed. Here, I present new analytic solutions for plate flexure due to axisymmetric dense core loads and use them to examine the effects of dense cores in flexure calculations for a variety of synthetic cases. Comparing analytic solutions with and without a core indicates that the flexure model with uniform density underestimates T_e by at least 25%. This bias

increases when the uniform density is taken to be equal to the crustal density. I also propose a practical application of the dense core model by constructing a uniform density load of same mass as the dense core load. This approximation allows me to compute the flexural deflection and gravity anomaly of a seamount in the wavenumber domain and minimize the limitations recognized from the analytic tests. Then, the dense core model is applied to predict the lithospheric flexure beneath Howland Island in the Tokelau seamount chain; these results are compared with the predictions of the uniform density model. Based on age dating of Howland and the age of the seafloor, traditional T_e vs age curves predict the elastic plate thickness beneath the seamount to be around 20 km, which is comparable to the best dense core model of $T_e = 26$ km. However, the best uniform density model is found at $T_e = 12$ km, which is significantly less than the predicted. From my investigations of synthetic and real seamount cases, I conclude that the dense core model approximates the true mass distribution of a seamount better than the uniform density model. Finally, I suggest that the role of underplating in flexure modeling may need to be reexamined because the dense core model predicts substantially less deflections than the uniform density model without requiring additional buoyancy caused by underplated material.

2.1 Introduction

How the lithosphere responds to geologic loads (e.g., ice sheets and seamounts) has been modeled using an elastic plate that can flex downward to support a given load [Watts, 2001]. The mechanical behavior of elastic lithosphere is then simply expressed in terms of the elastic plate thickness, T_e. Numerous studies have been carried out in order to understand lithospheric deformation of the oceanic crust, especially beneath seamounts and ocean islands [e.g., Walcott, 1970; McNutt & Menard, 1978; Watts, 1978; Calmant, 1987; Wolfe & McNutt, 1991; Wessel, 1993; Collier & Watts, 2001;

Adam & Bonneville, 2008]. As T_e depends on the age of the oceanic plate at the time of volcanic construction (Δt), the relationship between T_e and Δt has been widely applied to determine apparent ages of seamounts [e.g., Calmant et al., 1990; Watts et al., 2006; Hillier, 2007]. In addition, new roles of the lithosphere in influencing the location of intraplate volcanism [Hillier, 2007] and limiting the growth of seamounts [Wessel, 2001] have been recently proposed.

T_e at seamounts can be estimated by different methods with various geophysical data [e.g., Wessel, 1996; Ramillien & Mazzega, 1999; Grevemeyer et al., 2001; Adam & Bonneville, 2008]. However, a uniform seamount density structure is commonly assumed regardless of modeling approach. This uniform density model simplifies gravity anomaly prediction by requiring the density of materials inside the flexural moat and the density of the seamount to be the same (Figures 2.1a and 2.1b). The gravity anomaly is linearly proportional to the density contrast between two materials, which becomes constant along each boundary between the different materials assumed in the uniform density model. For example, the flexed crust in Figure 2.1a defines the boundary between the uniform load and the crust with a density contrast of $\rho_c - \rho_l$. If one assumes $\rho_l = \rho_c$, this flexed crust boundary is no longer needed for gravity prediction and hence the modeling becomes further simplified. The preferred choice for ρ_l, thus, has been the oceanic crustal density of 2800 kg m^{-3} [e.g., McNutt & Menard, 1978; Calmant, 1987]. In reality, the flexural moats that flank seamounts and oceanic islands are filled with a mixture of volcanic, erosional, and sedimentary materials and hence the peripheral (or moat) materials are less dense than the seamount itself. If one selects a peripheral density, ρ_s, that differs from the seamount density, ρ_t, then the flexed crust boundary exhibits a radial variation of density contrasts (i.e., $\rho_c - \rho_t$ beneath the seamount and $\rho_c - \rho_s$ inside the moat). Although this two-boundary model (Figure 2.1b) complicates gravity prediction, it is more realistic than the uniform density model [e.g., Smith et al., 1989; Wessel, 2001].

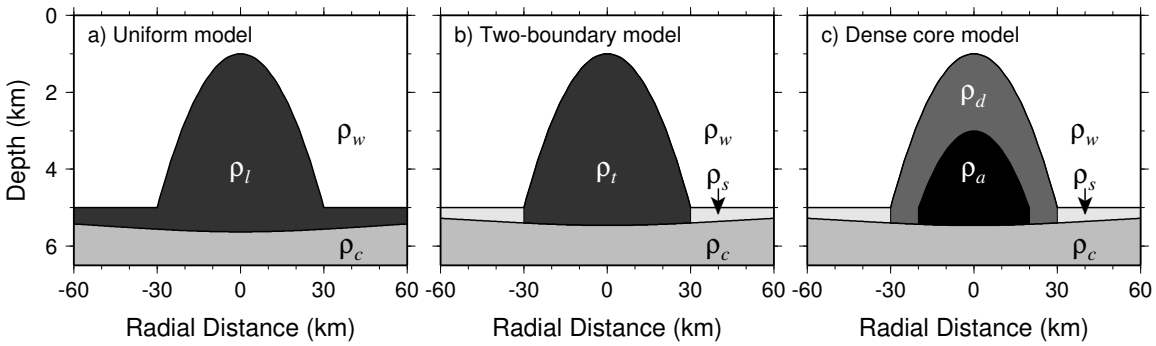

Figure 2.1: Various flexure models. (a) Uniform density model assumes all loading parts have a constant density, ρ_l, which can be fixed as the crustal density or determined by minimizing the misfits. (b) In the two-boundary model [Wessel, 2001], the peripheral density, ρ_s differs from the seamount density, ρ_t. (c) Dense core model. In this study, I separate the seamount body into the outer edifice (with density ρ_d) and the inner core (with density ρ_a), which reflect both geological (see Figure 15 in Staudigel & Schmincke [1984]) and geophysical (see Figure 2 in Minshull & Charvis [2001]) observations of internal seamount structure.

Many detailed gravity [e.g., Robertson, 1967; Kellogg et al., 1987; Hammer et al., 1991; Araña et al., 2000; Camacho et al., 2009] and seismic [e.g., Hildebrand et al., 1989a; Watts et al., 1997; Gallart et al., 1999; Weigel & Grevemeyer, 1999; Kopp et al., 2004; Contreras-Reyes et al., 2010] surveys have provided evidence of dense cores inside seamounts and ocean islands. Interestingly, such dense cores have only been considered when computing gravity anomalies due to the volcanic construct, but not when estimating the flexural deformation beneath it. Yet, lithospheric deformation is often modeled by minimizing the differences between the observed and predicted gravity anomalies. Furthermore, many tools for computing gravity signals due to arbitrary bodies are available [e.g., Talwani & Ewing, 1960; Nagy, 1966; Plouff, 1976; Blakely, 1996], but no methodology has been developed for flexure modeling with a dense core. There is a possibility that the uniform seamount assumption distorts the flexure analysis, and may in turn bias the results toward low T_e estimates [Minshull & Charvis, 2001]. Exploring such a possibility is long overdue.

In this study, I propose a new dense core seamount model incorporating a core that is denser than the seamount edifice (Figure 2.1c) and its practical application

to predict flexure and gravity at seamounts. For direct comparison between different seamount models in Figure 2.1, I first derive analytic solutions for plate flexure due to axisymmetric dense core loads. Then, I explore the differences between these models using various synthetic loads and a case study of lithospheric flexure beneath Howland Island in the northern Tokelau seamount chain.

2.2 Analytic Solutions for Axisymmetric Dense Core Loads

As a first-order approximation to realistic internal seamount structures [Staudigel & Schmincke, 1984; Minshull & Charvis, 2001], I first construct axisymmetric disc and parabolic loads that have dense cores at their centers. Then, following previous studies [Brotchie & Silvester, 1969; Brotchie, 1971; Lambeck & Nakiboglu, 1980], the governing equation for the deflection, $w(r)$, of an elastic plate of flexural rigidity, D, on an inviscid fluid due to an axisymmetric load, $q(r)$, is given as

$$D\nabla^4 w(r) + \rho_m g w(r) = q(r), \tag{2.1}$$

with

$$\nabla^2 \equiv \frac{d^2}{dr^2} + \frac{1}{r}\frac{d}{dr} \tag{2.2}$$

and

$$D = \frac{ET_e^3}{12(1-\nu^2)}. \tag{2.3}$$

The parameters not mentioned in the text are listed in Table 2.1. In eq. (2.1), the right-hand side is the driving force flexing the elastic plate downward, whereas the terms on the left-hand side represent the resisting forces arising from the finite strength of the plate (first term) and the buoyancy of the mantle (second term).

Through the balance between these forces, geological features achieve isostasy [Watts, 2001].

In order to simplify the derivation, I assume that the dense core has the same shape as the edifice. The density variations of each part in the dense core disc and parabolic loads are denoted as the core density, ρ_a, the edifice density, ρ_d, and the peripheral density, ρ_s, respectively (Figure 2.2a). For further simplification, I assume that the flexural moat is completely filled only up to the originally undeformed plane (i.e., the reference level in Figure 2.2a). Also, it is mathematically convenient to divide the load, $q(r)$, into two components: one above the reference level and the other between the reference level and the flexed crust (Figure 2.2). To be concise, I use "surface" for any loading materials above the reference level and "subsurface" for materials between the reference level and the flexed crust. The amount of subsurface materials, therefore, becomes a function of the deflection, $w(r)$. In flexure modeling, however, the term "infill" has been widely used to describe this subsurface material as it infills the flexed crust [Watts, 2001]. The uniform density model allows the infill density to differ from the density of the topographic feature above the reference level, however the model still requires a uniform density for the infill material [e.g., Hillier, 2007]. Although such separation between the surface and subsurface materials can lead to better gravity and flexure predictions, it is incongruent with geological views on seamount growth [Staudigel & Schmincke, 1984; Minshull & Charvis, 2001]. Thus, the subsurface material in the dense core model changes radially from the core material beneath the core, the edifice material beneath the edifice, and the material inside the flexural moat (Figure 2.2). This radial change of subsurface load requires me to divide $q(r)$ into three parts: the first for the radial extent of the core at $0 \leq r \leq r_a$, the second only under the edifice at $r_a \leq r \leq r_d$, and the third extending beyond the edge of seamount at $r \geq r_d$ (while the uplifted bulge represents yet another domain, I cannot include it in an analytic solution). The dense core disc and parabolic loads,

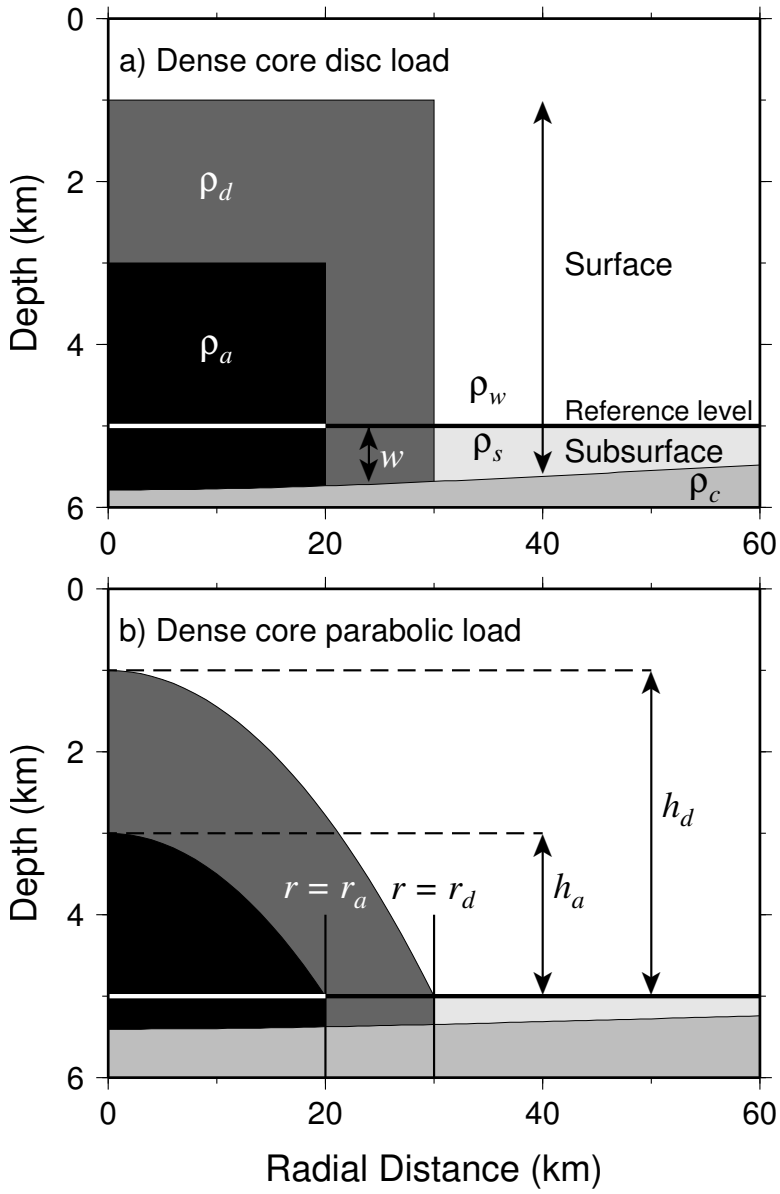

Figure 2.2: Axisymmetric dense core loads. (a) Dense core disc load with labels for the core (ρ_a), edifice (ρ_d), peripheral (ρ_s), water (ρ_w), and crust (ρ_c). (b) Dense core parabolic load with labels for the physical dimensions (i.e., height and radius) of the core and the edifice. The surface load is the mass above the reference level (thick solid line) and the subsurface load is the mass between the reference level and the flexed crust, which depends on flexure, w.

Table 2.1: Parameters used in flexure and gravity calculations.

Parameter	Description	Value	Unit
ρ_d	Edifice density	2500	kg m^{-3}
ρ_s	Peripheral density	2300	kg m^{-3}
ρ_a	Core density	2900	kg m^{-3}
ρ_m	Mantle density	3300	kg m^{-3}
ρ_c	Crust density	2800	kg m^{-3}
ρ_w	Water density	1000	kg m^{-3}
ν	Poisson's ratio	0.25	
E	Young's modulus	10^{11}	Pa
g	Normal gravity	9.81	m s^{-2}
G	Gravitational constant	6.673×10^{-11}	m^3 kg^{-1} s^{-2}

$q_D(r)$ and $q_P(r)$ respectively, are defined as follows:

$$q_D(r) = \begin{cases} \rho_a g[h_a + w(r)] + \rho_d g(h_d - h_a) - \rho_w g h_d & 0 \le r \le r_a \\ \rho_d g[h_d + w(r)] - \rho_w g h_d & r_a \le r \le r_d, \\ \rho_s g w(r) & r \ge r_d \end{cases} \tag{2.4}$$

and

$$q_P(r) = \begin{cases} \rho_a g[t_a(r) + w(r)] + \rho_d g[t_d(r) - t_a(r)] - \rho_w g t_d(r) & 0 \le r \le r_a \\ \rho_d g[t_d(r) + w(r)] - \rho_w g t_d(r) & r_a \le r \le r_d, \\ \rho_s g w(r) & r \ge r_d \end{cases} \tag{2.5}$$

with the parabolas of the core and the edifice defined as

$$t_x(r) = h_x(1 - r^2/r_x^2) \quad \{x = a, d\}. \tag{2.6}$$

The heights of the edifice and the core are measured relative to the reference level (Figure 2.2b).

When the shape of the surface load is relatively simple and axisymmetric, the homogenous solution to eq. (2.1) becomes a combination of Bessel-Kelvin functions [Brotchie & Silvester, 1969; Lambeck & Nakiboglu, 1980]. This solution is also valid

for the dense core loads because both the core and the edifice have the same axisymmetric shape. By equating eq. (2.1) with eqs. (2.4) and (2.5), I obtain the particular solutions using the method of undetermined coefficients. Customarily, the general solution for a non-homogeneous equation is a sum of the homogeneous and particular solutions that contain every solution satisfying eq. (2.1) over the interval of interest. In flexure modeling, the general solution (i.e., deflection) for eq. (2.1) must satisfy the following boundary conditions for continuity at each boundary, where the loading material changes (Figure 2.2b):

Condition 1. At $r = 0$, dw/dr and shear stress are finite.

Condition 2. At $r = r_a$, w, dw/dr, bending moments, and shear stresses are continuous.

Condition 3. At $r = r_d$, w, dw/dr, bending moments, and shear stresses are continuous.

Condition 4. At infinity, w and dw/dr vanish.

Here, the corresponding axisymmetric bending moments, $M(r)$, and shear stresses, $Q(r)$, are given by

$$M(r) = -D\left(\frac{d^2w}{dr^2} + \nu\frac{1}{r}\frac{dw}{dr}\right) \tag{2.7}$$

and

$$Q(r) = -D\frac{d}{dr}\nabla^2 w. \tag{2.8}$$

With boundary conditions 1 and 4 applied, the analytic solution to eq. (2.1) with the dense core disc load is reduced to

$$w_D(r) = \begin{cases} \alpha[1 + C_1\mathrm{ber}(k_a r) + C_2\mathrm{bei}(k_a r)] & 0 \le r \le r_a \\ \beta[1 + C_3\mathrm{ber}(k_d r) + C_4\mathrm{bei}(k_d r) + C_5\mathrm{ker}(k_d r) + C_6\mathrm{kei}(k_d r)] & r_a \le r \le r_d, \\ \beta[C_7\mathrm{ker}(k_s r) + C_8\mathrm{kei}(k_s r)] & r \ge r_d \end{cases} \tag{2.9}$$

where

$$\alpha = [h_a(\rho_a - \rho_d) + h_d(\rho_d - \rho_w)]/(\rho_m - \rho_a),$$
$$\beta = h_d(\rho_d - \rho_w)/(\rho_m - \rho_d), \tag{2.10}$$

and C_1 – C_8 are non-zero integration constants. Here, ber, bei, ker, and kei are Bessel-Kelvin functions of zero order [Abramowitz & Stegun, 1970], and k_a, k_d, and k_s are the radial flexural wave numbers defined as

$$k_x = \left[\frac{(\rho_m - \rho_x)g}{D}\right]^{1/4} \quad \{x = a, d, s\}. \tag{2.11}$$

These flexural wave numbers result from the radial change of subsurface material. The eight arbitrary constants in eq. (2.9) are evaluated numerically by applying boundary conditions 2 and 3.

Similarly, the analytic solution to eq. (2.1) with the dense core parabolic load is obtained as

$$w_P(r) = \begin{cases} \eta[t_a(r)(\rho_a - \rho_d) + t_d(r)(\rho_d - \rho_w) + C_1\mathrm{ber}(k_a r) + C_2\mathrm{bei}(k_a r)] & 0 \le r \le r_a \\ \zeta[t_d(r) + C_3\mathrm{ber}(k_d r) + C_4\mathrm{bei}(k_d r) + C_5\mathrm{ker}(k_d r) + C_6\mathrm{kei}(k_d r)] & r_a \le r \le r_d, \\ \zeta[C_7\mathrm{ker}(k_s r) + C_8\mathrm{kei}(k_s r)] & r \ge r_d \end{cases} \tag{2.12}$$

where

$$\eta = 1/(\rho_m - \rho_a) \tag{2.13}$$

and

$$\zeta = (\rho_d - \rho_w)/(\rho_m - \rho_d). \tag{2.14}$$

Boundary conditions 2 and 3 are also applied for the numerical determination of C_1 – C_8. For the sake of minimizing symbols, I keep the same subscript numbers of Cs in eq. (2.12) as in eq. (2.9), but their values are different. Although these constants can be evaluated analytically, the analytic solutions become arduous and it is simpler

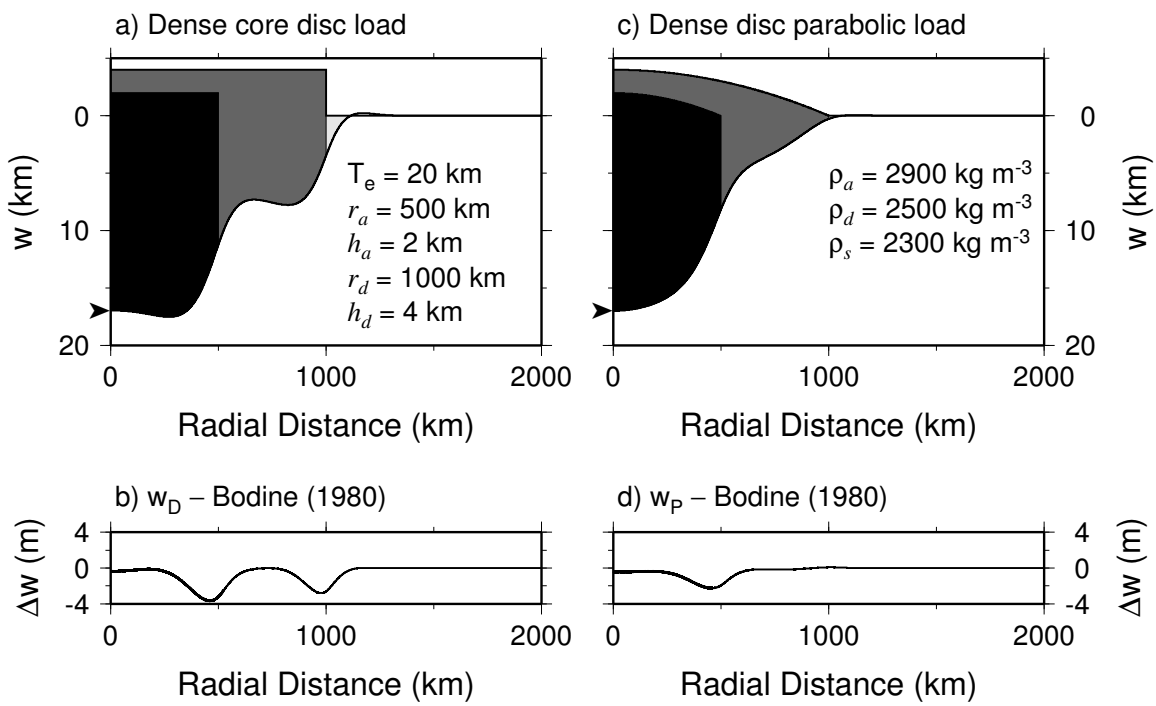

Figure 2.3: Large dense core loads on an elastic plate of $T_e = 20$ km. Analytic deflections due to the dense core (a) disc and (c) parabolic loads are compared with the numerical deflections of Bodine [1980]. The arrows in (a) and (c) indicate the expected Airy-type flexural response for the applied dense core loads. (b) and (d) are the differences between the analytic and Bodine solutions and show a good agreement.

to assess them numerically.

I verify the analytic solutions for plate flexure due to the dense core loads in three different ways. First, a case of no core (i.e., $\rho_a = \rho_d$) is considered. Then, eqs. (2.9) and (2.12) must be equal to the solutions of Lambeck & Nakiboglu [1980]. With no core, the first boundary in the dense core load presents no change in parameters and hence the analytic solution for the first boundary condition is not needed. While boundary condition 1 requires C_5 and C_6 to be zero, boundary condition 3 is necessary to determine the other constants. Therefore, I obtain the same solutions as Lambeck & Nakiboglu [1980]. This verification proves that my derivation is correct.

Second, when the surface load is very large ($r_d > 500$ km), the lithosphere becomes very weak compared to the given load and exhibits an Airy-type flexural response regardless of elastic plate thickness [Watts, 2001]. In an Airy-type flexural response,

the maximum deflection directly underneath the dense core loads in Figure (2.2) becomes linearly proportional to the mass balance between the surface loads (i.e., the core and the edifice) and the portion of the mantle displaced by the core; it is 17 km for the given dense core loads. To examine if my analytic solutions satisfy this simple physics, I increase only the radii of the edifice and the core and fix all other parameters including T_e as in Figure 2.2; the core radius is half the edifice radius. From Figures 2.3a and 2.3c, I find that both analytic solutions result in the expected value. The stair-case feature in Figure 2.3a occurs because the edifice itself is large enough to attain its own Airy-type flexural response.

Last, I compare the analytic solutions directly with the numerical solution of Bodine [1980] using the dense core loads in Figure 2.3. For the Bodine solution, the surface load is approximated by stacking the edifice and the core together so that the total mass of the stacked parts is equal to that of the dense core load above the reference level. In addition, the Bodine solution is adapted to include the subsurface material changes at $r = r_a$ and $r = r_d$. Both the analytic and Bodine solutions are constrained by the boundary conditions listed above. Figures 2.3b and 2.3d show the remainders after subtracting the numerically calculated deflections from the analytical ones. Except the minimal differences ($< 10^{-4}$), both solutions exhibit a good agreement. Therefore, I conclude that the analytic solutions for plate flexure derived with the axisymmetric dense core loads are valid. Next, I will explore how the dense core model differs from the uniform density model when used to predict deflections and the gravity anomalies using various synthetic data.

2.3 Flexure and Gravity Calculations with a Dense Core Load

2.3.1 Flexure modeling with a dense core load

The total mass of a uniform density load (i.e., the driving force) depends mainly on the choice of density. Although the detailed internal structure of seamounts can be constrained by, or inferred from, other data (e.g., seismic data), the load density, ρ_l, has often been presumed to equal the crustal density (i.e., Figure 2.1a with $\rho_l = \rho_c$). However, this choice tends to overestimate the driving force. For example, if I compare the dense core parabolic load in Figure 2.2b with a uniform parabolic load of same size and of crustal density, the mass above the reference level for the latter becomes 40% heavier than that for the former. Because of the overestimated mass, the uniform density model results in more flexure relative to the dense core model for the same T_e. If we consider the parabolic seamount (i.e., bathymetry) in Figure 2.2b and the flexure produced by the dense core load as the observed data, the uniform density model requires a thicker elastic plate (larger T_e) in order to compensate for the overestimated load [Minshull & Charvis, 2001]. Therefore, a careful consideration of the load density is necessary to prevent overestimating the driving force.

Rather than adjusting the load density alone [Minshull & Charvis, 2001], the load overestimation can be mitigated by lowering the peripheral density relative to the seamount density (Figure 2.1b). For instance, Wessel [2001] used a realistic peripheral density ($\rho_s = 2300$ kg m^{-3}) with a constant seamount density ($\rho_t = 2800$ kg m^{-3}). I compare this two-boundary model with the dense core and uniform density models for a range of parabolic loads and elastic plate thicknesses. For this comparison, the crustal density is used for the load density. Figure 2.4 shows the maximum deflections obtained beneath the center of a given load as a function of parabolic seamount height (i.e., h_d). The edifice radius is determined by an empirical relationship between the

height and radius of typical seamounts, i.e., $r_d = 4.5h_d$ [Wessel, 2001]. The height and radius of the core are set to be half of those of the edifice, which is my conservative choice based on the previous studies [e.g., Robertson, 1967; Kellogg et al., 1987; Gallart et al., 1999; Weigel & Grevemeyer, 1999]. As Wessel [2001] pointed out, the two-boundary model (thick solid lines in Figure 2.4) produces less deflection than the uniform model (dashed lines in 2.4). However, the two-boundary model predicts more deflections than the dense core model (dotted lines in Figure 2.4) simply because the seamount of the two-boundary model is heavier than the dense core seamount (Figures 2.1b and 2.1c). The discrepancy between the two-boundary and dense core models increases when the parabolic seamount grows large. For smaller seamounts (Figure 2.4a) and thicker plates (Figure 2.4b), the differences between the above three models become negligible because the elastic plate is strong enough to support most of the applied loads.

In addition, I examine a uniform load with a load density, 2600 kg m^{-3}, which is the average of the densities used in the dense core model (thin solid lines in Figure 2.4). Because the average density is estimated by taking into account the volumes of the edifice and the core of the examined parabolic seamounts, the surface mass of the "average" density load is the same as that of the dense core load. However, this uniform case approximates closely the dense core model only for smaller parabolic seamounts ($h_d < 3$ km) on the thinnest plate ($T_e = 1$ km). As the parabolic seamount grows on the thinnest plate, the average density load produces significantly less flexure than the dense core load. Although the total mass and volume of the surface load are the same for both the average density and dense core loads, the dense core load is less equally distributed than the average density load. In other words, the dense core load becomes heavier than the average density load at the axis of the parabolic seamount, where the core material is concentrated. The difference between the subsurface loads of these two models also contributes to the different flexure predictions, because the

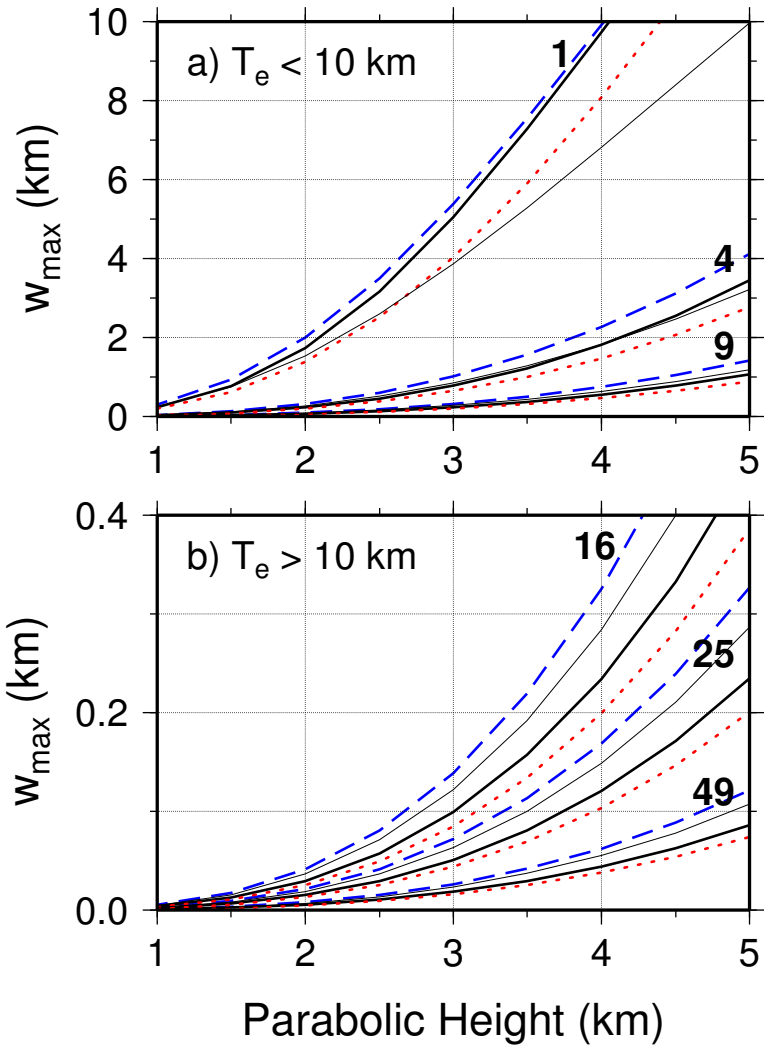

Figure 2.4: Maximum deflections for various parabolic seamounts. (a) Elastic plates thinner than 10 km. (b) Elastic plates thicker than 10 km. The dashed lines are for the uniform density model, the thick solid lines for the two-boundary model [Wessel, 2001], the thin solid lines for the uniform density model with a load density that is the average of the densities used in the dense core model, and the dotted lines for the dense core model. Each group of dashed, thick solid, thin solid, and dotted curves represents a distinct elastic thickness (T_e), shown in bold.

dense core model infills the flexure with heavier materials than the uniform density model with the average density. For other cases ($T_e > 4$ km), it falls between the predictions of the uniform model with the crustal density and the two-boundary model.

It is self-evident that the uniform density load with the crustal density is heavier than the dense core load because different densities are used for each loading part. If surface mass and peripheral density are the same for both flexure models, would the predicted flexure differ? In Figure 2.5, the surface mass of the dense core disc load is equated with the stacked uniform discs of the edifice density. For a simple comparison, the peripheral density is equal to the edifice density. The disc placed on top of the edifice disc has the same mass as the core above the reference level (Figure 2.5b). Figure 2.5c shows relatively insignificant differences between the deflections caused by the stacked uniform density discs and the dense core disc. The dense core model results in slightly larger deflections because the core material is assumed to extend down to the flexed crust and hence acts as an extra driving force. The difference between these models, however, increases when a realistic peripheral density is considered [Wessel, 2001], as examined above. This particular test illustrates that the surface mass is the largest contributor to flexural deformation of the plate [Menke, 1981]. However, constraining surface mass is complicated and requires gravity modeling, as discussed in the following section.

2.3.2 Flexure modeling with gravity data

I have shown above that the uniform density model tends to overestimate flexural deformation (Figure 2.4). Such bias, however, needs to be examined in light of the gravity prediction because free-air gravity and geoid anomalies are the most widely available data that are sensitive to both surface load and lithospheric flexure [Watts, 2001]. Using the Fourier transform approach of Parker [1972], I derive the gravity

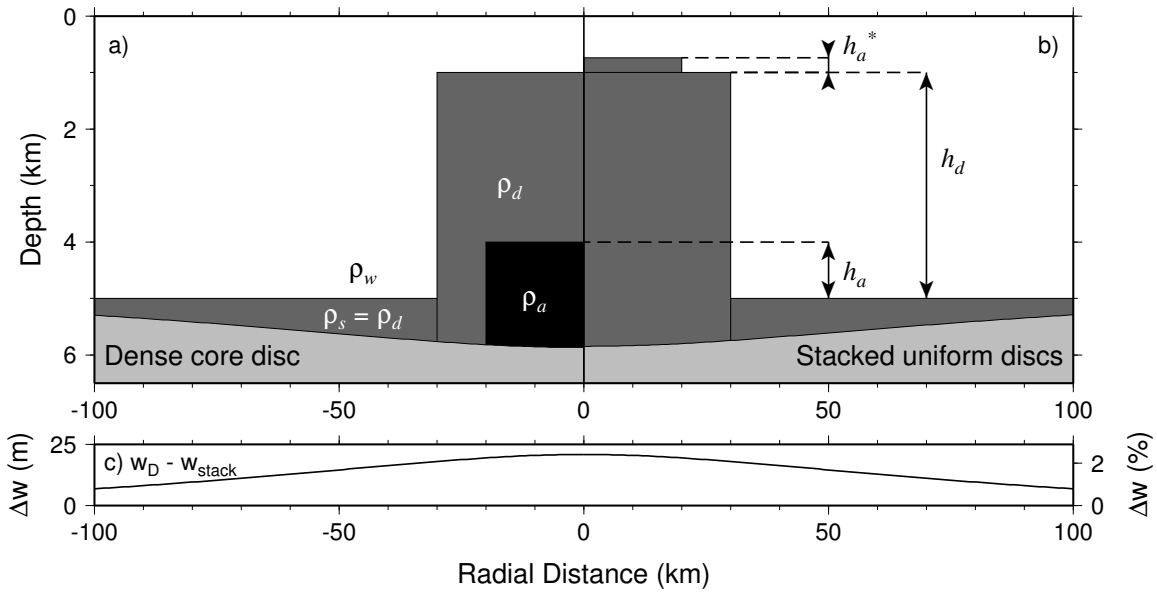

Figure 2.5: Comparison of (a) the dense core disc load and (b) stacked two uniform density discs, with $T_e = 20$ km. The mass of the top disc in (b) is equivalent to the mass of the core above the sea floor by adjusting its height (h_a^*). (c) Difference between the predicted deflections obtained by subtracting the stacked disc model from the dense core model.

anomaly for a dense core load as a sum of the following attractions due to the edifice (first term), the core (second term), the subsurface materials between the reference level and the flexed crust (third term), and the Moho topography determined by the flexure (fourth term):

$$F[\Delta g] = 2\pi G \exp(-|\mathbf{k}|d) \sum_{n=1}^{\infty} \frac{|\mathbf{k}|^{n-1}}{n!} \left\{ \begin{array}{l} (\rho_d - \rho_w) F[h_d^n(\mathbf{r})] \\ +(\rho_a - \rho_d) F[h_a^n(\mathbf{r})] + F[\Delta\rho_i(\mathbf{r}) w^n(\mathbf{r})] \\ + \exp(-|\mathbf{k}|t)(\rho_m - \rho_c) F[w^n(\mathbf{r})] \end{array} \right\}, \tag{2.15}$$

where $\mathbf{k}$ is the wavenumber vector, $\mathbf{r} = (x, y)$ is the position vector in space, d is the regional depth to the seafloor, t is the thickness of the oceanic crust, G is the gravitational constant, and F is the two-dimensional Fourier transform of the given layers of the edifice $h_d(\mathbf{r})$, the core $h_a(\mathbf{r})$, and the flexure $w(\mathbf{r})$. Here, n accounts for the linear ($n = 1$) and non-linear higher-order terms in eq. (2.15) and $\Delta\rho_i(\mathbf{r})$ in the

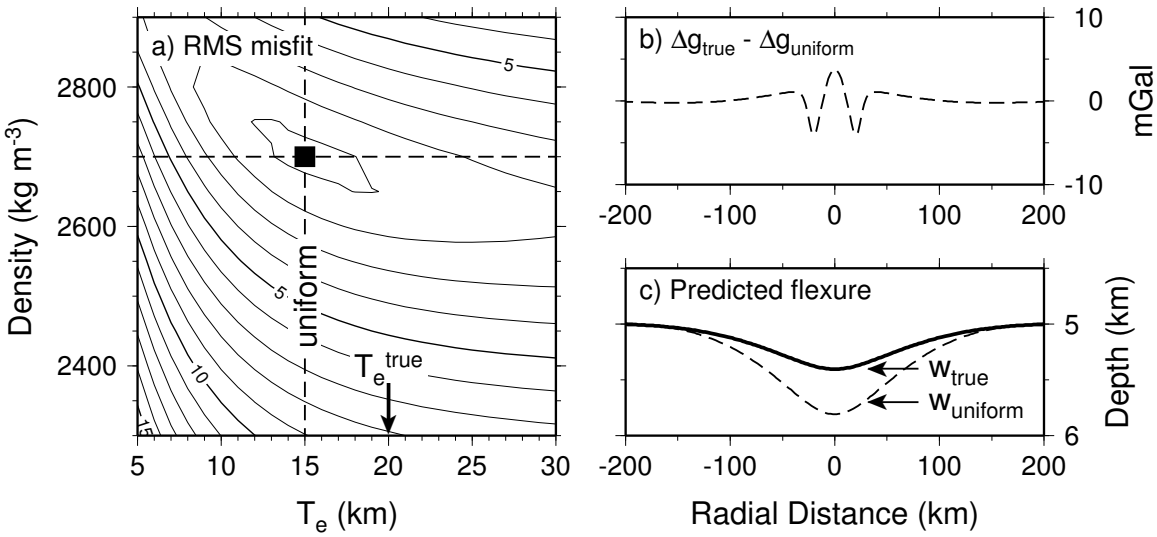

Figure 2.6: Flexure modeling using the gravity anomaly calculated from the dense core parabolic load of Figure 2.2b as the true data. (a) The root-mean-square (RMS) difference between the true and predicted gravity using the uniform density model. The free-air gravity anomalies over the parabolic seamount placed on the plate of $T_e = 20$ km are assumed to be the true data. (b) Residual gravity anomaly by subtracting the predicted gravity by the uniform density model from the true data. (c) Comparison between the true and predicted flexures by the uniform density model.

third term denotes the lateral variation in density contrast between the subsurface (i.e., infill) materials and the flexed crust (e.g., it becomes $(\rho_c - \rho_a)$ beneath the core). If the uniform density model uses the crustal density, then eq. (2.15) is simplified because the second and third terms cancel. If the load density is different from the crustal density, the third term of eq. (2.15), with the spatially invariant density contrast, $\Delta\rho_i(\mathbf{r}) = \rho_c - \rho_l$, is necessary for the gravity calculation. Because this uniform model has been used most commonly in previous flexure studies [e.g., Watts et al., 1975; Calmant, 1987; Smith et al., 1989; Ito et al., 1995; Lyons et al., 2000; Adam & Bonneville, 2008], my comparisons focus on differences in the best T_e estimated by the dense core and uniform density models constrained by gravity data.

For a simple comparison using synthetic data, I assumed that the dense core parabolic load of Figure 2.2b is the observed seamount structure. Other key parameters for gravity calculation were a regional water depth of 5 km and a crustal thickness

of 7 km. With the density parameters as listed in Table 1, the flexural depression for $T_e = 20$ km was calculated analytically using eq. (2.12); this is what I define as the "true" flexure model. To optimize the speed and accuracy of the Fast Fourier Transform (FFT), a square grid of 512 by 512 nodes was used for all calculations in eq. (2.15); this resulted in the true gravity anomaly over the parabolic seamount. The deflections due to the uniform density loads were estimated analytically using the solution of Lambeck & Nakiboglu [1980]. Then, the root-mean-square (RMS) misfits between the predicted gravity anomaly using the uniform density model and the observed data were computed for a range of elastic thicknesses and load densities. I kept up to the fifth-order term of Parker's expansion for calculating both the observed and predicted gravity anomalies.

This exercise shows that the uniform density model underestimates T_e when modeling is constrained by gravity data. The best T_e value of the uniform density model (Figure 2.6a; square and dashed lines) is 25% less than the true model (Figure 2.6a; arrow). The overestimated surface mass of the uniform density model adds an excessive positive contribution to the gravity prediction, which is counteracted by a negative contribution from the more flexed crust. As such, flexure modeling with gravity data seeks the best trade-off between the positive gravitational contribution of the seamount and the negative effect of the flexed crust. This trade-off, which is presented in Figure 2.6c, shows that the uniform density model results in larger deflections than the true flexure. However, Figure 2.6b shows disturbingly insignificant differences between the true and predicted gravity anomalies with the best uniform density model, reflecting the non-unique nature of gravity modeling [Al-Chalabi, 1971; Blakely, 1996]. In other words, the same gravity signal can be produced by two different geological structures as the uniform density model predicts a gravity signal relatively similar to the true data despite a heavier load density, underestimated T_e (Figure 2.6a), and overestimated flexural deformation (Figure 2.6c).

In addition, Figure 2.6b shows that the dense core model predicts positive gravity contributions from both the surface and subsurface core materials, while the uniform density model is affected by the negative contribution from the subsurface load material. This is manifested as a positive difference over the summit; however, differences due to peripheral densities are less distinct in this comparison. Such detailed differences are likely to be masked by noise in real gravity data over seamounts.

In order to make general comments about the biases observed in flexure modeling using gravity data, I repeated the above exercise for a range of elastic thicknesses. The dense core parabolic load in Figure 2.2b was again regarded as the observed seamount structure. By placing this parabolic seamount on various elastic plates, I calculated the true gravity anomaly for a given true T_e and then determined the best T_e and ρ_l for the uniform density model that minimized the RMS misfits (green lines in Figure 2.7). Because many previous T_e estimates were obtained with $\rho_l = \rho_c$, I also found the best T_e when the load density was set to the crustal density (orange line in Figure 2.7a). Upper and lower bounds of these T_e estimates (shaded areas in Figure 2.7a) were obtained at a 5% tolerance level from the minimum RMS [Watts et al., 2006], but sampled along ρ_c and best ρ_l. Therefore, this uncertainty bound is narrower than that of a 5% uncertainty ellipse.

If there were no shortcomings in the flexure modeling with the uniform density model, the predicted T_e values should follow the dashed 1:1 line in Figure 2.7a. Instead, I observe a significant underestimation of T_e, as was also found by Minshull & Charvis [2001]. For thin elastic plates ($T_e < 10$ km), the uniform density model with the crustal density predicts T_e close to the true model. This is also reflected in Figure 2.7b because the uniform density model with variable load density minimizes the misfits with a higher load density for thinner plates. However, the best load density determined by RMS minimization is too large so that the amount of the flexure is significantly overestimated (e.g., Figure 2.6c). In gravity computation, the

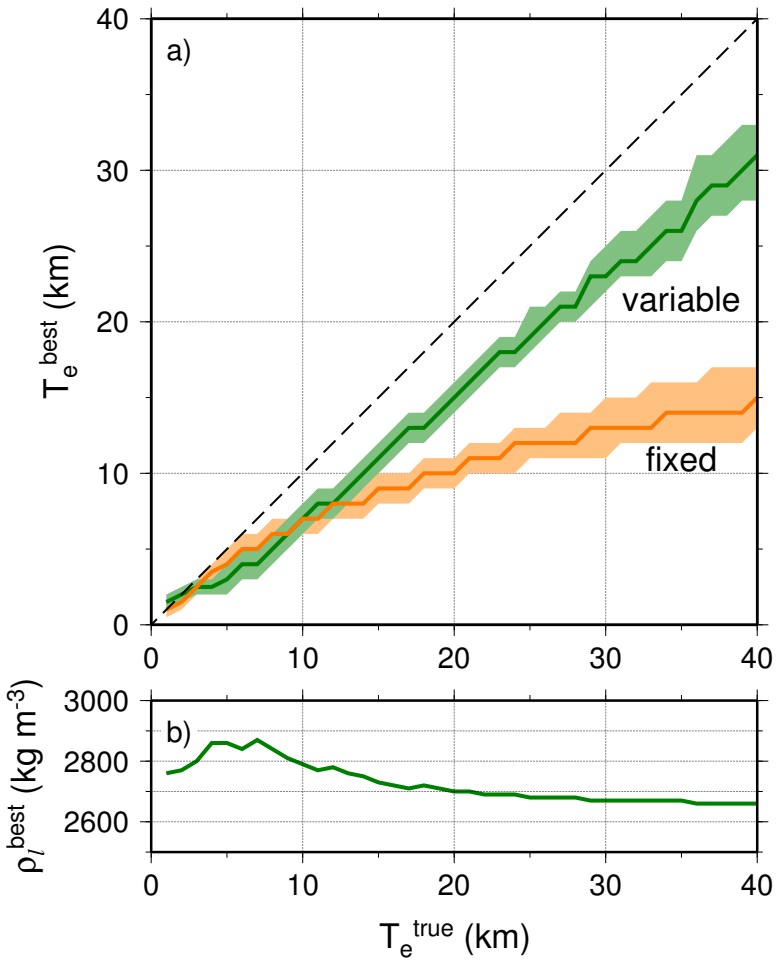

Figure 2.7: Comparison of the best models obtained by the uniform density model with the true models. I repeat the flexure modeling of Figure 2.6 with a range of plate thicknesses and show how the model parameters of T_e and ρ_l are determined by the uniform density model. (a) Best T_e estimates by the uniform density model with fixed ($\rho_l = \rho_c$, orange) and variable (green) load density. Shaded ares indicate a 5% uncertainty bound of each T_e estimate. (b) Best load density estimates from the uniform density model with variable load density.

uniform density model with variable ρ_l still achieves a balance between the gravity contributions from the load and the flexed crust, but results in largely underestimated T_e relative to the uniform density model with $\rho_l = \rho_c$.

For strong elastic plates, the underestimation of T_e by the uniform density model with $\rho_l = \rho_c$ exacerbates further. Because the surface load is fixed and overestimated, the only way to offset the extra positive gravity signals and minimize the misfits is to decrease T_e (Figure 2.7a). The uniform density model with variable ρ_l, however, reduces the load density gradually to produce better gravity fits (Figure 2.7b) and results in better T_e estimates. Figure 2.7b shows that a $\sim$100 kg m^{-3} reduction from the typical crustal density (2800 kg m^{-3}) reduces the underestimation of T_e significantly. In addition, this indicates that the role of load density in flexure modeling is more important for seamounts on strong elastic plates.

2.3.3 Flexure modeling with arbitrary dense core loads

In the preceding discussions, I have dealt with synthetic examples using axisymmetric disc and parabolic seamounts, which may in some cases approximate the actual seamount bathymetry [e.g., Lambeck, 1981a]. However, such idealized loads are not always adequate for contemporary geophysical studies that utilize high-resolution gridded bathymetry at seamounts. In this respect, the greatest advantage the uniform density model affords in the flexure and gravity calculations lies in the simplicity of the flexural response function [Watts, 2001]:

$$\Phi(\mathbf{k}) = \left(1 + \mathbf{k}^4/k_l\right)^{-1}. \tag{2.16}$$

with k_l defined by eq. (2.11) with $x = l$. The lithospheric flexure due to any given shape of topography, h_l, is calculated in the wavenumber domain by

$$F[w(\mathbf{r})] = \frac{\rho_l - \rho_w}{\rho_m - \rho_l} F[h_l(\mathbf{r})]\Phi(\mathbf{k}). \tag{2.17}$$

Calculation of flexure using eq. (2.17) is fast and reliable. However, I cannot adapt eq. (2.17) directly for the dense core model to make use of an actual bathymetry grid, because eq. (2.16) requires a constant k_l. From the preceding comparisons, I find that the surface mass plays a more important role in flexure modeling than changes to the density of subsurface materials. Also, Menke [1981] proved analytically that a point load equivalent to a distributed load does not alter the amplitude and wavelength of flexure. Therefore, I circumvent the inherent limitation of the dense core model by constructing a uniform load of peripheral density that is equivalent to the sum of the surface core and edifice loads:

$$h_e(\mathbf{r}) = \frac{\rho_d - \rho_w}{\rho_s - \rho_w} h_d(\mathbf{r}) + \frac{\rho_a - \rho_d}{\rho_s - \rho_w} h_a(\mathbf{r}). \tag{2.18}$$

While this modification allows me to use eq. (2.16), it underestimates the amplitude relative to the analytic solutions because the subsurface materials beneath the edifice and the core are now replaced with less dense peripheral material. Comparison of maximum amplitudes calculated using this equivalent load, $h_e(\mathbf{r})$, with the exact dense core model indicates that such biases are generally less than 10% and increase only when the atypical situations of large seamounts on thin elastic plates are considered. I thus utilize eq. (2.18) to approximate the dense core surface load and calculate lithospheric flexure from the equivalent load, while the gravity calculation is obtained by eq. (2.15). In the following, I demonstrate a practical use of the dense core model for Howland Island in the Pacific and examine if the bias inherent in the uniform density model discussed above is noticeable when analyzing real data.

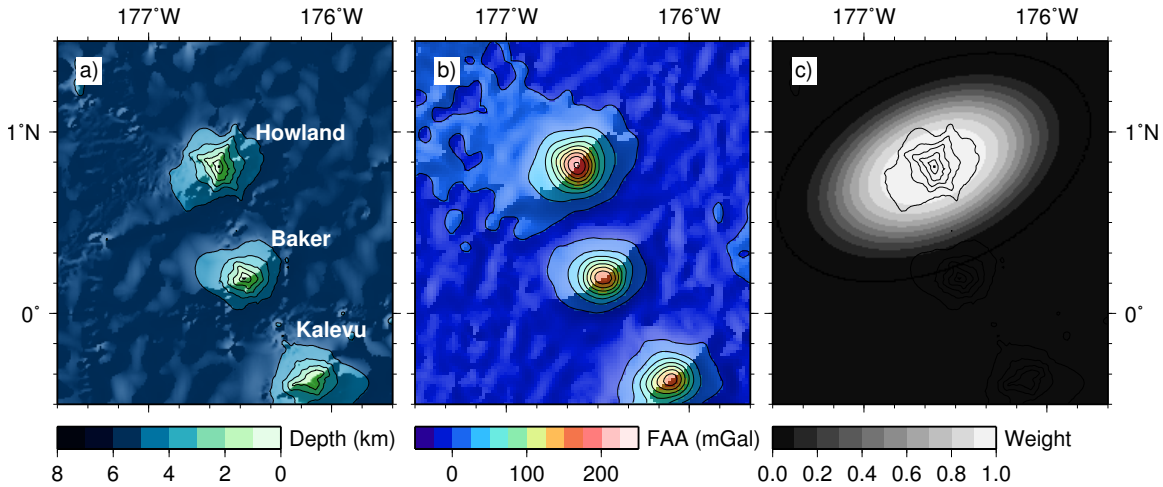

Figure 2.8: Observed geophysical data near Howland Island. (a) SRTM30+ bathymetry [Becker et al., 2009]. (b) Satellite-derived free-air gravity version 18.1 [Sandwell & Smith, 2009]. (c) Weighting function used for the regional-residual separation and RMS estimates for the flexure modeling in order to emphasize Howland. The depth contours of 1 km interval are overlaid.

2.4 Case Study: Howland Island

Detailed geophysical and geochemical mapping of the Tokelau seamount chain was carried out by R/V *Melville* in 1999 [Koppers & Staudigel, 2005]. Howland Island is situated on a 127 ± 1 Ma oceanic plate at the northern end of this trail [Müller et al., 2008], and its formation age is 72.3 ± 2.7 Ma [Koppers et al., 2007]. The shipboard depth measurements along the Tokelau chain can be downloaded from the Seamount Catalog at the EarthRef.org. However, I utilize SRTM30_PLUS V5.0 [Becker et al., 2009] for flexure modeling because it provides complete data coverage in the vicinity of Howland by blending the same ship data and the predicted bathymetry [Smith & Sandwell, 1997]. From the previous $^{40}Ar/^{39}Ar$ study [Koppers et al., 2007], the predicted elastic plate thickness beneath Howland is 20 ± 2 km using the empirical relationship of Calmant et al. [1990] that closely follows the 400 °C isotherm. By applying both the dense core and uniform density models to Howland, I will differentiate between these two models.

For the synthetic loads (Figure 2.2), a constant depth was sufficient to define the

reference level. Such a choice for actual bathymetry data, however, can misrepresent the reference level and in turn bias the surface load, because a single (e.g., average) depth overlooks bathymetry variations of other geological phenomena, such as swells and the thermal subsidence of the plate. I thus performed a regional-residual separation of the bathymetry around Howland using directional median (DiM) filtering, in order to estimate the reference plane that defines the surface load [Wessel, 1998; Kim & Wessel, 2008]. To determine the best filter width for an effective separation, I followed the optimal robust separation (ORS) technique [Wessel, 1998]. I explored a range of filter widths to determine a width that maximized the ratio of the volume to the area of the residual bathymetry. In this study, however, the ratio was computed from a weighted residual bathymetry (Figure 2.8c) so that the separation could be optimized near Howland. The data domain for DiM-based filtering was extended by about 2° in all directions from Figure 2.8a in order to avoid possible edge effects of the filtering. Because the background seemed very gentle, I chose four sectors for the DiM filtering and smoothed the DiM-filtered results using a spatial median filter with 40 km filter width. The ratio was estimated for a range of filter widths and maximized for a 100 km filter width [see Kim & Wessel [2008] for details]. The Howland surface load (i.e., the residual), therefore, was obtained by subtracting the DiM-filtered bathymetry from the observed data (Figure 2.9a).

Although there is no available data (e.g., seismic refraction profiles) indicating the existence of a core inside Howland, I can infer from previous studies [e.g., Watts et al., 1997; Araña et al., 2000; Minshull & Charvis, 2001; Kopp et al., 2004; Camacho et al., 2009; Contreras-Reyes et al., 2010] that the core is similar in shape to the seamount edifice. O'Higgins [Kopp et al., 2004] and La Reunion [Gallart et al., 1999], for example both have edifices with low P wave velocity ($\sim$3-4 km s^{-1}) and core structures outlined by $\sim$5 km s^{-1}. However, Great Meteor [Weigel & Grevemeyer, 1999] and Louisville Guyot [Contreras-Reyes et al., 2010] show higher P velocities for

the edifice (∼5 km s^{-1}) and the core (∼6.5 km s^{-1}). Thus, I consider the dense core to be correlated with a range of P velocities (i.e., 5-6.5 km s^{-1}), which separates the core from the volcanic edifice. In addition, the observed cores are generally about 1 to 2 km below the outer edifice. With extrapolation from these observed cases, I constructed a possible core for Howland by subtracting 2 km from the residual and only keeping positive values (Figure 2.9c; dashed line). Then, the equivalent load (Figure 2.9b) of the peripheral density was obtained by eq. (2.18) and used to compute flexure for various elastic thicknesses.

For the gravity calculation, the regional depth, $d = 5.4$ km, was taken from the mean depth of the regional bathymetry. The thickness of the oceanic crust, t, was 6.5 km and the densities of the water, the crust, and the mantle were 1030, 2900, and 3330 kg m^{-3}, respectively [Lambeck, 1981b; Adam & Bonneville, 2008]. For the dense core model, the densities for the core, the edifice, and the moat were the same as those I used in the previous flexure calculation (listed in Table 1), assuming that the core and the edifice of Howland are similar to those of Great Meteor [Weigel & Grevemeyer, 1999]. The layers of the core, the edifice, and the flexure predicted with the equivalent load were used to calculate the spatial variation of the subsurface materials needed for the third term in eq. (2.15). Then, the gravity anomalies due to the core, the edifice, and the subsurface were summed. For the uniform density model, I computed flexure for a range of load densities and elastic plate thicknesses using the residual bathymetry. For both models, however, the regional bathymetry (i.e., the DiM-filtered data) was added back to both the residual and predicted flexure before the gravity calculation so that the predicted gravity can exhibit regional gravity components similar to the observed.

The flexure and gravity computations were carried out with all features inside the domain; however, the RMS misfits were computed from the weighted difference [Watts et al., 2006] between the predicted and the satellite-derived gravity data of

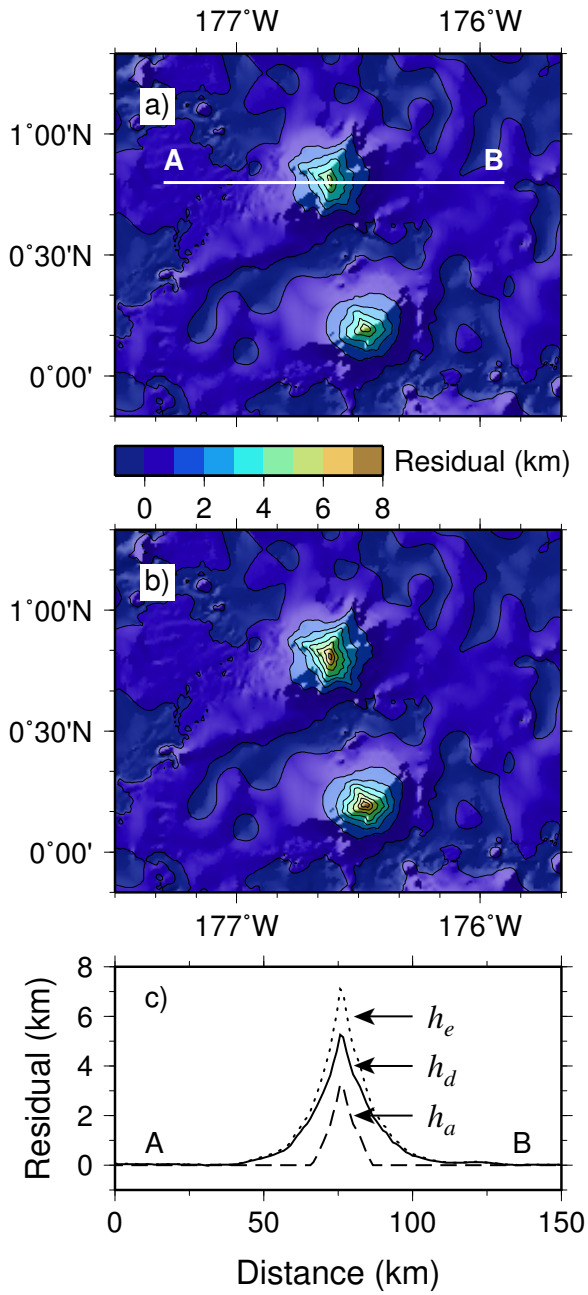

Figure 2.9: Dense core load for Howland Island. (a) The surface load is defined by the residual bathymetry. (b) The equivalent load has the same mass as the presumed surface loads of the seamount. (c) The presumed core (dashed line, h_a), the edifice (solid line, h_d) and the equivalent load (dotted line, h_e) along profile AB in (a).

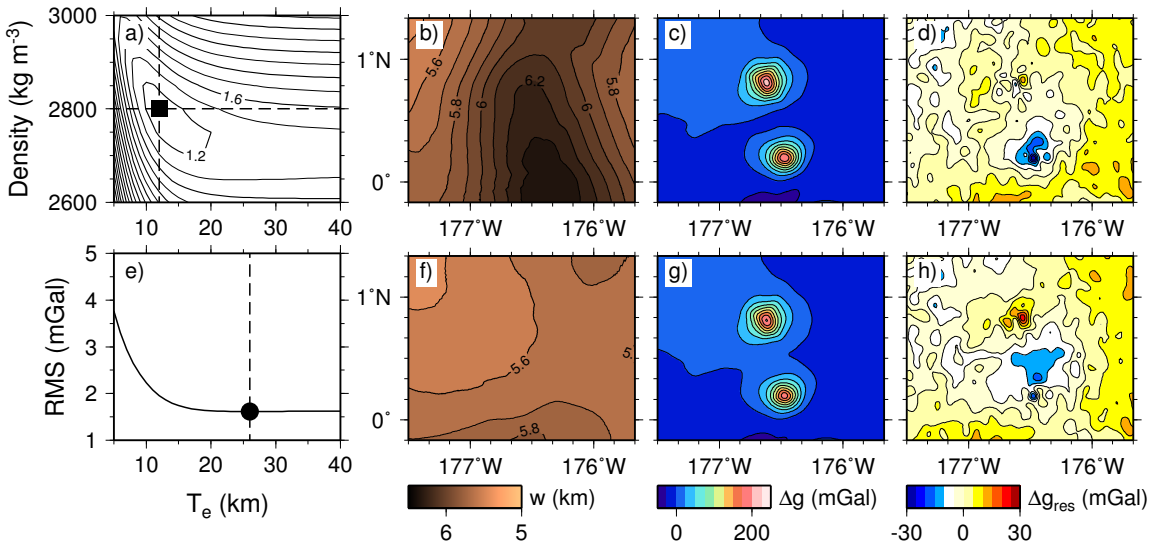

Figure 2.10: Comparison of the uniform density and dense core models for Howland Island. The RMS misfits between the observed and the predicted gravity using (a) the uniform density model and (e) the dense core model are used to determine the best T_e. (b) Predicted deflection for the best uniform density model. (c) Predicted gravity anomaly for the best uniform density model. (d) Residual gravity for the best uniform density model. (f) Predicted deflection for the dense core model. (g) Predicted gravity for the dense core model. (h) Residual gravity for the dense core model.

version 18.1 [Sandwell & Smith, 2009]. The lower resolution of the satellite-derived gravity (compared to shipboard measurements) typically manifests itself as lower amplitudes over short-wavelength features like seamounts. For example, Watts et al. [2006] showed that the satellite-derived data of version 14.2 only recovered $n = 1$ over Wahoo Guyot. Because of the improved resolution for short-wavelength features in the gravity data of version 18.1, however, setting $n = 2$ in eq. (2.15) was necessary to recover a comparable amplitude of the predicted signals to that of the observed data [Marks & Smith, 2007]. In particular, the peak amplitude at Wahoo Guyot is amplified from ∼55 mGal (version 14.2) to ∼82 mGal (version 18.1).

The uniform density model minimizes the RMS misfits at $T_e = 12$ km (Figure 2.10a), which is substantially less than the predicted thickness based on the age data. The upper and lower bounds of the uniform density model prediction were estimated at a 5% tolerance level from the RMS minimum and determined along the best load

density (see Figure 2.12). In contrast, the dense core model is minimized at T_e = 26 km (Figure 2.10e). However, the changes in the RMS misfits from this global minimum are subtle (< 0.01 mGal) so that the upper bound of the best dense core model is unresolved (Figure 2.12; question mark).

The difference in T_e estimates between the uniform density and dense core models is most apparent in the predicted deflections of Figures 2.10b and 2.10f. As the uniform density model favors a thin plate and a typical crustal density (Figure 2.10a), it predicts more flexural deflections than the dense core model. This overestimated flexure increases southward toward Baker Island. However, the gravity anomaly predicted by the uniform density model (Figure 2.10c) is generally more comparable with the observed data (Figure 2.8b) than that of the dense core model, especially if we consider the location of the zero contour between the Howard and Baker Islands. This zero contour is not apparent in the predicted gravity by the dense core model (Figure 2.10g). In Figure 2.10d, however, the uniform density model shows large negative residual anomalies over Baker. This indicates that the best uniform density model for Howland is not adequate for Baker. Although my computation excluded Baker by using an weight function centered on Howland (Figure 2.8c), such negative residuals are large enough to suspect that the uniform density model might decrease T_e even more if both islands were included in flexure modeling. The dense core model instead exhibits a broad negative anomaly between two islands, where the zero contour is observed (Figure 2.10f).

In Figure 2.11a, the comparison of the predicted gravity anomalies for the dense core (dotted line) and uniform density (dashed line) models along profile AB of Figure 2.9a shows that both predictions generally agree with the observed data. While the best load density of the uniform density model is dense enough to overshoot the peak of the observed anomaly, the dense core model predicts less than the peak because the densities of the core and the edifice are fixed during calculation. As demonstrated

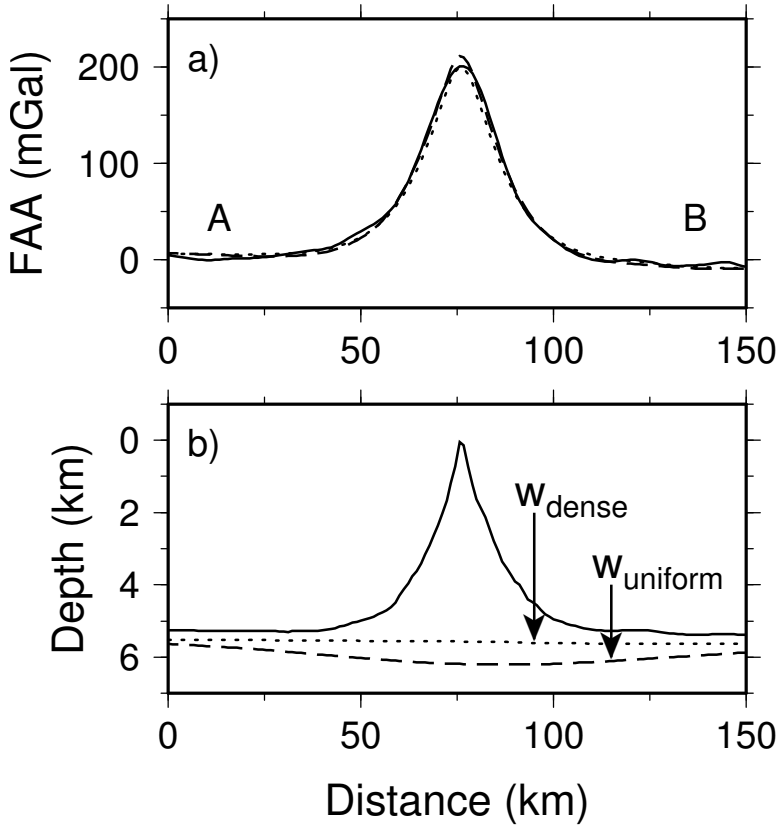

Figure 2.11: Comparison of predicted gravity and flexure along profile AB in Figure 2.9a. (a) Predicted gravity anomalies. (b) Predicted flexure. The dotted line is for the dense core model and the dashed line for the uniform density model.

analytically in the preceding examples, the uniform density model predicts larger deflections beneath Howland than the dense core model does (Figure 2.11b).

Watts [1978] first showed the correlation between the modeled elastic thicknesses beneath seamounts and the depth to the 450 °C ± 150 °C isotherm of the plate cooling model [Parsons & Sclater, 1977]. Such relationships have been consistently supported by many subsequent studies [e.g., Calmant, 1987; Kruse et al., 1997; Watts et al., 2006] and used as a proxy for age prediction of either plate or seamount [Calmant et al., 1990]. In addition, any outliers from this trend (i.e., elastic plates anomalously thinner than expected) have been the focus of many controversies and have invoked proposals of other additional geodynamic processes, including lithospheric thinning [Crough, 1983], lithospheric reheating [McNutt, 1984], and small-scale convection [Dalloubeix & Fleitout, 1989] to explain such anomalously thin plates.

I compare the elastic thickness estimates for Howland with the plate cooling model of Parsons & Sclater [1977] in Figure 2.12, which includes also the age prediction curve (dotted line) of Calmant et al. [1990]. The estimate of the uniform density model is above the 300 °C isotherm, while that of the dense core model is close to the 500 °C isotherm. The underestimation of the uniform density model, thus, is manifested by a thinner T_e prediction that is consistently observed from the preceding synthetic examples. Because the previously proposed correlation between T_e and age at seamounts are based on the uniform density model estimates, the dense core model prediction does not follow the age prediction curve described by the 400 °C isotherm [Calmant, 1987]. In addition, the significant disparity between the T_e estimates beneath seamounts and those obtained at trenches and fracture zones have suggested that the former predictions are systematically underestimated [e.g., McNutt, 1984; Wessel, 1992]. Therefore, it is noteworthy that the dense core model with a thicker plate can account for the gravity anomaly at Howland (Figures 2.10 and 2.11) and follows a hotter isotherm (Figure 2.12). This result is in agreement with findings from

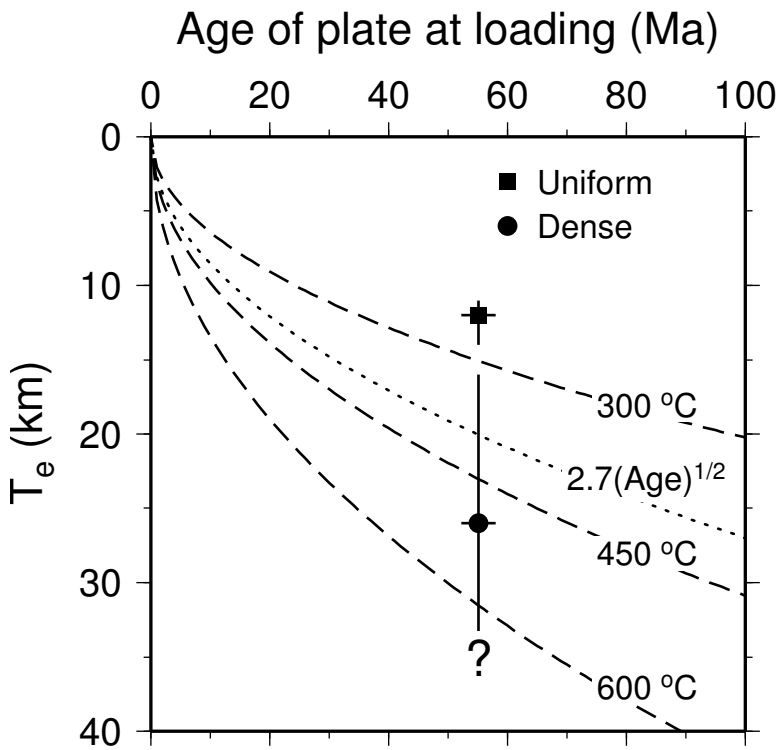

Figure 2.12: Elastic thickness estimates for Howland Island as a function of age of the lithosphere at the time of loading. The 5% uncertainty bounds for the T_e values (vertical bars) are sampled along the best load density for the uniform density model and from the RMS misfits for the dense core model. However, the upper bound of the dense core model is not resolved (question mark) because the RMS misfits show subtle changes for thicker plates (Figure 2.10e). The age uncertainty bounds (horizontal bars) are the sum of the uncertainties in the ^{40}Ar/^{39}Ar age data [Koppers et al., 2007] and the digital age grid of the seafloor [Müller et al., 2008]. Theoretical isotherms [Parsons & Sclater, 1977] and empirical relationship [Calmant et al., 1990] are shown as dashed and dotted lines, respectively.

flexural studies at fracture zones and trenches, without needing additional reheating mechanisms to reset the thermal age of the lithosphere.

2.5 Concluding Remarks

I have demonstrated how the uniform density model underestimates T_e and overestimates deflections using various synthetic and real examples. When flexure modeling is constrained by gravity data alone, such biases are often concealed because the pre-

dicted gravity with distorted T_e and deflections can nevertheless be the best fit for the observed data. This non-uniqueness of solutions to the gravity field can be circumvented by using additional observations (e.g., seismic profiles) or mitigated by a more rigorous analysis. In this study, I have shown that the inclusion of a dense core is important when approximating the first-order inhomogeneous internal seamount structure. Thus, the dense core model appears to be more suitable for investigating the thermal and mechanical properties of the oceanic lithosphere.

My study does not imply that all published T_e estimates are underestimated. However, some of them could be biased to some degree simply because of the load density used in the flexure modeling. The flexural studies on Tenerife in the Canary Islands are such a case. Watts et al. [1997] predicted the elastic thickness beneath Tenerife to be 20 km, which was 10 km less than the expected thickness based on the dated rock samples. Later, Collier & Watts [2001] revised the flexure model by reducing the load density and obtained the expected elastic thickness. Another important factor is the quality of the bathymetry and gravity data around seamounts of interest. For example, Lambeck [1981b] computed analytically the flexural deformation of the lithosphere beneath the Cook Islands by approximating the topographic features as the stacks of uniform density discs. Although he used a load density less than the crustal density and included a core in his calculation, his T_e estimates were the same as the study of Calmant & Cazenave [1986] who used the crustal density as the load density. Because both studies relied on a few SEASAT altimetry tracks and had poor bathymetric constraints (e.g., SYNBAPS [Van Wyckhouse, 1973]), the careful details of the modeling space incorporated by Lambeck [1981b] were not effectively propagated into the solution space.

Finally, I consider underplating beneath large seamounts or ocean islands that is quite commonly observed seismically [e.g., Weigel & Grevemeyer, 1999; Ali et al., 2003]. In flexure modeling, the role of underplating is to reduce the total flexural

depressions because lighter underplated material adds to the buoyancy and hence works against the surface load. This process, in particular, is necessary for the uniform density model in order to compensate for the overestimated deflections so that a modeler can achieve a better fit between the predicted and observed flexure. However, for such sizable volcanoes, I can presume the existence of a dense core as a constructional feature. If the dense core model alone can predict the flexed crust, then the sub-surface load due to underplating becomes less important in calculating deflections; however, its contribution to the gravity anomaly will remain. Therefore, I suggest the role of underplating in flexure modeling may need to be reassessed with a dense core model.

Chapter 3

New Global Seamount Census from Altimetry-Derived Gravity Data

I have developed a non-linear inversion method to detect seamounts in the satellite-derived vertical gravity gradient (VGG) data; a recent revision to the VGG data reveals more detail of the ocean bottom than previous datasets. I approximate VGG anomalies over seamounts as sums of individual, partially over-lapping, elliptical polynomial functions, which allows me to form a nonlinear inverse problem by fitting the polynomial model to the observed VGG data. The model parameters for a potential seamount include the geographical location, peak VGG amplitude, major and minor axes of the elliptical base, and the azimuth of the major axis. The nonlinear inversion is very sensitive to the initial values for the location and amplitude; hence, they are constrained by the center and amplitude of the uppermost contours obtained with a 1-Eötvös contour interval. With these initial conditions from contouring, I execute my step-wise and fully automated inversion and obtain optimal model estimates for the potential seamounts; these are statistically evaluated for significance using the Akaike Information Criterion and F-tests. A logarithmic barrier technique is applied to ensure positivity of all seamount amplitudes. After automatic and manual inspections of the model parameters determined by the inversion, I estimate actual heights and basal ellipses of the inspected potential seamounts directly from the predicted bathymetry grid. A total of 24,643 potential seamounts ($h \geq 0.1$ km) globally are characterized in this study. Although this number is significantly lower than predictions from previous studies, a first-order reconciliation of the size-frequency statistics

obtained from those studies reveals that the previous counts are systematically overestimated. Because of the ambiguity of gravity signals due to small seamounts of $h <$ 1 km and the overlap with abyssal hills, I tentatively estimate the global seamount census to lie in the 40,000–55,000 range.

3.1 Introduction

Despite considerable post-World-War-II investments in ocean exploration [e.g., Chandler & Wessel, 2008], vast areas of the ocean floor (e.g., 90% at 1 minute resolution [Becker et al., 2009] or 70% at 5 minute resolution [Wessel & Chandler, 2010]) remain uncharted by surface ships. Given cost estimates of $\sim 10^{10}$ USD for a complete mapping with high-resolution multi-beam shipboard measurements [Vogt & Jung, 2000], a global coverage of the Earth's underwater landscape at $\sim$100 m resolution seems highly unlikely for the foreseeable future. Yet, at the more modest resolution of $\sim$5-10 km, an alternative approach to studying the ocean bottom is available: sea-surface height measurements from orbiting satellites record spatial changes in the gravitational field caused by the density contrast between water and bathymetric features. A global gravimetric view of the sea floor, thus, becomes accessible through satellite-derived gravity data [Haxby et al., 1983; Sandwell & Smith, 1997]. This marine gravity anomaly dataset has provided uniform and dense data coverage over all oceans and has enabled researchers to investigate both remote bathymetric features unexplored by oceangoing expeditions [e.g., Mammerickx, 1992; Small & Sandwell, 1994] as well as large-scale deep-seated geophysical phenomena [e.g., Haxby & Weissel, 1986].

Traditionally, seamounts have been defined as isolated, extinct or active underwater volcanoes rising more than 1 km above the surrounding seafloor [Menard, 1964]. Given rapid advances in marine technologies, this height limit has been adjusted to include volcanic constructs with heights as low as 50–100 m [e.g., Smith & Cann, 1990;

Behn et al., 2004]. Whether small or large, seamounts play important roles in a diverse range of social and natural phenomena. For instance, they can pose as obstacles to submarine navigation [e.g., BBC, 2005] and affect the propagation of tsunami waves [e.g., Mofjeld et al., 2004]. Seamounts also sustain diversified marine habitats [e.g., Stocks, 2005] and even influence the global ocean circulation [e.g., Gille et al., 2004]. Many older seamounts are covered by manganese crust, a potential mineral resource that one day may be economical to harvest [e.g., Friedrich & Schmitz-Wiechowski, 1980; Grigg et al., 1987]. Finally, the geographical and size-frequency distributions of seamounts are required to study the evolution of underwater volcanism through time and space [e.g., Wessel, 2001]. Consequently, it is of great importance to locate and characterize seamounts globally.

Because of differences in data sets and methodologies, many researchers have arrived at different global assessments of seamounts [Craig & Sandwell, 1988; Wessel, 2001; Kitchingman & Lai, 2004; Hillier & Watts, 2007]. A review of these methods and the uncertainties of the different approaches and estimates have been presented by Wessel et al. [2010]. Given the uniform coverage of satellite altimetry, such data traditionally have been used to assess the global seamount census estimates. However, the most-cited studies relied on early versions of the Geosat/ERS grids (v. 7.2) that are now almost 15 years old [Wessel & Lyons, 1997; Wessel, 2001]. Furthermore, the simple methodology employed in the previous studies placed several restrictions on the attributes that could be extracted from the data. In this paper, I will use the latest altimetry data and introduce a new nonlinear inversion method for seamount detection, discuss the development and limitations of my method, present a revised global seamount census, and finally compare my new estimates with those of previous studies.

3.2 The Vertical Gravity Gradient (VGG) Grid

To recover marine gravity anomalies from satellite altimetry data it is assumed that the sea-surface heights above the reference ellipsoid equal the geoid heights. By using a first-order linear relationship between geoid height and gravitational potential (i.e., Brun's equation), the east and north components of the vertical deflection (i.e., the slope of the geoid) are obtained directly from the first east- and north-derivatives of the sea-surface height [Heiskanen & Moritz, 1967; Sandwell & Smith, 1997]. Because the gravitational potential must satisfy Laplace's equation, the VGG equals the sum of the first derivatives of the east and north vertical deflections. Consequently, the VGG is the sum of the east and north second derivatives of the observed sea-surface heights, i.e. the curvature of the geoid. To construct the VGG grid, therefore, neither spherical harmonics nor Fourier transforms are required [Sandwell & Smith, 1997]. Such further processing, however, is necessary to derive free-air gravity anomalies (FAA) from the VGG grid. Due to the simplicity of the VGG computation, the VGG grid is the primary geopotential dataset retrieved from the altimetry measurements. The spatial second derivatives imply that VGG amplifies short-wavelength signals (such as observed over seamounts and fracture zones) and suppresses long-wavelength trends (e.g., those associated with flexure and hotspot swells). Hence, the VGG grid becomes more suitable than the FAA grid for finding small features such as seamounts [e.g., Wessel & Lyons, 1997]. In addition, recent reprocessing of Geosat and ERS-1 altimetry data with a rigorous waveform re-tracking method has improved significantly both accuracy and resolution of the data [Sandwell & Smith, 2005, 2009]. The resolution, in particular, has been enhanced by a factor of 1.3 relative to previous releases, which should significantly improve my chances of finding unmapped seamounts, especially those taller than 1 km. Therefore, I have utilized the 1-min Mercator VGG grid (v. 16.1) to reassess the global seamount distribution.

The coordinate system of the VGG grid is not conventional because gridding was

performed in an equidimensional spherical Mercator map projection domain [Sandwell & Smith, 1997]. For the VGG 16.1 grid, the grid cell dimensions are 1 arc minute (width) by 1 arc minute times the cosine of latitude (height). As a result, the number of grid cells per 1 arc degree increases with latitude, resulting in more data points toward the poles. If one simply projects this grid to the common geographical coordinate system, the original data points must be averaged for a cell with 1-min by 1-min dimension. This process dilutes the original resolution of the VGG grid, preferentially at higher latitudes. Thus, to preserve the full resolution of the VGG grid, I performed my data processing and nonlinear inversion directly in the Mercator domain and only projected my final estimates back to geographical coordinates.

3.3 Methodology

3.3.1 VGG potential seamounts

High-resolution shipboard bathymetric mapping of seamounts has revealed a multiplicity of morphological forms, ranging from simple circular, truncated cones to complicated stellate shapes [e.g., Batiza & Vanko, 1983; Rappaport et al., 1997; Mitchell, 2001]. While larger seamounts (taller than 3 km) are often reshaped by the development of rift zones and flank collapses that result in complex volcanic edifices (e.g., Ojin and Nintoku seamounts of the Emperor Seamount Chain [Smoot, 1982]), smaller seamounts tend to have single volcanic centers and display sub-circular structures (e.g., Lamont Seamount Chain south of the Clipperton Transform [Fornari et al., 1988]). Mitchell [2001] found that the transition from circular to stellate forms of seamount occurs gradually over a 2–4 km edifice height range, with the best transition estimate of 3 km height. Previous global seamount studies consistently show that the majority ($> 83\%$) of detected seamounts are smaller than 3 km height [Wessel, 2001; Hillier & Watts, 2007; Wessel et al., 2010]. Thus, I assume that an "ideal"

volcanic edifice is an elliptical truncated cone and anticipate that my estimates will be applicable for most of the seamounts detected by my study, except for larger seamounts with stellate form. Consequently, as most larger seamounts have been mapped bathymetrically I purposefully bias my modeling to be optimized for detecting and parameterizing the smaller and more numerous seamounts.

Gravity anomalies over seamounts observed at the sea surface are much smoother than shipboard bathymetry because the amplitudes of the gravity anomalies are attenuated exponentially with increasing depth to the seafloor, and this attenuation preferentially affects shorter wavelengths [Blakely, 1996]. Even if the volcanic edifice is a perfect cone, the gravity anomaly takes on a smoother (e.g., Gaussian-like) shape due to the attenuation. I take advantage of this "upward continuation" phenomenon when searching for seamounts in the gravity data because a Gaussian shape can be expressed analytically and is easy to manipulate in both the spatial and spectral domains. For example, Wessel & Lyons [1997] employed a circular Gaussian shape to approximate gravity anomalies caused by seamounts. In their approach, however, the distance to the first zero crossing (i.e., the radius of a seamount base) was assumed to be equal to the 3σ range that accounts for about 99.7% of the area under the Gaussian function (since the curve never reaches zero). This causes the seamount shape to be discontinuous at its base. In contrast, I will utilize an elliptical polynomial model, R, which is similar to the Gaussian model but explicitly goes to zero at the seamount base (Figure 3.1):

$$R(\mathbf{x}, \mathbf{x_o}, p, a, b, \theta) = \begin{cases} p\frac{(1+r)^3(1-r)^3}{1+r^2} & |r| \leq 1 \\ 0 & |r| > 1 \end{cases}, \tag{3.1}$$

where $\mathbf{x} = (x, y)$ is the position vector, $\mathbf{x_o} = (x_o, y_o)$ is the summit location, and p is the peak amplitude. Then, the normalized radial distance from the summit, r, is

defined as

$$r = \sqrt{A(x - x_o)^2 - 2B(x - x_o)(y - y_o) + C(y - y_o)^2} \tag{3.2}$$

with

$$\begin{aligned} A &= \tfrac{1}{b^2}(f^2 \cos^2\theta + \sin^2\theta) \\ B &= \tfrac{1}{b^2}(1 - f^2)\cos\theta\sin\theta \\ C &= \tfrac{1}{b^2}(f^2 \sin^2\theta + \cos^2\theta) \end{aligned} \quad . \tag{3.3}$$

Here, $f = b/a$, where a and b are the major and minor semi-axes of the basal ellipse, respectively, and θ is the angle between the major and east-west (x) axes. A circular polynomial seamount can be simplified further with

$$r = \frac{\sqrt{(x - x_o)^2 + (y - y_o)^2}}{r_o}, \tag{3.4}$$

where r_o is the radius of the seamount base.

Figure 3.1 demonstrates the similarity between the polynomial (red line) and Gaussian (black dotted line) models and compare these models with the VGG signal (black solid line) over a typical truncated cone. The dense core model [Kim & Wessel, 2010] was employed to predict the free-air gravity (FAA) anomalies arising from the density differences and flexed crust (Figure 3.1b). Then, the VGG signal was estimated by taking the vertical derivative of the predicted FAA data. The polynomial model is generally close to the Gaussian model, except at the base, as mentioned above. However, the width of the VGG data is wider than either model. Such differences depend on the mass distribution of the seamount implied by the truncation level, the ratio between its height and basal radius and the amount of flexure underneath the seamount. Predicting such details would require more geophysical information (e.g., bathymetry and seismic refraction profiles). Thus, the polynomial model serves as a simple approximation to typical VGG anomalies over seamounts.

Because seamounts are volcanic constructs, their gravity anomalies protrude up-

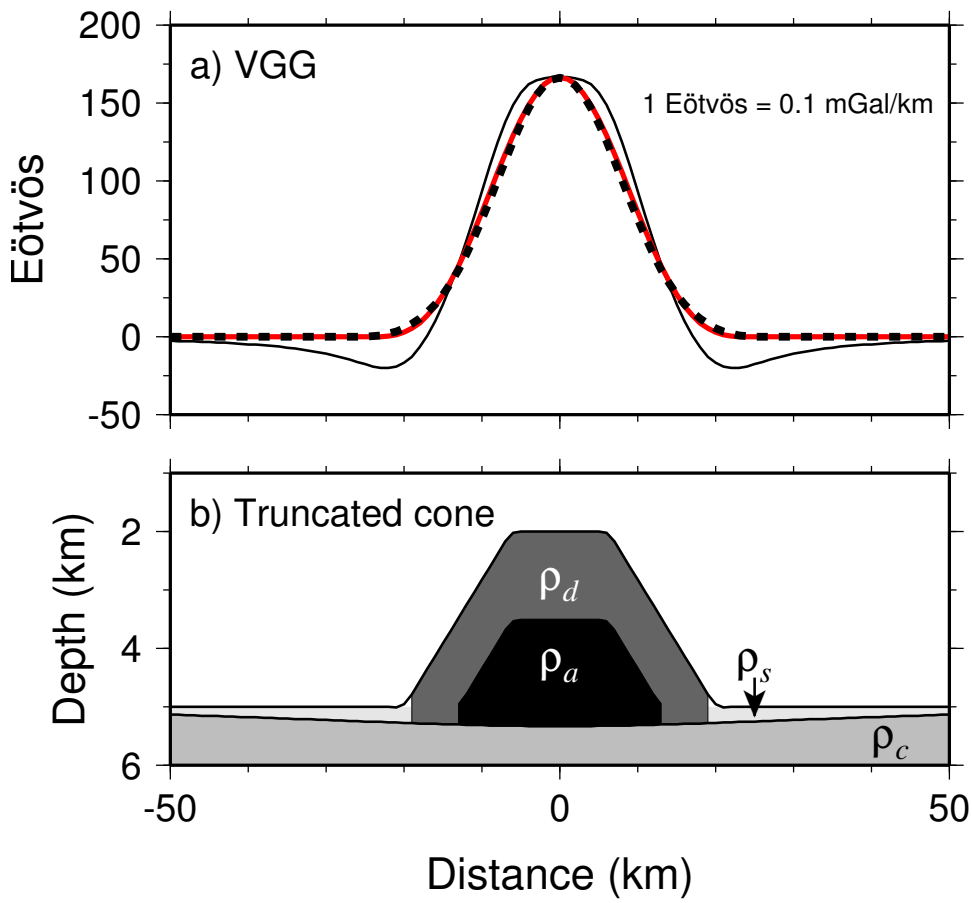

Figure 3.1: Polynomial seamount model. a) The vertical gravity gradient (VGG) signal (black solid line) due to a truncated cone shown in (b) is approximated by the polynomial (red line) and Gaussian (black dotted line) seamount models. b) Truncated cone with the dense core model [Kim & Wessel, 2010]. The densities of edifice (ρ_d), core (ρ_a), peripheral (ρ_s), and crust (ρ_c) are 2500, 2900, 2300, and 2900 kg m^{-3}, respectively.

wards from the regional gravity level. In the following, I will describe how I fit the elliptical polynomial model to such protuberances in the VGG grid. Obviously, not all positive VGG bumps indicate the presence of seamounts since other tectonic features (e.g., abyssal hills and fracture zone scarps) can result in similar signals. Thus, I will first construct a set of "potential" seamounts parameterized by the elliptical polynomial model and then apply statistical model selection criteria and both automatic and manual inspections in order to eliminate most unrealistic potential seamounts.

3.3.2 Nonlinear inversion for elliptical polynomial seamounts

If a given domain has S elliptical polynomial seamounts, I can construct a least-squares problem for estimating the six parameters, $\mathbf{m} = (p, x_o, y_o, a, b, \theta)$, for each polynomial seamount by minimizing

$$E(\mathbf{M}_S) = \sum_{i=1}^{N} \left[\frac{V_i - R_i(\mathbf{M}_S)}{\sigma_i} \right]^2 - 2\gamma \sum_{j=1}^{S} \ln p_j, \tag{3.5}$$

where N is the number of data points used for the fit, V_i is the observed VGG at the ith data point and σ_i the standard deviation of data noise. Here, R_i is the predicted VGG at the ith data point using $\mathbf{M}_S = (\mathbf{m}_1, \mathbf{m}_2, \ldots, \mathbf{m}_S)$. Thus, the first term in eq. (3.5) is a standard chi-squared measure of misfit between the observed and predicted data. The second term is a positivity constraint on the amplitude parameters, p_j, with a logarithm barrier, γ [Li & Oldenburg, 1996; Baptista et al., 2005].

As eq. (3.5) is nonlinear, I construct a set of linear equations based on the Levenberg-Marquardt method [Press et al., 1992]:

$$\textstyle\sum_{l=1}^{M} \alpha_{kl} \delta m_l = \beta_k, \quad k = 1, N. \tag{3.6}$$

where

$$\begin{aligned} \alpha_{jj} &\equiv (1+\lambda)\tfrac{1}{2}\tfrac{\partial^2 E}{\partial m_j^2} \\ \alpha_{jk} &\equiv \tfrac{1}{2}\tfrac{\partial^2 E}{\partial m_j \partial m_k} \qquad (j \neq k) \ . \\ \beta_k &\equiv -\tfrac{1}{2}\tfrac{\partial E}{\partial m_k} \end{aligned} \tag{3.7}$$

Here, $M = 6S$ is the total number of the model parameters in $\mathbf{M}_S$ and λ is a non-dimensional adjustment factor. I start the iteration with an initial set of $\mathbf{M}_S$ and update the model parameters as follows:

(a) Compute $E(\mathbf{M}_S)$

(b) Pick modest values for γ and λ. For this study, I used $\gamma = 10^5$ and $\lambda = 10^{-4}$.

(c) Solve the linear system in eq. (3.6) for δm and evaluate $E(\mathbf{M}_S + \delta m)$

(d) If $E(\mathbf{M}_S + \delta m) \geq E(\mathbf{M}_S)$, increase λ by a factor of 10, decrease γ by a factor of 2, and go back to (c).

(e) If $E(\mathbf{M}_S + \delta m) < E(\mathbf{M}_S)$, decrease both λ and γ by a factor of 10, update $\mathbf{M}_S$ with $\mathbf{M}_S + \delta m$, and go back to (c).

The iteration stops when $\gamma < 10^{-5}$ and $E(\mathbf{M}_S + \delta m) - E(\mathbf{M}_S) < 0.001$. The logarithm term increases the gradient of the misfit if the amplitude keeps decreasing toward negative and hence ensures that solutions with negative amplitudes are avoided.

However, the derivatives of the elliptical polynomial model with respect to (a, b, θ) become too unwieldy because both eqs. (3.2) and (3.3) are necessary. Instead I obtain derivatives with respect to the intermediate parameters (A, B, C). Thus, the derivatives of the model with respect to the six parameters are

$$
\begin{aligned}
\tfrac{\partial R}{\partial x_o} &= 2D\left[A(x-x_o) - B(y-y_o)\right] \\
\tfrac{\partial R}{\partial y_o} &= 2D\left[-B(x-x_o) + C(y-y_o)\right] \\
\tfrac{\partial R}{\partial p} &= \tfrac{R}{p} \\
\tfrac{\partial R}{\partial A} &= -D(x-x_o)^2 \\
\tfrac{\partial R}{\partial B} &= 2D(x-x_o)(y-y_o) \\
\tfrac{\partial R}{\partial C} &= -D(y-y_o)^2
\end{aligned}
\quad , \tag{3.8}
$$

where

$$
D = p\frac{2(1+r)^2(1-r)^2(1+2r^2)}{(1+r^2)^2}. \tag{3.9}
$$

Once the solution to eq. (3.5) has been determined, I formulate an eigenvalue problem that recovers the original parameters (a, b, θ) from (A, B, C) by substituting f^2 in A and C with that of B, i.e.,

$$
\begin{aligned}
A\cos\theta - B\sin\theta &= \tfrac{1}{a^2}\cos\theta \\
-B\cos\theta + C\sin\theta &= \tfrac{1}{a^2}\sin\theta
\end{aligned}
\quad . \tag{3.10}
$$

The above terms can be rewritten as the following 2x2 system:

$$
\begin{bmatrix} A & -B \\ -B & C \end{bmatrix}
\begin{bmatrix} \cos\theta \\ \sin\theta \end{bmatrix}
= \frac{1}{a^2}
\begin{bmatrix} \cos\theta \\ \sin\theta \end{bmatrix}. \tag{3.11}
$$

Using the two eigenvalues and eigenvectors of eq. (3.11) I can easily calculate (a, b, θ) from

$$
\begin{aligned}
a &= \sqrt{1/\lambda_e^1} \\
b &= \sqrt{1/\lambda_e^2} \\
\theta &= \tan^{-1}(\nu_y^1/\nu_x^1)
\end{aligned}
\quad , \tag{3.12}
$$

where the smaller eigenvalue is indicated by the superscript 1. Hence, the angle from the x-axis to the major axis is obtained using the eigenvector (ν_x^1, ν_y^1) associated with λ_e^1 because it points toward the major axis.

3.3.3 Data noise and statistical model selection

Like other geophysical data, the VGG has noise due to measurement and theory errors. While the measurement error is due to instrumentation (e.g., range precision of altimeter) and ambient noise (e.g., ocean waves and tide model error), the theory error derives from the simplified parameterizations of Earth models and idealized treatment of forward problems [Sandwell & Smith, 1997]. To improve the accuracy of the recovered gravity field, researchers enhanced the range precision of the existing altimetry measurements by better constraining the sea surface slope errors [Maus et al., 1998; Sandwell & Smith, 2005]. As a result, the signal-to-noise ratio of the current VGG data (v. 16.1) has been improved more than 40% [Sandwell & Smith, 2009].

In addition to the data noise present in the VGG grid, I introduce additional errors. Because eq. (3.5) does not include a complete set of parameters representing every geophysical phenomenon captured in the VGG data (e.g., gravity signals due to abyssal hills, fracture zones, and crustal density variations), the VGG signals not related to seamounts become the theory error. The elliptical polynomial model also contributes to the theory error as the model cannot handle completely the irregularity of VGG anomalies. In general, one can address this issue by adopting a more accurate model or by incorporating a measure of error correlations into the inversion formulation [e.g., Dosso et al., 2006]. The former is the very reason I chose the elliptical model because it is a more appropriate model than the circular models used in previous studies [Wessel & Lyons, 1997; Hillier & Watts, 2007]. However, developing a complete Earth model to explain every detail of the gravity field is impractical. Thus, I set an amplitude threshold (p_{cut} = 10 Eötvös) that the VGG amplitude of potential seamounts must exceed, by assuming that VGG peaks lower than this threshold are more likely to be associated with data noise or small-scale geologic features (e.g., abyssal hills) than actual seamounts. This threshold is about

twice the standard deviation of observed VGG anomalies in regions void of major geologic features (see insets in Figure 3.2). In addition, I ameliorate the theory error further by performing regional-residual separation on the VGG grid and subject the seamount model to both automatic and manual inspections (section 3.3.4).

However, error correlations are generally unknown and require reasonable assumptions about the data uncertainty distribution. A common approach is to assume that errors follow a Gaussian distribution and are spatially uncorrelated, which enables the use of σ_i in eq. (3.5) (i.e., a diagonal covariance matrix). Unfortunately, this approach becomes less effective in describing the data uncertainty distribution of the VGG grid because the errors in the raw altimetry measurements become correlated through data processing. In this case, one can estimate a full data covariance matrix with off-diagonal elements from the residual data (i.e., the observed data minus the predicted model) using an iterative procedure [Montgomery & Peck, 1992; Dettmer, 2006; Dosso et al., 2006]. For my study, however, incorporating a full data covariance matrix into eq. (3.5) becomes very expensive in terms of computation time because a NxN matrix would need to be inverted at each iteration as the model parameters get updated. In addition, the iterative approach has been successfully applied only to 2-D datasets (e.g., acoustic measurements at a hydrophone) and hence requires careful consideration for 3-D data (e.g., the VGG grid). Neglecting the off-diagonal elements in eq. (3.5), therefore, may lead to underestimation of model-parameter uncertainties.

Here, I address the effect due to correlated errors by considering the following aspects. First, the uncertainties of the model parameters for VGG potential seamounts are not directly converted to uncertainties of the parameters for bathymetric ideal seamounts; that step involves additional forward modeling [e.g., Wessel & Lyons, 1997]. Several tests with synthetic noise and VGG seamounts also showed that the model parameters determined with a diagonal covariance matrix predicted the original

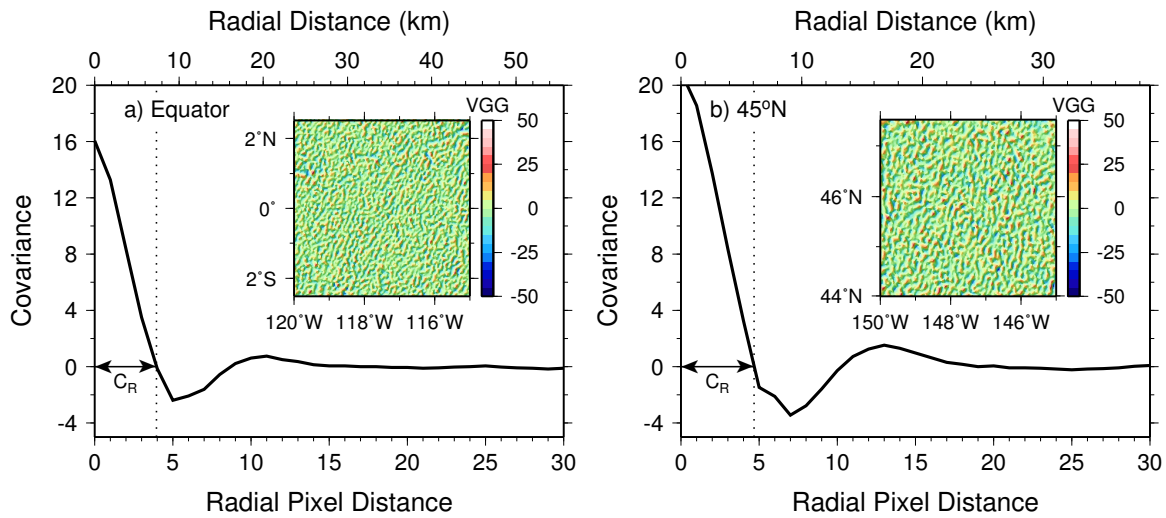

Figure 3.2: Correlation length of the VGG 16.1 grid. a) Radial covariance estimate of the VGG grid at Equator (inset). b) Radial covariance estimate of the VGG grid at ∼45°N (inset). Correlation pixel length, C_R, is the distance to the first zero crossing of the covariance estimates. Because these two areas do not have any large-scale geologic features, I use the standard deviations of these regions to determine the amplitude threshold, p_{cut}.

parameters in a consistent manner. Thus, I use eq. (3.5) with a diagonal covariance matrix (i.e., single standard deviation) and regard the best model parameters for VGG potential seamounts as a first-order approximation of actual VGG anomalies. Second, the parameter affected most by correlated data is the number of potential seamounts (S). Because this parameter is not solved for by eq. (3.5), I constrain S using statistical model selection criteria. However, such statistical tests inherently assume that each measurement is independent, which is invalid for the VGG grid due to its correlated nature. As a first-order correction, I determine the effective number of uncorrelated data, N_E, based on auto-covariance estimates of the VGG data and apply it to the model selection criteria.

For computational efficiency, I used the indirect method of computing auto-covariance estimates based on the Wiener-Khinchin theorem [Press et al., 1992]. In this theorem, an auto-correlation estimate is obtained by taking the inverse Fourier transform of the auto-spectrum estimate of a given data set. Then, an auto-covariance

estimate is simply computed by dividing the auto-correlation estimate by the number of given data points. I applied this procedure to two areas at different latitudes, where no significant geologic features were observed (Figure 3.2). Then, I averaged the 2-D auto-covariance estimates over one radial pixel distance (i.e., the distance between two neighboring grid points of the VGG data in the Mercator domain) and defined the correlation length of the VGG data using the first zero-crossing of the radial covariance estimates. The correlation length at Equator (Figure 3.2a) is ∼8 km, while the high latitude case (Figure 3.2b) is slightly better, at ∼6 km. This may be because the track spacing is closer at higher latitude and hence the noise is lower [Sandwell & Smith, 1997]. The radial auto-covariance estimates indicate that a VGG value at one grid node is strongly correlated with neighboring VGG values located within a radius of 5 pixels. Thus, I estimated the effective number of uncorrelated data, N_E, as

$$N_E = N/C_R^2 \tag{3.13}$$

where the correlation pixel length, $C_R = 5$, as shown in Figure 3.2.

Finally, I address the most important question of this study: How many VGG potential seamounts are necessary to optimally fit eq. (3.5)? Statistically, I can examine this question using model selection criteria (MSC) that test if a model with $S + 1$ seamounts significantly improves the misfit relative to a model with only S seamounts. One of the applied MSC is the Unbiased Akaike Information Criterion (AIC_u) [Tsai & McQuarrie, 1999] defined as

$$AIC_u = \ln\left[\frac{\sum_{i=1}^{N}(V_i - R_i(\mathbf{M}_S))^2}{N_E - M}\right] + \frac{N_E + M}{N_E - M - 2}. \tag{3.14}$$

Here, the first term is a measure of the misfit with S seamounts. However, if S is overestimated for a given dataset then AIC_u will be penalized by the second term (a

measure of model complexity). Thus, $AIC_u(\mathbf{M}_{S+1})$ becomes less than $AIC_u(\mathbf{M}_S)$ if the improvement in misfit made by a model with one more seamount, $\mathbf{M}_{S+1}$, is statistically significant. The other criterion considers the F-ratio test [Stein & Gordon, 1984], i.e.

$$F = \frac{\left[\chi^2(\mathbf{M}_S) - \chi^2(\mathbf{M}_{S+1})\right]/(M_{S+1} - M_S)}{\chi^2(\mathbf{M}_{S+1})/(N_E - M_{S+1})}, \tag{3.15}$$

where M_S is the number of model parameters for S seamounts and the chi-squared function is the same as the first term of eq. (3.5). This F-statistic is tested against the probability, $P_{0.05}(n_1, n_2)$ with $n_1 = (M_{S+1} - M_S)$ and $n_2 = (N_E - M_{S+1})$, for a 95% confidence level. Although both methods tend to result in the same statistical outcome, I conservatively only accept a model that passes both tests. Using the above MSC, therefore, I arrive at the number of potential seamounts that are statistically significant for the given VGG data with correlated noise.

3.3.4 SeaHunt: Automated global seamount search

Regional-residual separation

Long-wavelength signals apparent in the FAA data are inherently suppressed in the VGG data. However, some undulations are still noticeable, especially along major seamount chains surrounded by small negative amplitudes (e.g., Figure 3.3a). Since this regional variation is not directly associated with the seamounts themselves, I separated short-wavelength signals from the regional background by applying a spatial median filter with a 400 km filter width to the entire VGG grid [Smith, 1990; Wessel & Lyons, 1997]. The filter width was chosen so filtering would not affect seamounts but instead approximate the regional trend [Wessel, 1998]. Although median filtering can be biased due to a sloping background [Kim & Wessel, 2008], the VGG data have a relatively flat background and hence such filtering bias was not a concern for

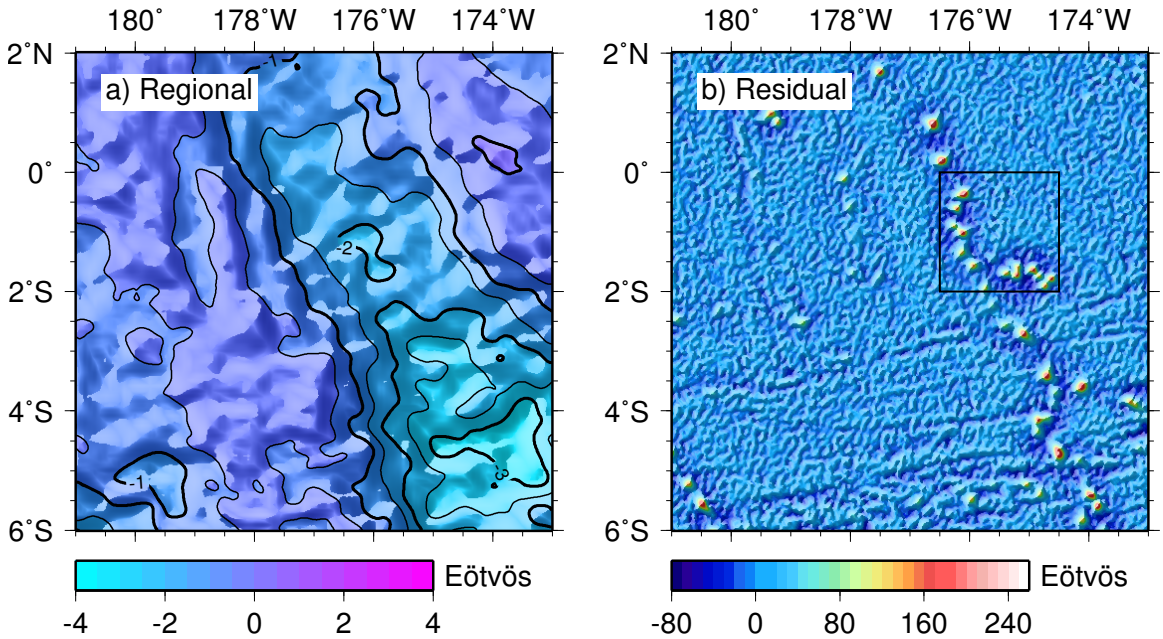

Figure 3.3: Regional and residual VGG over the Tokelau seamount chain. a) A gentle negative trend along the chain is apparent in the regional VGG. b) The residual VGG is obtained after subtracting the regional data from the raw VGG grid. A 2°-by-2° box used to demonstrate the automated searching method in the following figures.

this separation. Then, the regional trend obtained by median filtering was smoothed with a spatial Gaussian filter with 50 km filter width. The residual VGG data were obtained by subtracting the smoothed regional data from the original VGG data (Figure 3.3).

Dense grid contouring

The iterative inversion requires an initial set of model parameters that are constrained by the observed data. Among the six parameters, the misfit is most sensitive to the location and VGG amplitude of a polynomial seamount, i.e., (x_o, y_o, p). Thus, I decided to contour the residual VGG data using a 1-Eötvös interval and keep track of each contour, because seamounts produce positive gravity signals and hence their locations and amplitudes determine the geometry of their contours (Figure 3.4).

As an example (Figure 3.4a), if a given area has two seamounts (the VGG peak of seamount A is larger than that of seamount B), the contouring returns the first

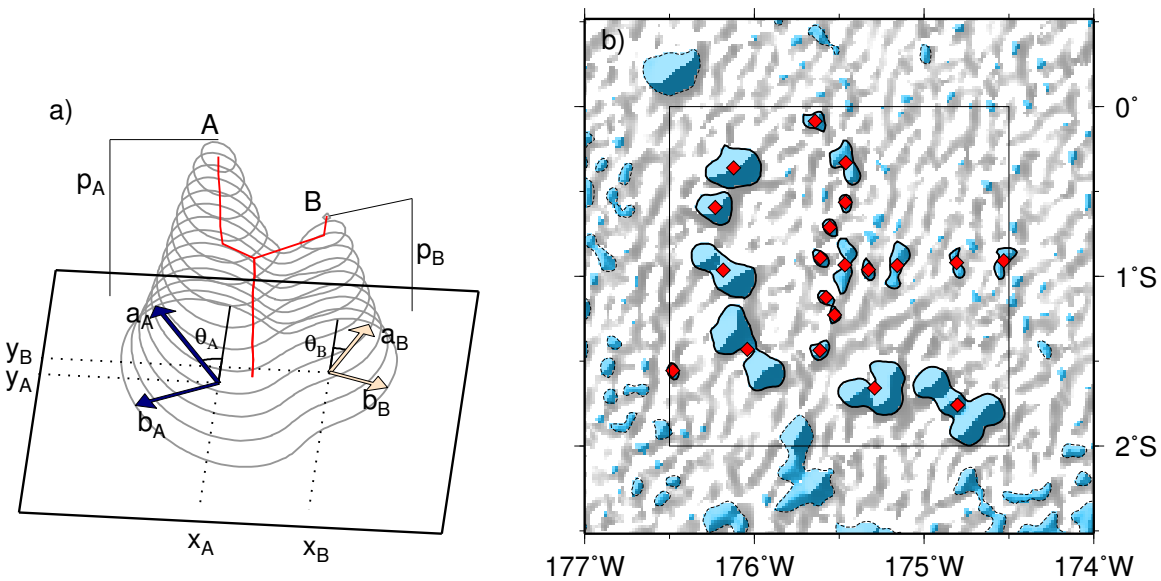

Figure 3.4: Contouring and base polygons. a) Schematic diagram of contouring when two VGG potential seamounts with different amplitudes are considered; see text for details. The model parameters are denoted for the potential seamounts, A and B. b) Base polygons inside the small inversion box (thin solid line), which is designed only for demonstration purpose (Figure 3.3b). The actual inversion box is 5°-by-5° as discussed in text. The colored areas indicate VGG exceeding the threshold ($p_{cut} = 10$ Eötvös), while those outlined by dashed lines are larger than the area threshold (50 km^2). The red diamonds are the centers of basal ellipses fitted to the base polygons. Thus, I choose the base polygons (thick sold line) by examining whether their centers are inside a given inversion box.

closed polygon at the summit of seamount A. Whenever a new polygon is generated, the process estimates its area and determines a best-fit ellipse to that polygon, which usually has an irregular shape. This step parameterizes all polygons (i.e., contours) generated and enables me to recover these geometrical parameters at any contour level. As contouring proceeds, it tests if a new polygon encompasses the previous polygons. When the contouring reaches the summit of seamount B, the process results in two distinct polygons: one is from seamount A and the other is the first polygon due to seamount B. Because the latter does not include any of the previous polygons from seamount A, the contouring can recognize this event from the above test and maintain the polygon set of seamount A separately from that of seamount B, assigning unique identification numbers to each set. At each interval, I progressively construct a database of the area of a closed contour, its center location, major and minor axes, and the azimuth of the best-fit ellipse to that contour. More importantly, the contouring gives me a maximum number of potential seamounts in a given area because the first contour of each unique polygon set is associated with a positive VGG bump that may result from an actual seamount. Thus, an initial parameter set can be constructed by using the centers (x_o, y_o) of best-fit ellipses for the first contour level, p, for each feature.

For my global seamount analysis, I first divided the Earth into 25 plate-size domains based on a digital model of plate boundaries [Bird, 2003] by merging relatively smaller plates with their nearest neighbor plates (Table 3.1). For example, the Banda Sea, Burma, Molucca Sea, and Timor plates were processed together with the Sunda plate. Then, I generated 5°-by-5° boxes (called inversion boxes) that filled any given plate-size domain entirely.

For each plate-size domain, I extracted a sub-region grid from the residual VGG grid. Because the contouring keeps track of only closed contours, the area of the sub-region grid was enlarged so that contours extending outside the plate boundary

polygon (i.e., open contours) would become closed within the larger domain. Then, I carried out the contouring for the 25 sub-region grids at the specified interval (i.e., 1 Eötvös) down to the amplitude threshold (p_{cut} = 10 Eötvös). I used the p_{cut} contours as base polygons, inside which potential seamounts, if any, must be found. To reduce the number of spurious base polygons I only retained polygons whose area exceeded 50 km^2 (i.e., area threshold based on the correlation analysis of the VGG grid; section 3.5). This analysis yielded 415,710 initial candidates for potential seamounts.

To avoid unnecessary repetition and simplify computations, I assigned the data to the corresponding plate-size domain and then to its inversion boxes, based on the base polygons (Figure 3.4b). I assigned base polygons to the plate-size domain by examining if their centers are inside its boundary defined by the digital model of Bird [2003]. In the same way, the base polygons assigned to the plate-size domain were distributed further to the inversion boxes by determining if their centers were inside a given inversion box (Figure 3.4b). Then, I distributed VGG data and initial parameter sets to each inversion box according to the assigned base polygons, which encompasses both the data and initial peaks (Figure 3.5a). In this way, although the grid for a plate-size domain and its inversion boxes is rectangular, the actual shape of the data distribution inside an inversion box becomes irregular. Thus, I did not need to change the size of the inversion boxes or overlap the boxes in order to include data located along the irregular boundary of any plate-size domain.

Automated searching and step-wise inversion

The initial parameters (x_o, y_o, p) given by contouring are good initial choices for the location and VGG amplitude of potential seamounts, while the other parameters (a, b, θ) need to be determined directly by minimizing eq. (3.5). However, this non-linear system quickly becomes unstable if the initial guesses for the parameters (a, b, θ) are too distant from the actual values. Thus, I construct a step-wise inversion that

solves eq. (3.5) using the circular polynomial model and then refines the circular parameters to yield an elliptical polynomial model. The procedures A–D explained in this section were executed for each inversion box in a given plate-size domain. In addition, I parallelized the following procedures for an efficient search because the model parameters optimized for one box are independent from other boxes.

In step A, I determine a first-order approximation to the given VGG data using the circular polynomial model defined by eqs. (3.1) and (3.4). Although the circular model requires four parameters, (x_o, y_o, p, r_o), I fix the location and amplitude parameters at their initial values obtained from contouring throughout the first step and hence solve eq. (3.5) for r only. This simplifies eq. (3.6) and only requires the derivative

$$\frac{\partial R}{\partial r_o} = 2D\frac{r}{r_o}, \tag{3.16}$$

where D and r are defined in eqs. (3.9) and (3.4), respectively. In addition, the logarithm barrier in eq. (3.5) is applied to the radius parameter because the amplitude parameter is fixed for this step. Because each base polygon includes at least one potential seamount summit detected by contouring, I estimate the radius of the seamount with the largest amplitude first, add one more seamount, re-estimate the radii of the given two seamounts, and then use the MSC to determine if the added seamount is statistically significant in reducing the misfit. I repeat step A until it fails the MSC. By carrying out the above procedures on a base-polygon basis, I construct a set of circular seamounts that are statistically significant within their base polygon. The MSC, however, needs to use the actual number of the data points inside the base polygon, N, not N_E as the data points are too few to compute N_E for individual base polygons. Thus, I find S_1 circular potential seamounts from the initial set (red squares in Figure 3.5b) after rejecting statistically insignificant seamounts (blue squares in Figure 3.5b).

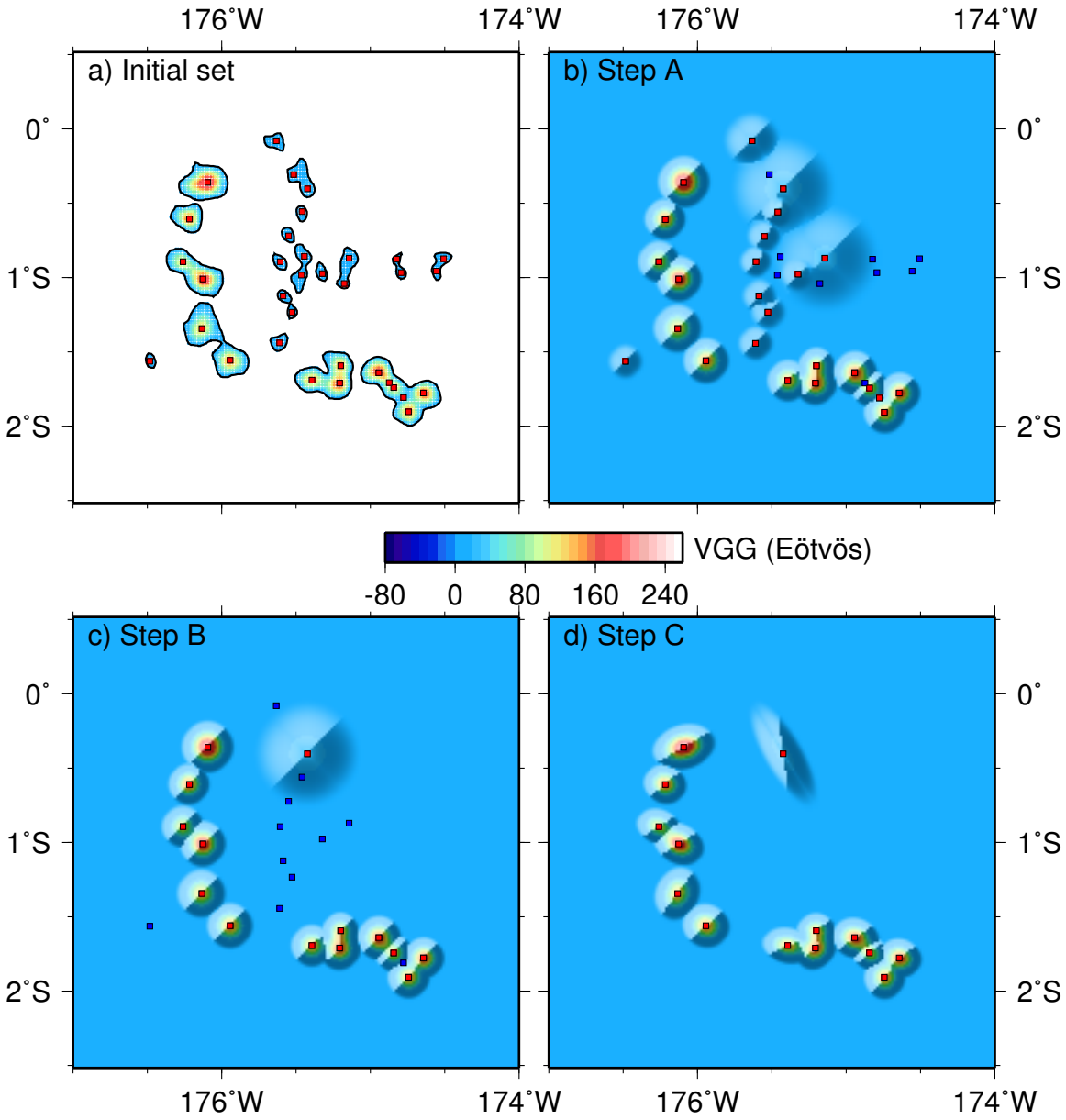

Figure 3.5: Automated step-wise inversion for seamount searching. a) The initial dataset consists of the VGG data inside the base polygons and the initial model parameters, (x_o, y_o, p), prepared by contouring (see Figure 3.4). The potential seamount locations are indicated by the red squares. b) Step A. The model selection criteria (MSC) are applied to identify statistically insignificant potential seamounts (blue squares) using the circular polynomial model. c) Step B. The potential seamounts (red squares) are further reduced after removing the potential seamounts (blue squares), which do not increase the misfit significantly when it is not included to the computation. d) Step C. The elliptical polynomial model is applied to approximate the given VGG data, however the parameters, (x_o, y_o, p), have been fixed as their initial values until this step.

In step B, I remove statistically insignificant seamounts (blue squares in Figure 3.5c) from the previous set by now applying the MSC to the entire inversion box. A tentative set of seamounts is constructed by removing one seamount from the starting set and using this reduced set to compute the MSC estimates with N_E, which represent the statistical significance of the removed seamount. Then, I generate another tentative set by adding back the removed seamount and removing another seamount from the starting set, and then re-compute the MSC estimates. By repeating this process, I construct a table of MSC estimates for the S_1 tentative sets. If the exclusion of a particular seamount does not make the misfit significantly worse, the MSC will result in both decreased AIC_u and F-ratio smaller than the critical value (i.e., $P_{0.05}$) for the tentative set without this seamount. This seamount, thus, is the least important feature in minimizing the misfit. After removing the least significant seamount from the starting set, I repeat the process with the new starting set now having $S_1 - 1$ potential seamounts. When all the seamount in the new set are statistically significant, the MSC estimates will have increased either the AIC_u or F-ratio beyond their critical values. Thus, I can terminate step B and obtain S_2 circular potential seamounts (red squares in Figure 3.5c).

In step C, I determine the parameters, (a, b, θ), for the elliptical seamount model using the radii of the circular potential seamounts as initial values, while the location and amplitude parameters are fixed as before. Because S_2 tends to be substantially reduced from S_1, I exclude data points inside base polygons that have no potential seamounts after step B, prior to solving eq. (3.5) for the basal ellipse parameters (Figure 3.5d).

In the last step D, I solve eq. (3.5) for all six parameters of the given potential elliptical seamounts (Figure 3.6a). The location and amplitude parameters are not fixed in this stage and hence the logarithm barrier is properly applied to the amplitude parameter. This step uses the model parameters of step C as the starting values and

makes a fine adjustment to the parameters. For Figures 3.5d and 3.6a, the differences between the model parameters estimated by steps C and D are <10%. Thus, I obtained 110,127 potential seamounts from the inversion-based search and inspected them as discussed in the next section.

3.3.5 Automatic and manual inspections

As the VGG grid is derived from sea surface height measurements, the altimetry tracks become discontinuous over large subaerial landmasses. Although a complicated gridding scheme is applied to fill the altimetry data gaps and produce the VGG grid [Sandwell & Smith, 2005], the VGG data over continents and large islands (e.g., New Guinea) are poorly constrained. Another important aspect is that volcanic seamounts are unlikely to exist along continental margins. Thus, I defined Seamount Exclusive Zones (SEZs) using the 2000 m isobaths obtained from ETOPO2v2 [NGDC, 2006], which approximate the boundaries of the continents. The seamounts found inside or within 20 km distance from the SEZs (black lines in Figure 3.9) were automatically tagged to be excluded from list of the potential seamounts.

The model parameters estimated by my automated method can be biased because of the theory error, which results from the inability of the model to predict the noise in the VGG grid and non-seamount-related signals; both effects tend to overestimate the major axis (e.g., Figure 3.6a). By extending the major axes of small potential seamounts (usually with $p < 30$ Eötvös), the model is able to reduce the misfits in areas where the VGG grid is complicated by roughness of the seafloor (e.g., the Southwest Indian Ridge) and where linear trends are apparent (e.g., near fracture zones). I automatically tagged potential seamounts with unrealistic major axes if the major-to-minor axes ratio was less than 0.2 (i.e., $f \leq 0.2$) and if the ratio of the major axis to the VGG amplitude was larger than 0.7 (i.e., $a/p \geq 0.7$). These empirical and conservative conditions were used to exclude unrealistic potential seamounts.

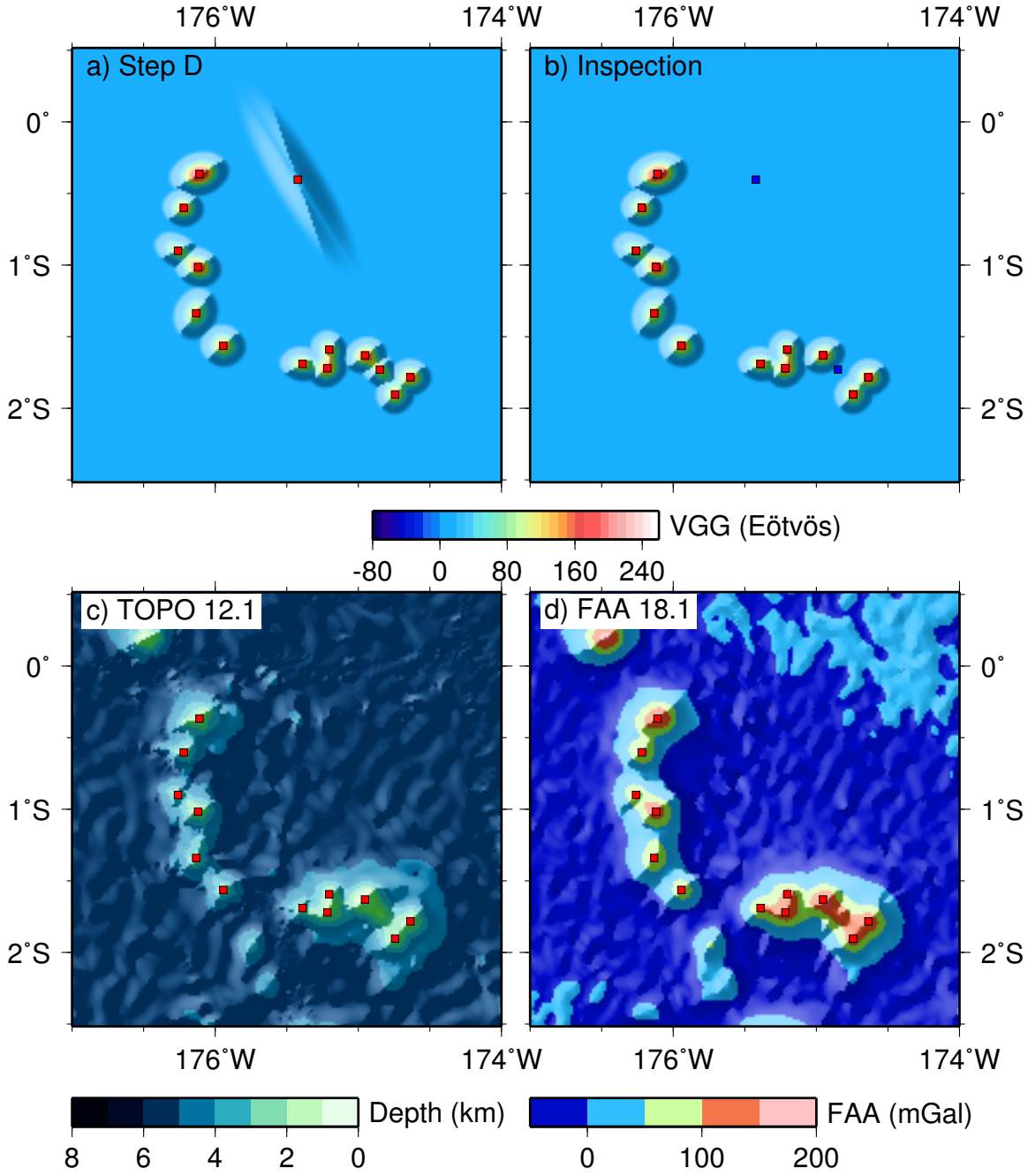

Figure 3.6: Full inversion and inspection. a) Step D. The six model parameters of the elliptical polynomial model are solved in this stage. b) Automated and manual inspections. The automatic inspection tagged a small potential seamount (blue square at 0.5°S) because it has a severely elongated basal ellipse as the inversion approximated the data noise, not a real feature. Another seamount (blue square at 1.5°S) was manually tagged after comparing (a) with both (c) the predicted bathymetry and (d) the free-air gravity anomalies.

Next, I compared the potential seamounts to the VGG, FAA, and predicted bathymetry (TOPO 12.1) grids using Google Earth. I manually tagged multiple peaks over flat-topped seamounts, stellate seamounts, and large islands, as well as peaks detected at volcanic ridges and over rough bathymetry. Manual inspection was necessary because I could not find any systematic relationship between my model parameters and the VGG over such morphologies. For example, a truncated seamount (e.g., guyot) exhibits relatively flat FAA variation over its summit and the slope of the FAA depends on the flatness of the truncated seamount and its density structure. The VGG derived from such a flat FAA field have multiple local maxima for a single seamount, which consequently causes the contouring to produce multiple initial peaks for that single seamount. For most cases, the MSC used with the automated inversion was effective in merging them into one summit, but not for large guyots (e.g., Pallada Guyot). As anticipated at the model building stage, the MSC was not fully successful in excluding initial peaks obtained at flanks of stellate seamounts, large islands and at volcanic ridges (e.g., Necker ridge). These multiple peaks were therefore tagged during the manual inspection (Figure 3.6). The model parameters of the manually edited potential peaks were reexamined when to convert the gravimetric parameters to the bathymetric parameters (see section 3.3.6). While I strived for consistency in making these decisions, it is clearly a subjective procedure.

Finally, I tagged islands based on distance to the nearest coastline. A volcanic island is a seamount rising above the sea surface. However, its exposed area above the sea surface varies considerably. Some islands exhibit large subaerial surfaces with high elevations, while others have small areas barely above sea level (e.g., atolls). In addition, the gravimetric center of a volcanic island is not always the same as the center of the subaerial surface. Due to these variations, no systematic approach to finding islands was made. Instead, I define an island if the distance to the nearest coastline from any subaerial point of the island is longer than 4 km. It means that the

length between the two closest ends of the island coastline is longer than 8 km. Given the VGG correlation length of ∼8 km (Figure 3.2), data gaps longer than 8 km cannot be constrained through nearby altimetry data points. Using this criterion, I could tag 62 islands from the manually inspected potential seamounts. After removing all tagged potential peaks from the list, I arrived at 25,721 potential seamounts.

3.3.6 Seamount height estimation

The model parameters of the identified VGG potential seamounts can be used for various studies: spatial distribution of seamounts [Craig & Sandwell, 1988; Wessel & Lyons, 1997], plate tectonic reconstructions [Jarrard & Clague, 1977], and refining absolute plate motions [Wessel & Kroenke, 1997]. The amplitude and basal ellipse parameters of the VGG potential seamounts, however, cannot be translated linearly to obtain actual dimensions and volumes of bathymetric seamounts, which are desirable when investigating intraplate volcanism [Wessel, 2001; Watts et al., 2006; Hillier, 2007]. To address this problem, one can use either the predicted bathymetry from gravity [Smith & Sandwell, 1997] or a separate modeling scheme [Wessel & Lyons, 1997]. Because the former data were estimated based on the assumption of a constant elastic thickness, the height prediction can be biased, especially for large seamounts that were formed recently relative to the thermal age of the lithosphere beneath them (i.e., young seamount on old crust) [Dixon et al., 1983]. To remedy such bias, Wessel & Lyons [1997] estimated the height parameter from a simplified forward modeling that considered a broad range of elastic thicknesses. They assumed the seamount had a circular Gaussian shape and built a look-up table for a wide range of heights and flank slopes in order to relate their gravimetric parameters (i.e., VGG and FAA amplitudes and zero-crossing distance) to the height and radius of the seamount model. However, the uncertainty of the predicted height is greater for small seamounts (< 3 km) than for large seamounts because the flexural signals due to small

seamounts are inherently less significant than those due to the large ones [Wessel & Lyons, 1997]. Thus, the uncertainty of the height parameter for small seamounts predicted without bathymetry becomes similar in both approaches. For the large seamounts ($>$ 3 km), the simple seamount model becomes inadequate because of their stellate form; however, many of these have been mapped bathymetrically. In this study, therefore, I obtain the bathymetric parameters (i.e., actual height, major, and minor axes) for the VGG potential seamounts from the predicted bathymetry, TOPO 12.1 [Smith & Sandwell, 1997], because it includes shipboard measurements wherever available.

As seen in Figure 3.7a, the basal ellipse (black solid line) of a VGG seamount is generally narrower than the actual basal ellipse (red solid line) of the corresponding bathymetric seamount. To estimate the height, I discretely scaled the basal ellipse of the VGG seamount by 0.5, 2, 3, and 4 (see the concentric ellipses in Figure 3.7a). For each scale I computed the median of the depths sampled at the four positions where the major and minor axes intersect the basal ellipse (see the red and black dots in Figure 3.7a). The height estimate for each seamount is summit depth (black square in Figure 3.7a) minus the median depth. Then, I compared five different height estimates and chose the height only when the examined scale resulted in a 50% increase in height over the previous estimate (Figure 3.7b). In Figure 3.7, the height estimate is increasing continuously with scaling, however the height is not increased by more than 50% for scales larger than 3. Although this ratio constraint prevents excessive stretching and enables me to construct less overlapping basal ellipses (Figure 3.8), I anticipate that the height estimates for tall seamounts ($h > 4$ km) may be underestimated by $\sim$15%. Based on the estimated heights, I found 24,643 potential seamounts taller than 100 m out of 25,721 VGG seamounts.

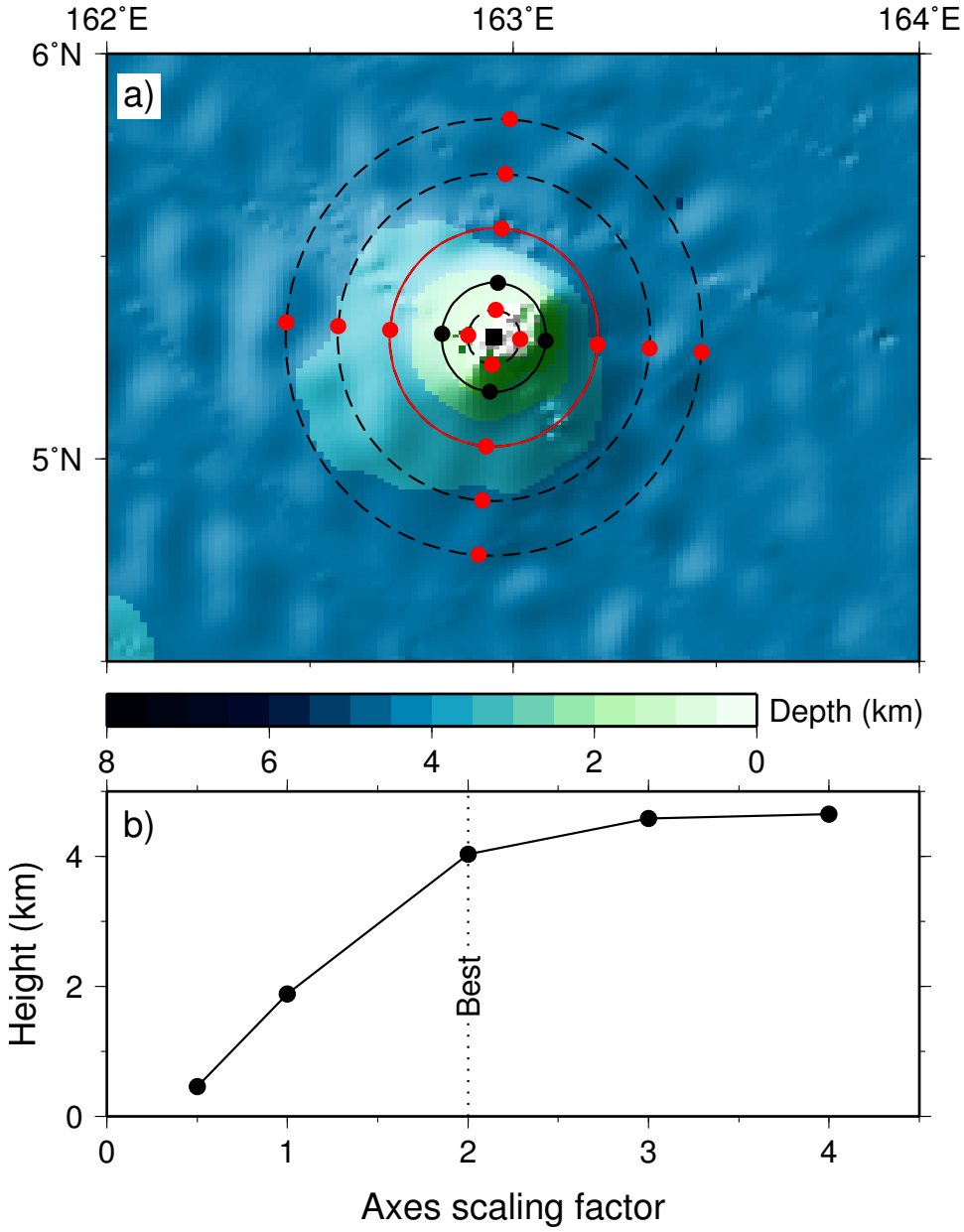

Figure 3.7: Height estimation from the predicted bathymetry grid, TOPO 12.1 [Smith & Sandwell, 1997]. a) Scaled basal ellipses. The basal ellipse of the VGG potential seamount (black solid line) is scaled discretely by 0.5, 2, 3, and 4 (dashed and red concentric ellipses). The depths are sampled from the intersecting points between the major and minor axes and the ellipses (black and red dots). b) Height estimation curve. The height is estimated by subtracting the regional depth (i.e., median value of the four depths from each scaled ellipse) from the summit depth (black square in (a)). The best scale is determined if the height at that scale is increased more than 50% relative to the previous height.

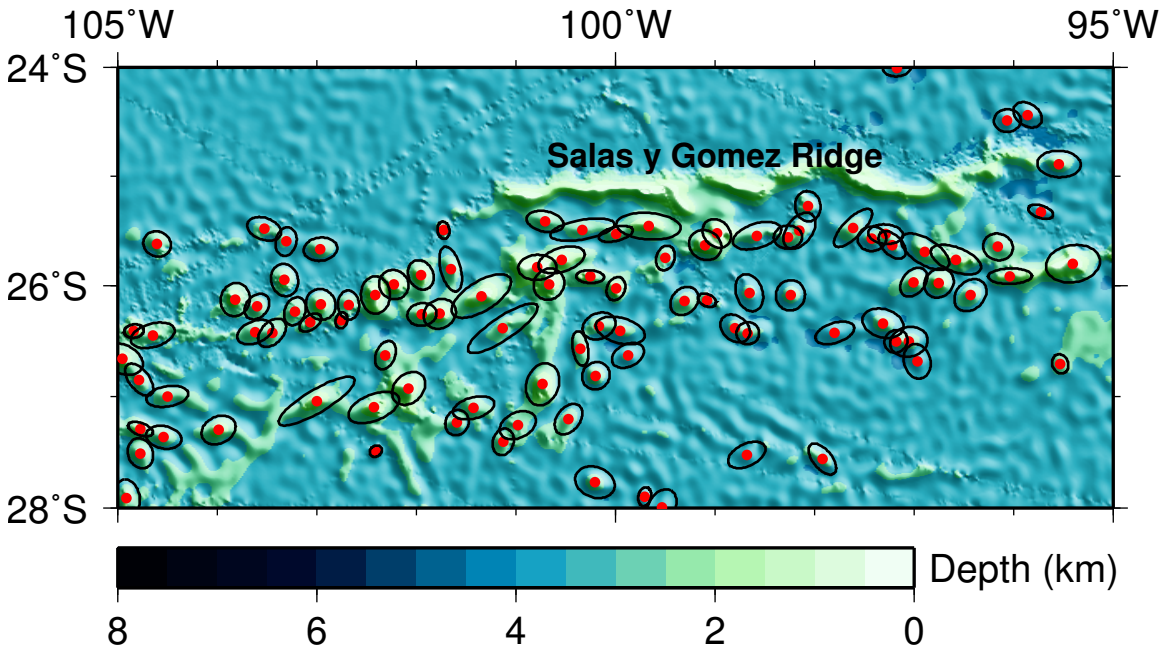

Figure 3.8: Bathymetric basal ellipses of potential seamounts scaled by the height estimation process. The locations (red dots) of potential seamounts are shown for a section of the Easter Seamount Chain. As discussed in the text, the Salas y Gomez Ridge at 25°S was manually excluded from the list of the potential seamounts.

3.4 Results

The total of 24,643 potential seamounts taller than 100 m was determined and characterized by the processes described above; this is almost twice the number identified in the previous study [Wessel, 2001]. However, the term "seamount" has been defined inconsistently in various studies due to the specific interests in a field of research or limitations of the data used in a study [Menard, 1964; Jordan et al., 1983; Wessel & Lyons, 1997; Wessel et al., 2010]. A recent attempt to include diverse views on seamounts within multidisciplinary research communities describes seamounts as "any geographically isolated topographic features on the seafloor taller than 100 m, including ones whose summit regions may temporarily emerge above sea level, but not including features that are located on continental shelves or that are part of other major landmasses" [Staudigel et al., 2010]. The automatic tagging with the SEZs, the manual tagging to deal with volcanic ridges, and the height threshold make my

potential seamount count more compatible with modern terminology than those of previous studies. Although I tagged 62 islands, my final seamount count still includes some small islands because the shortest width of their subaerial area is narrower than the correlated 8-km length of the VGG grid.

3.4.1 Spatial and height distribution of the potential seamounts

The spatial distribution of potential seamounts from this study (Figure 3.9) shows that seamounts taller than 1 km (blue and red dots, n = 8,458) generally occur in clusters, seamount chains, and arc regions, whereas large portions of the seamounts less than 1 km (black dots, n = 16,185) are located near mid-ocean ridges. This partitioning suggests that large seamounts are formed by mantle plumes or subduction, whereas small seamounts are produced in near-ridge environments [Wessel, 2001; Hillier, 2007]. A histogram of the height distribution of the seamounts (see inset in Figure 3.9) also illustrates that the population of small seamounts ($h < 1$ km) is about twice that of large seamounts ($h > 1$ km).

The Pacific plate supports ∼28% of the identified potential seamounts. However, nearly half of the world's seamounts taller than 1 km are found on the Pacific plate (Table 3.1), which confirms earlier results for the western Pacific [Craig & Sandwell, 1988; Wessel & Lyons, 1997; Hillier, 2007]. Following the Pacific plate, numerous seamounts are found on the Antarctica, Africa, Australia, South America, and Nazca plates. The rest of the seamounts of $h > 1$ km are distributed over the Africa, Australia, Antarctica, and Nazca plates. Unlike the Pacific, seamounts with $h < 1$ km on the Antarctica plate make up more than 80% of the seamounts. Although the seamount counts for the Philippine, Mariana, and Sandwich plates are small relative to the total number of global seamounts, nearly 60% of seamounts found on these plates are taller than 1 km. It may imply that arc volcanoes can grow taller than near-ridge volcanoes due to the relatively static magma source supplied by the subduction

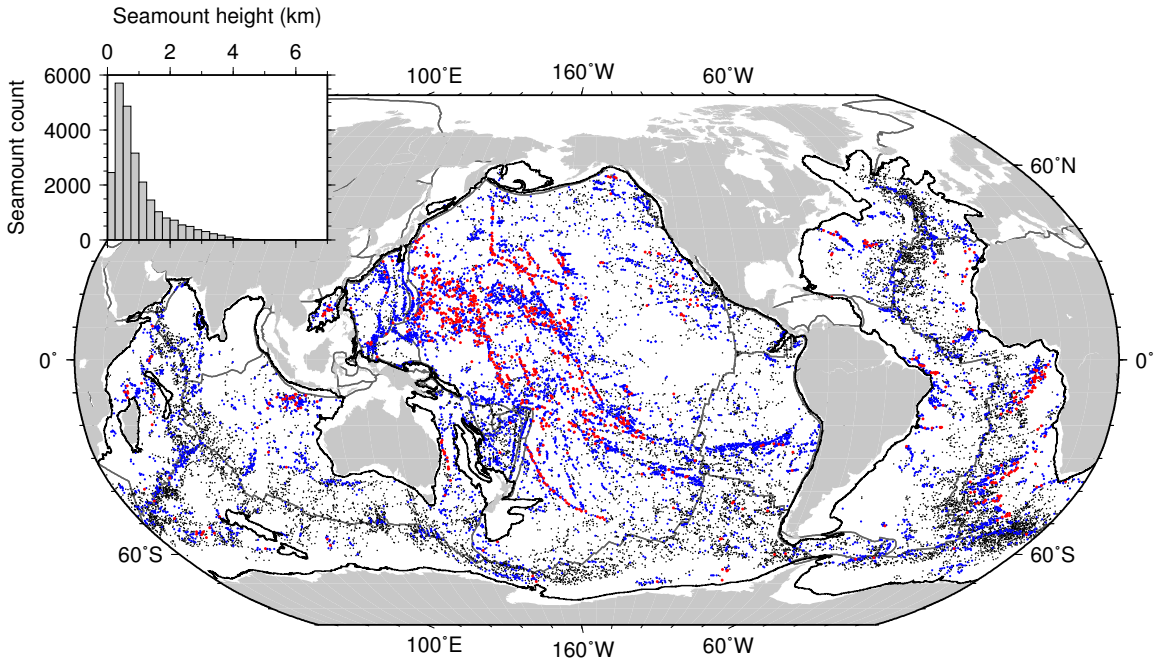

Figure 3.9: Global distribution of 24,643 potential seamounts identified by this study. Black dots for $0.1 \leq h < 1$ km ($n = 16{,}185$), blue dots for $1 \leq h < 3$ km ($n = 7{,}514$), and red dots for $h \geq 3$ km ($n = 944$). The plate boundaries [Bird, 2003] are shown as gray lines and the Seamount Exclusion Zones (SEZs) defined by the 2000 m isobaths are drawn as black lines. Inset shows histogram of height distribution of potential seamounts.

process.

In terms of seamount density (i.e., the ratio of seamount counts to the area of plate-size domain), the highest density is observed from the Philippine Sea and Mariana plates because of active arc volcanism. Anomalously high estimates for seamount density (e.g., Juan Fernandez and Sandwich plates) are because the area is substantially smaller than that of other plate-size domain. It is intriguing to note that the seamount density estimates for the Africa, Pacific, Antarctica, and Nazca plates are relatively consistent, although the spatial distribution of the potential seamounts for each plate is different (Figure 3.9). In addition, the South and North America plates have less seamount coverage than their conjugate plate (i.e., the Africa plate).

3.5 Discussion

With different methodology and data, one will obtain dissimilar numbers of seamounts [Wessel, 2001; Kitchingman & Lai, 2004; Hillier & Watts, 2007; Wessel et al., 2010]; this makes it difficult to reconcile these numbers. Using bathymetry, Hillier & Watts [2007] found 201,055 potential seamounts in the NGDC archieved single-beam ship bathymetry, whereas Kitchingman & Lai [2004] identified 14,287 potential seamounts in the ETOPO2 grid. In contrast, Wessel [2001] found 11,882 potential seamounts from the VGG 7.2 grid (recently revised from 14,675 after removing accidental duplicates [Wessel et al., 2010]). One can also differentiate these numbers further based on size threshold, data resolution, methodologies, and other factors. Here, I will focus on two aspects of the broad definition of a seamount [Staudigel et al., 2010] that earlier studies did not consider. The first aspect is that a seamount is "any geographically isolated topographic feature." Previous studies commonly identified local summits on volcanic ridges as seamounts, which are geographically continuous. As an illustration, I compare the potential seamounts from this study (KW; red dots)

Table 3.1: Number of seamounts identified for each plate-size domain. Seamount density is the ratio of seamount counts to the area of plate-size domain. The plate notations are from Bird [2003], except for the plate-size domains consisting of combined plates.

Plate-size domain	$h \geq 1$ km	Total ($h \geq 0.1$ km)	Density (10^{-6} km^{-2})
AF	857	3888	41.7219
AN	639	4837	38.0876
AO[a]	820	2855	34.7297
AR	6	47	4.5874
CI[b]	59	149	18.0341
CO	40	185	33.4222
CP[c]	1	1	0.163562
EA	3	9	26.6708
EU	76	532	5.42395
GP	0	2	26.9772
IN	99	356	16.7875
JF	0	21	25.5191
JZ	7	40	155.217
NA	182	705	3.49659
NZ	440	1112	41.5518
OA[d]	2	7	0.243989
PA	4055	6863	44.9719
PSM[e]	419	697	57.7222
RI	2	30	102.997
SA	373	1133	15.837
SC	37	134	39.8391
SD[f]	39	80	4.38698
SO	281	924	28.9264
SW	21	36	114.493

a. Includes AU, CR, KE, NI, BR, FT, NH, and TO plates.

b. Includes BH, MN, NB, SS, CL, MO, SB, and WL plates.

c. Includes CA and PM plates.

d. Includes AM, ON, OK, and YA plates.

e. Includes MA and PS plates.

f. Includes BS, MS, TI, BU, and SU plates.

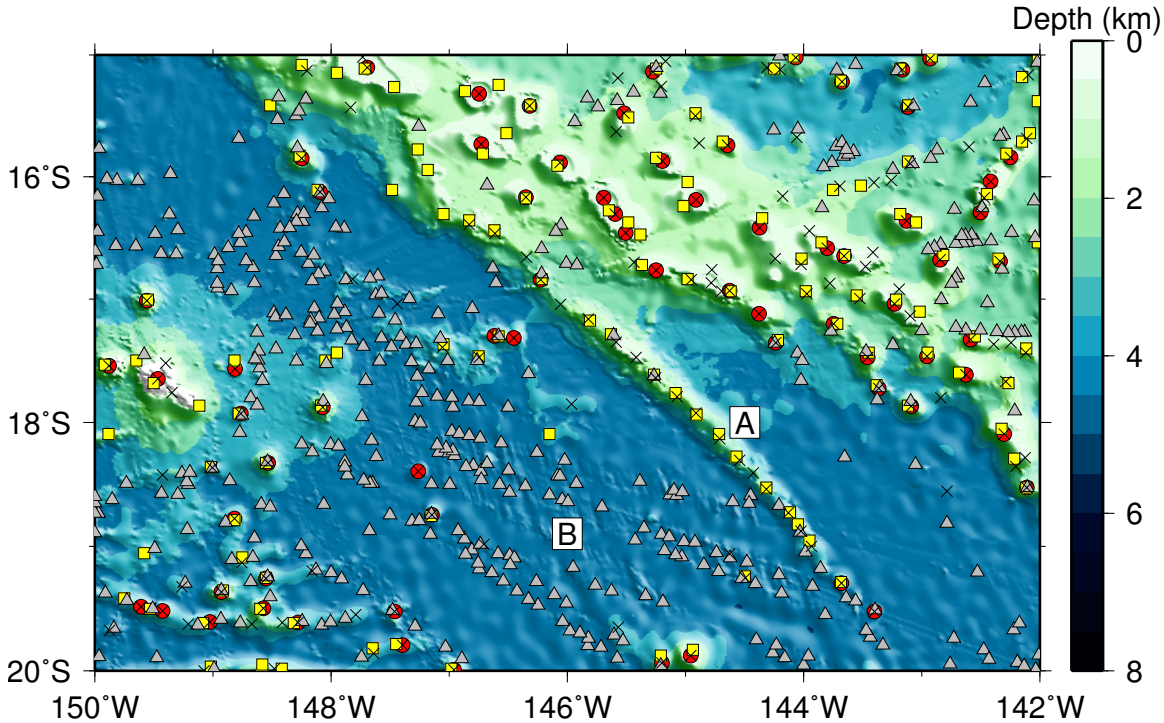

Figure 3.10: Comparison of potential seamounts identified by this study (red dots) with Wessel [2001] (yellow squares) and Hillier & Watts [2007] (gray triangles) near Tuamotu Plateau. Crosses indicate locations of uninspected potential seamounts in this study. The seamounts identified at the ridge (A) and along abyssal hills (B) biased the previous seamount counts.

with those of Wessel [2001] (PW; yellow squares) in the eastern part of the Tuamotu Plateau (Figure 3.10). Along the northwest-trending ridge (see A in Figure 3.10), PW has multiple seamounts whereas KW has none after the inspections (see crosses for the uninspected seamounts of KW). The second aspect is that seamounts are not "features that are located on continental shelves or that are part of other major landmasses." Because this geographical limitation was not imposed on the bathymetric studies [Kitchingman & Lai, 2004; Hillier & Watts, 2007], they found numerous seamounts along continental boundaries (e.g., within the Gulf of California). Thus, I can assume that any potential seamount in these databases located too far from any of the KW seamounts is unlikely to be a seamount according to this new definition. Furthermore, I can demonstrate how different and similar these databases are.

With this assumption, I make a first order reconciliation between the PW and HW [Hillier & Watts, 2007] seamount databases by choosing any seamounts in the PW and HW databases that are within 5 km of any of the KW seamounts. This distance (5 km) is a conservative limit that allows for differences in the data used to search for seamounts. My estimation shows that 5,461 seamounts (∼46%) of the PW data and 4,228 seamounts (∼2%) of the HW data are found within 5 km from the KW seamounts, while 2,208 (∼16%) seamounts from the KL [Kitchingman & Lai, 2004] data are within the reconciliation distance. For further comparison, I use the PW and HW datasets only because the KL data have the least number of reconciled seamounts.

The most significant difference between the PW and KW counts is observed for potential seamounts less than 3 km (Figure 3.11a). This reduction is expected as the PW data have multiple seamounts on linear ridges (e.g., Figure 3.10) and their predicted heights fall within that range ($1 < h < 3$ km). If the total volume of the non-reconcilable PW seamounts is linearly related to that of volcanic ridges, then the contribution of such ridges to intraplate volcanism can be significant because nearly half of the original PW seamounts are not found nearby the potential seamounts detected by my study. Thus, although I focus exclusively on seamounts in this study, the importance of volcanic ridges in understanding intraplate volcanism becomes self-evident. However, the reconciled PW data (PW|KW) still show many seamounts taller than 5 km, which KW does not have (Figures 3.11a). This means that the locations of these seamounts are close to each other except for the estimated heights, which leads to a further implication that these heights may be biased to some degree. The spatial distribution of these tall seamounts in the PW|KW data demonstrates that their heights are clearly over-predicted, because they would be islands in places where no islands exist (Figure 3.12). Disregarding these seamounts makes the KW and PW|KW more comparable (see blue squares and red dots in 3.11a). The difference

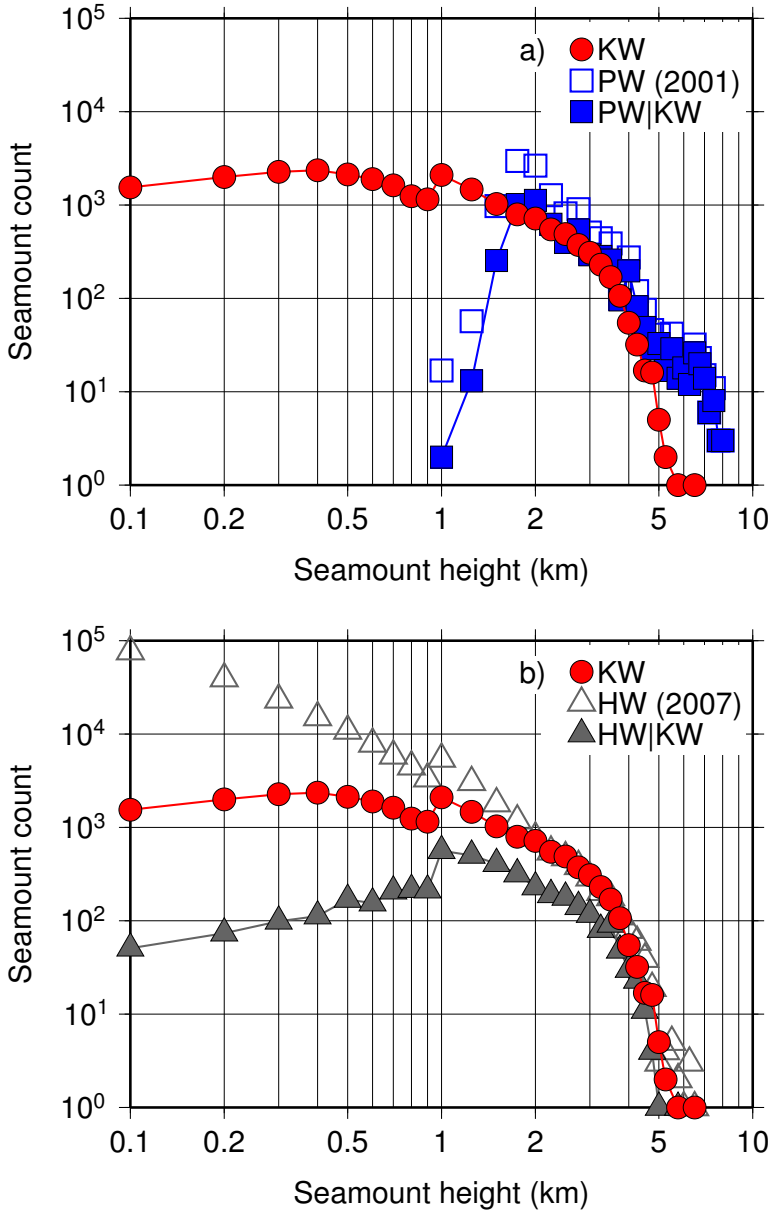

Figure 3.11: Height distribution of potential seamounts. a) Log-log plot of the height distribution of potential seamounts from the KW (this study; red dots), PW [Wessel, 2001] (blue open squares), and reconciled PW (PW|KW; blue squares). b) Log-log plot of the height distribution of potential seamounts from the KW, HW [Hillier & Watts, 2007] (gray open triangles), and reconciled HW (HW|KW; gray triangles).

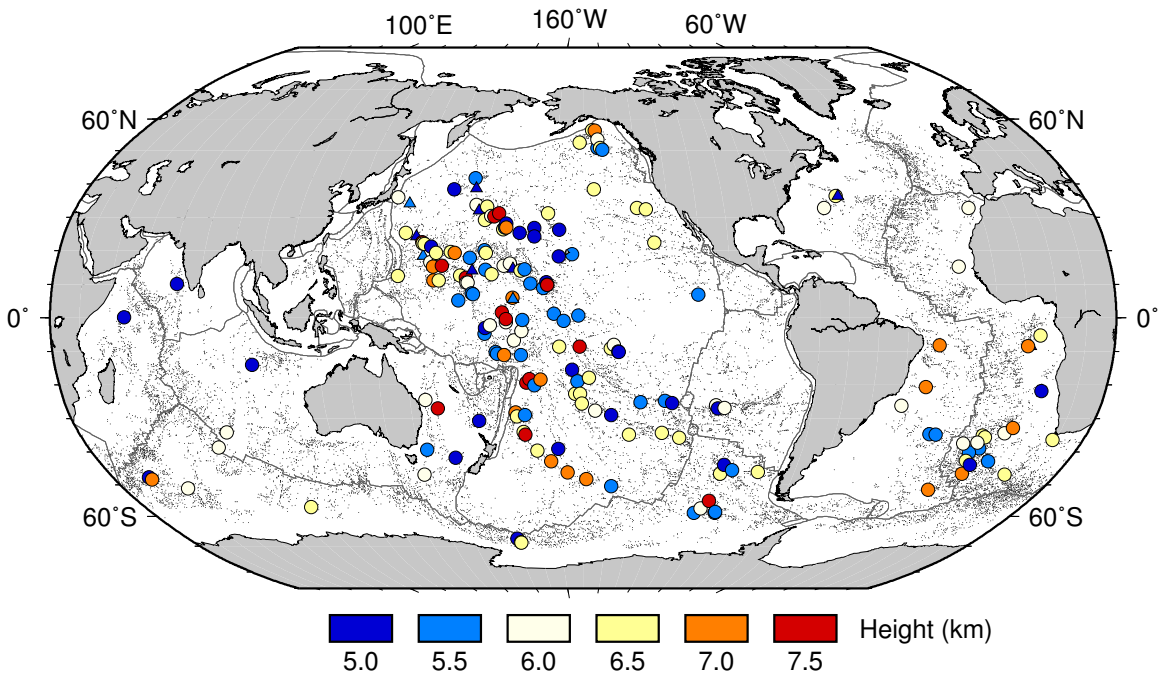

Figure 3.12: Spatial distribution of the PW|KW potential seamounts of $h > 5$ km in Figure 3.11. According to the predicted heights of these seamounts, we should see islands (circles) at places where such features cannot be found (e.g., Southeast Indian Ridge). Only a few of the large PW|KW seamounts are barely submerged (triangles). This clearly indicates that their heights are overestimated. The black dots are the KW potential seamounts.

between the HW and KW counts, however, increases as the seamount height decreases (Figure 3.11b). Although the general trend of the height distribution is similar to KW, the HW|KW has many fewer seamounts (especially at $1 < h < 3$ km) because of the sparse ship tracks (see gray triangles and red dots in Figure 3.11b). Taking into account the overestimated heights of the PW|KW data and the incomplete ship-track coverage of the HW|KW data, the similarity of all three seamount databases within $1 < h < 6$ km is noteworthy although these studies used different datasets and methods.

For small seamounts (< 1 km), however, no general trend is observed as both HW and HW|KW counts diverge from KW (Figure 3.11b). The direct comparison between KW and HW (see red dots and gray triangles in Figure 3.10) implies that HW identified abyssal hills (see B in Figure 3.10) as seamounts because heights and

length-scales of seamounts increasingly overlap with those of abyssal hills; furthermore, seamounts and abyssal hills are difficult to differentiate in one-dimensional profiles. In addition, it implies that the HW missed many small seamounts that I have detected. Thus, the HW count for small seamounts becomes questionable.

The gravity signals over small seamounts (< 1 km) can be ambiguous because of upward continuation, data resolution, altimetry noise level, seafloor roughness, and sediment cover [Wessel et al., 2010]. Because these are the main parameters that determine the maximum VGG amplitude of a seamount, I predicted VGG amplitudes for various cases by changing these parameters and defining the "detectability" of a seamount for a given depth and height by examining if its VGG amplitude exceeded a prescribed threshold [Wessel et al., 2010]. A truncated cone model was used to approximate the typical topography of seamounts, with basal radius of 4.5 times the height and fixed truncation ratio of 0.31 [Wessel, 2001]. As more than 60% of the seafloor has less than 200 m of sediments [Wessel et al., 2010], I assigned upper and lower limits on sediment thickness for the oldest seafloor (i.e., 180 Ma) as 600 m and 300 m, respectively. Sediment thickness, then, was linearly interpolated to the ridges (i.e., 0 Ma), which enabled me to relate sediment thickness to predicted depth of the seafloor formed at a given age [Parsons & Sclater, 1977]. By equating the predicted depth to the regional depth for a given seamount, I could examine the three cases of no sediments, minimum and maximum sediment thicknesses. In addition, I applied a second-order, low-pass Butterworth filter with a cutoff wavelength of 18 km to the predicted VGG signals [e.g., Marks, 1996] and kept only the linear term due to bathymetry [Parker, 1972]. By considering different scenarios using these constraints, I arrived at four "detectability zones" for seamounts (Figure 3.13). The high detectability zone (green domain) encloses seamounts exhibiting VGG amplitudes above the higher threshold (15 Eötvös), even when the maximum sediment thickness and the lowest density contrast between seamount (2500 kg m^{-3}) and sediment (2300

kg m^{-3}) were considered. In this zone, gravity over seamounts is easily distinguishable from gravity due to abyssal hills and data noise. The intermediate detectability zone (blue domain) represents seamounts having predicted VGG amplitudes above the lower threshold (10 Eötvös) when the minimum sediment thickness and the largest density contrast between seamount (2800 kg m^{-3}) and sediment (2000 kg m^{-3}) were considered. The low detectability zone (orange domain) encompasses seamounts with VGG amplitudes above the lower threshold when the less-dense seamount (2500 kg m^{-3}) and no sediment cover were considered. Finally, the null detectability zone (red domain) groups seamounts having VGG amplitudes less than the lower threshold because of upward continuation alone; the boundary between the orange and red domains was obtained without the low-pass filter.

In Figure 3.13, yellow dots show the seamount population found by this study. The majority of the potential seamounts are situated at 3–6 km depth. Seamounts deeper than 6 km were detected near subduction zones. About 35% of the potential seamounts are inside the red zone, although the seamount models that have VGG amplitudes less than the given threshold (10 Eötvös) define this zone. Yet, contouring and the automatic inspection ensured that all the identified seamounts have VGG amplitudes larger than this threshold. This mismatch implies that the detectability model under-predicts VGG due to the neglected nonlinear (i.e., higher order) terms of bathymetry, fixed ratio between height and radius, differences in the distributed mass between elliptical and circular cones, and fixed truncation ratio. Despite the gap between the real data and the simplified detectability model, many potential seamounts inside the red zone are still questionable (especially the small, deep ones) and may require ship bathymetry for confirmation.

The most fundamental limitation on seamount detection from gravity data is upward continuation. Figure 3.14a shows VGG predictions due to two closely spaced seamounts (4 km apart and 1 km tall) exhibiting a clear separation when the regional

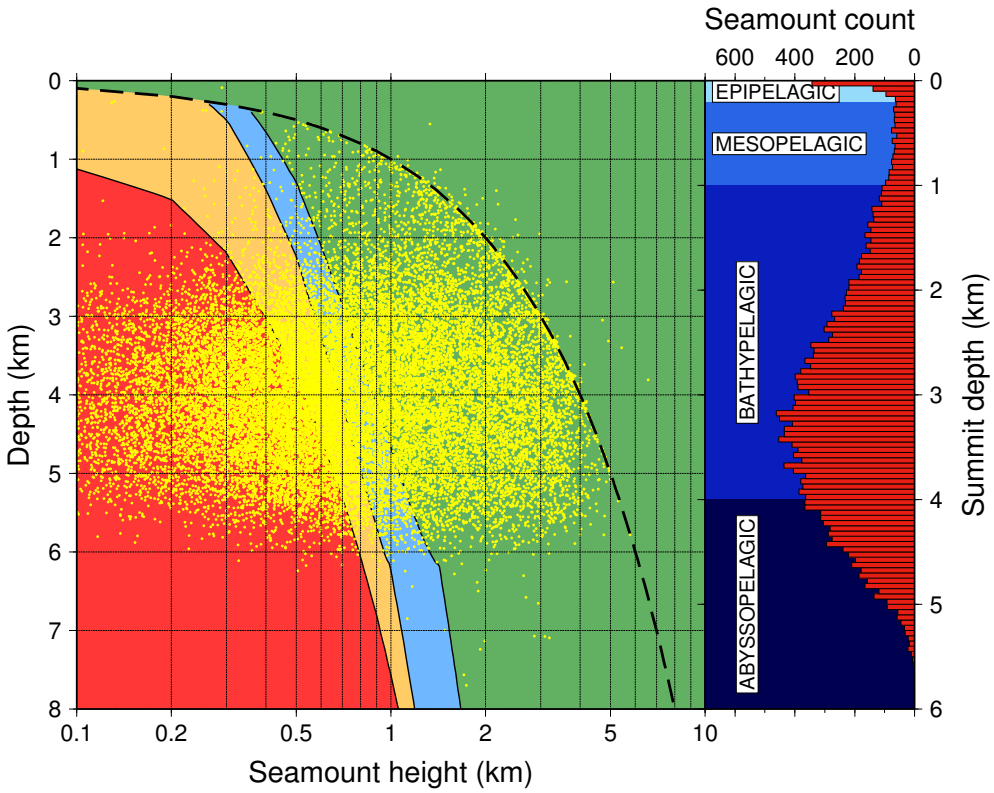

Figure 3.13: Modeled detectability zones for seamounts using VGG data. Each zone is based on maximum VGG amplitudes that reflect changes in seamount height, regional depth, density of seamount and sediment, thickness of sediment cover, and different noise level (see text for details). Seamounts in the green zone should be easily detected, whereas those in the red zone are problematic as they are too small for the given depths. Seamounts in intermediate zones (blue and orange) can be identifiable using robust methodology or better data. Yellow dots are the estimated heights from this study. The histogram of summit depths interestingly follows a normal distribution centered on ∼3-km depth and illustrates that seamounts have the potential to sustain epipelagic and mesopelagic environments crucial for marine animals. Modified from Wessel et al. [2010].

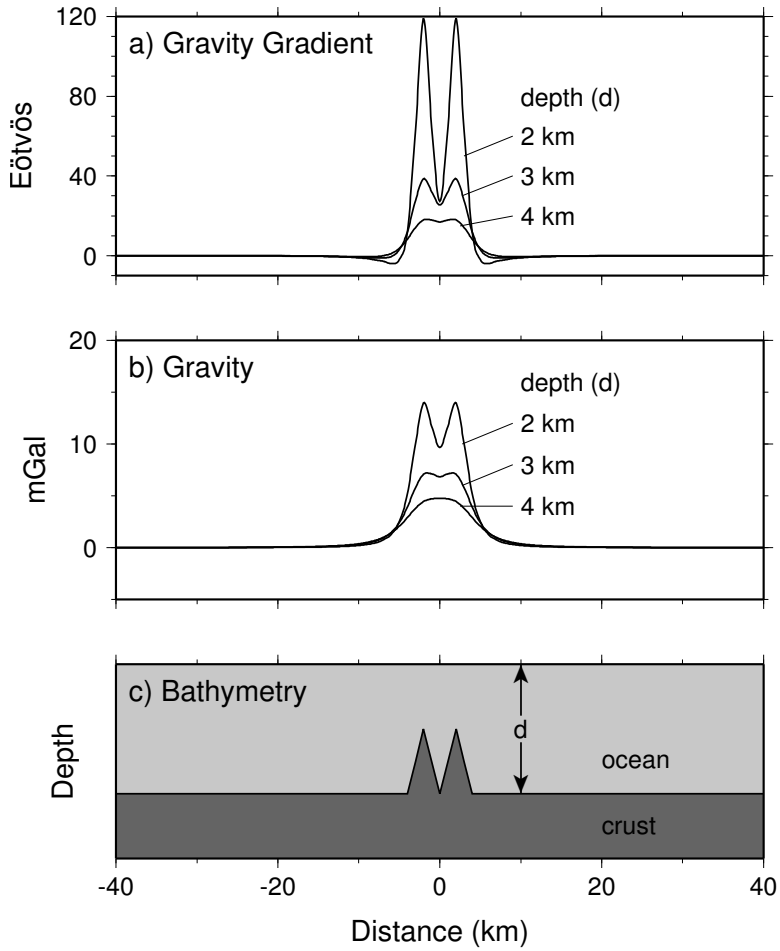

Figure 3.14: Limitation of topographic separation from gravity over closely spaced small seamounts. Two 1-km tall seamounts that are 4 km apart are considered for variable depths. Gravity anomalies over the seamounts become indistinct when the regional depth exceeds the size of seamounts. This upward continuation fundamentally limits my ability to detect seamounts. Modified from Wessel et al. [2010].

depth is 3 km or less, while the separation in the FAA predictions (Figure 3.14b) becomes indistinct from ∼3-km depth. Although this clearly demonstrates that the VGG is more suitable for finding seamounts than FAA, my seamount counts for the small seamounts (< 1 km) located in deep water (< 4 km) may be underrepresented. About 33% of the potential seamounts fall in this category.

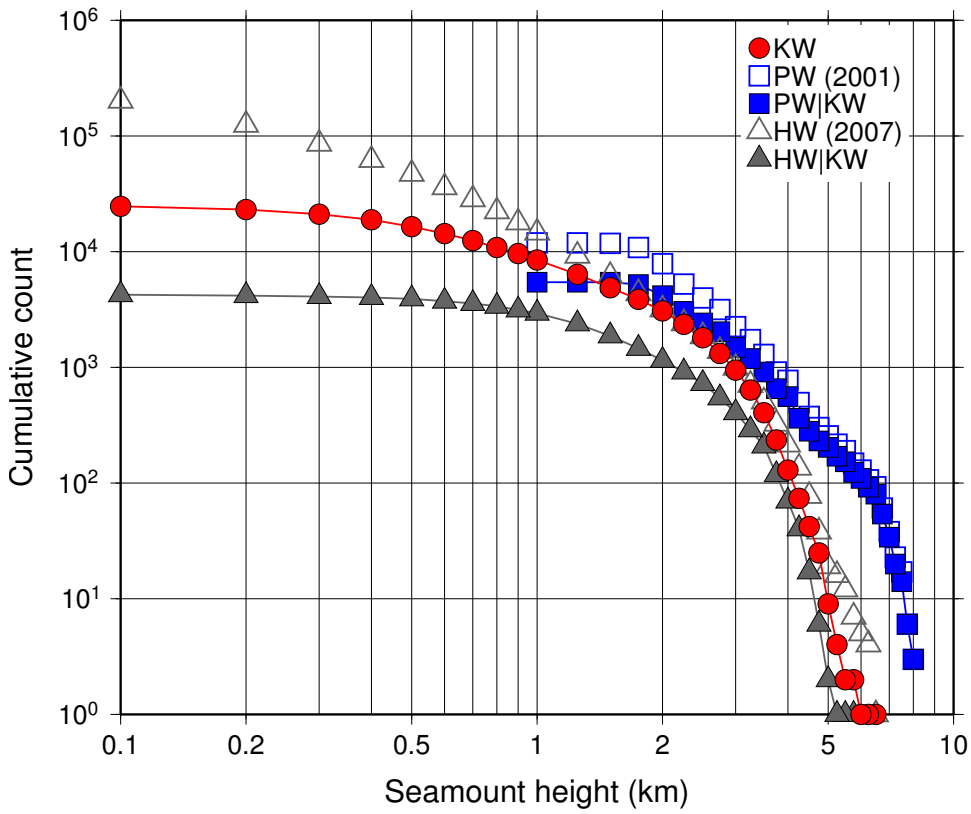

Figure 3.15: Height-frequency distributions of potential seamounts from KW (red dots), PW (blue open squares), PW|KW (blue squares), HW (gray open triangles), and HW|KW (gray triangles). The curvatures of the distributions are maximized at ∼3 km.

3.5.1 New global seamount census

The total number of seamounts for a plate or the Earth has been one of the core questions that previous studies have tried to answer, regardless of variable data coverage (incomplete or complete) and methodologies (manual or automatic) [e.g., Batiza, 1982; Jordan et al., 1983; Abers et al., 1988; Wessel, 2001; Hillier & Watts, 2007]. As a complete global determination of all seamounts has yet to be made, a number of uncounted seamounts has been obtained based on statistical extrapolation. This approach assumed that the height-frequency distribution follows either an exponential or power-law curve. Based on the choice of curve, the total number of seamounts for a region of interest could be fluctuating widely.

Wessel [2001] used a power-law relationship for the PW seamounts in the 2–7 km height range and predicted there might be 100,000 seamounts globally that are taller than 1 km. This number has been revised recently to 125,000 seamounts with an uncertainty range of 45,000–350,000 [Wessel et al., 2010]; however, the same power-law condition was used. The revised power-law height-frequency distribution also predicted 25 million seamounts taller than 100 m, but might range from 8–80 million. This power-law curve is a straight line in a log-log plot, and the linear trend of the PW data (see blue open squares in Figure 3.15) in the 2–7 km height range is well described by this empirical curve, as are the PW|KW data (see blue squares in Figure 3.15). Nevertheless, the over-predicted heights of the PW|KW seamounts bias this apparent power-low relationship and consequently inflate the predicted numbers for global seamounts.

Hillier & Watts [2007] corrected their counts to compensate for sparse data coverage and arrived at global predictions of 39,000 ($h > 1$ km) and 3 million ($h > 100$ m) seamounts. However, the comparison and reconciliation of the HW and KW data imply that the HW count (i.e., 14,582) for seamounts taller than 1 km are overestimated because the HW|KW count is only 2,931 (see triangles in Figure 3.15). Thus, the corrected number may be significantly lower than what was reported originally.

In this study, I find 8,458 potential seamounts globally that are taller than 1 km. If I consider the 62 counted islands and possible missing seamounts due to the SEZs and upward continuation, I can speculatively increase this number up to 10,000. Although this revised number is still lower than previous predictions, I am confident that this count for seamounts with $h > 1$ km is a reliable upper limit. In addition, the height-frequency curves derived from the KW and HW data have curved rather than linear trends, which led Hillier & Watts [2007] to conclude that no conventional empirical curves are adequate in describing seamount abundances over the entire height range. This finding is also directly applicable to my height-

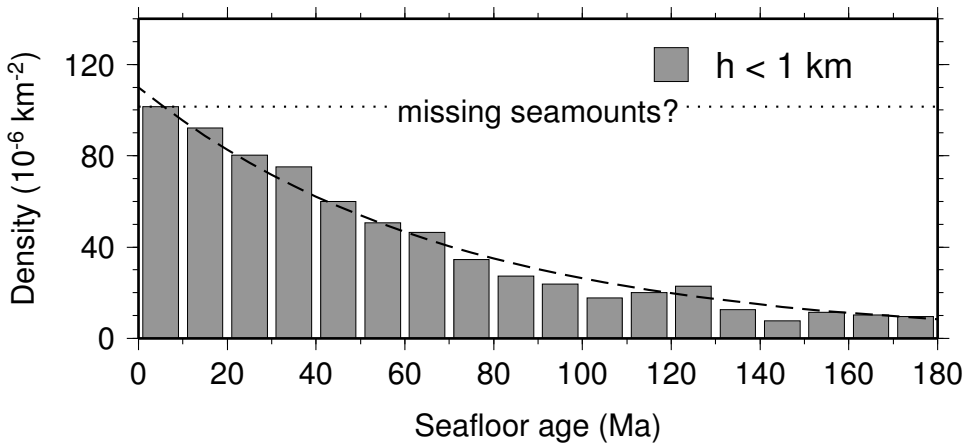

Figure 3.16: Seamount density for small seamounts ($0.1 < h < 1$ km) as a function of the seafloor age. The seamount density (i.e., the ratio of seamount counts to seafloor area for each age bin) decreases for older seafloor, indicating small seamounts are not likely detectable because their gravity signals can be subdued significantly due to greater water depth (see dashed curve) and thick sediment coverage. Crustal ages are sampled from the age grid 3.2 [Müller et al., 2008].

frequency curve (red circles in 3.15), which has its maximum curvature at ∼3 km and coincides (perhaps fortuitously?) with the transition height between circular and stellate seamounts [Mitchell, 2001].

Due to the non-statistical height-frequency distribution (Figure 3.15) and ambiguity of gravity signals due to small seamounts ($0.1 < h < 1$ km), I am only able to speculate about the "true" number of small seamounts globally by assuming that the seafloor is uniformly covered by small seamounts. Geologically, small seamounts are formed on young lithosphere near mid-ocean ridges [e.g., Smith & Cann, 1990]. This fact alone increases the detectability of these seamounts because the regional depth near the spreading ridges is typically shallower than other parts of the oceans [Parsons & Sclater, 1977] (i.e., less upward continuation) and the near-ridge areas have the least sediment cover [Wessel et al., 2010], and hence the confidence level of my count for small seamounts on the youngest seafloor is relatively higher than that for the older seafloor (Figure 3.16). If I can assume that the seafloor produced for any given geologic time period has experienced a constant seamount volcanism,

a given area of the seafloor will have a constant seamount density (Figure 3.16). If the seamount density of the youngest plate ($<$ 10 Ma) is a proxy for the "true" area coverage of small seamounts produced per 10 Myr for any geologic time period (Figure 3.16), I can predict that there are ∼30,000 small seamounts globally. If I impose a 50% uncertainty to the observed seamount density of the youngest plate, the predicted count for small seamounts becomes ∼45,000. This leads to a new global seamount census ($h > 0.1$ km) that ranges from 40,000–55,000. Of course, many of these smaller seamounts would be buried by sediments but could still give rise to a diminished gravity anomaly.

Nonetheless, the resolution of gravity is inherently limited by upward continuation. A chain of small seamounts ($h < 1$ km), thus, may be indentified as a single elongated seamount by my methods. The example of Figure 3.14 illustrates such a possibility because the VGG amplitude over closely spaced seamounts is larger than the threshold of this study, yet the shape of the VGG data appears as a blanket over them. For such cases, shipboard bathymetry is preferable.

Finally, I can assess to what extent potential seamounts have been mapped by surface ships. The histograms in Figure 3.17 show the ship data coverage per potential seamount by calculating Δs, the ratio of the number of shipboard measurements to the total number of grid points inside the basal ellipse. The TOPO 12.1 grid has embedded information that tells me whether a grid point is constrained by shipboard bathymetry or interpolated by the standard prediction [Smith & Sandwell, 1994]. Only 24% of the identified seamounts have more than 10% coverage of shipboard bathymetry (Figures 3.17a and 3.17b), while ∼40% of the potential seamounts have 0% ship coverage. The bathymetric coverage also differs for the size of seamounts (Figure 3.17c). About 90% of the small seamounts ($0.1 < h < 1$ km; black) have less than 10% ship coverage, while about 70% of the intermediate ($1 < h < 3$ km; blue) and large ($h > 3$ km; red) have the same coverage. However, the bathymetric

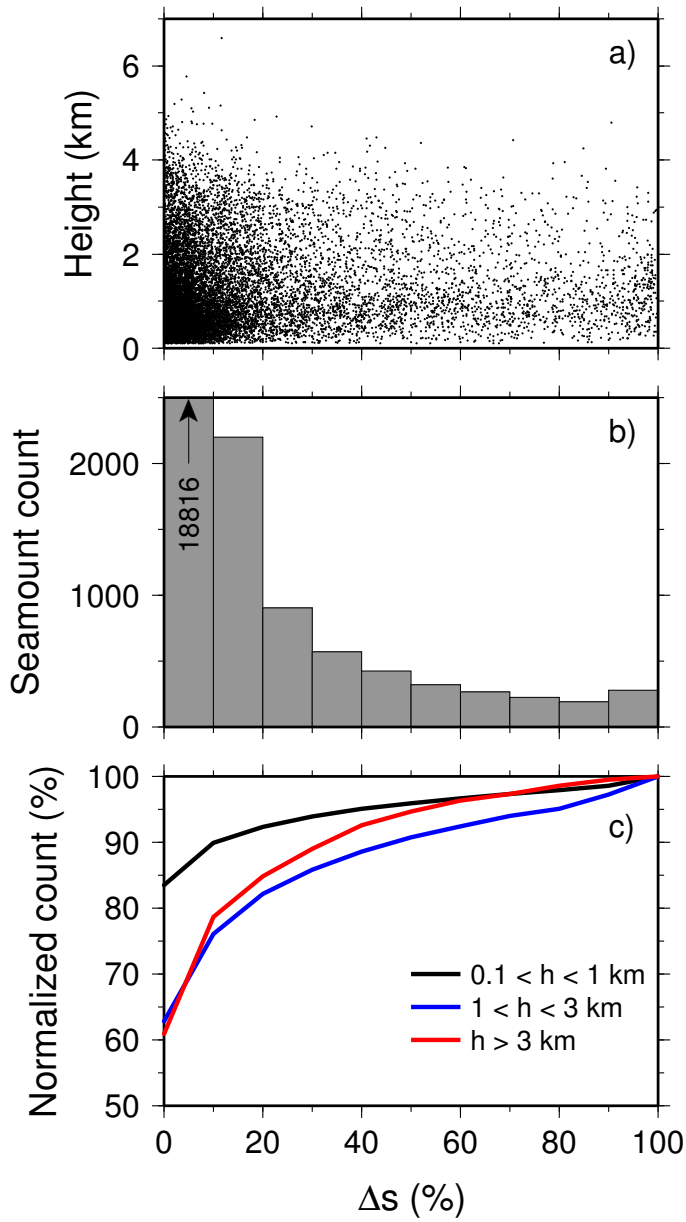

Figure 3.17: Bathymetric map coverage over potential seamounts. a) Scatter plot of the bathymetric map coverage versus seamount height. b) Histogram of bathymetric map coverage. Only 5,828 potential seamounts have more than 10% of their area mapped bathymetrically; 10,062 potential seamounts have not been mapped bathymetrically. c) Normalized cumulative count of small (black), intermediate (blue), large (red) seamounts as a function of bathymetric map coverage. The count is normalized with respect to the total number of seamounts for each seamount group.

coverage for the intermediate and large seamounts are quickly improved because they are easily locatable. To chart these poorly constrained seamounts effectively, one may use my seamount database to plan a survey or transit so that a survey ship can pass over one of these seamounts purposefully [Sandwell & Wessel, 2010].

3.6 Conclusions

For a global seamount analysis, I have developed a non-linear inversion method to search for potential seamounts from the satellite-derived vertical gravity gradient grid. The elliptical polynomial model was applied to approximate gravity anomalies due to seamounts. In addition, the statistical significance of each potential seamount was examined using the model selection criteria with the consideration of correlated gravity data. After making both automatic and manual inspections of potential seamounts determined by the inversion process, I isolated 24,643 seamounts with $h > 0.1$ km globally. In this count, the number of small seamounts ($h < 1$ km) is about twice larger than that of large seamounts ($h > 1$ km). The small seamounts are mostly found on the young seafloor and their counts decrease exponentially for old seafloor. This reflects my count for the small seamounts is fundamentally limited due to attenuated gravity signals of small seamounts at deep ocean (i.e., upward continuation). Because the size-frequency distribution does not follow typical empirical statistics, I have assumed a constant production of small seamounts at near-ridge environment and estimated a new census of global seamounts ($h > 0.1$ km) that ranges from 40,000–55,000. However, my new global seamount count is not significantly increased from the previous counts with the improved resolution of the VGG grid and a better methodology to characterize seamounts. The comparison of my seamount data with the previous global studies has demonstrated that the previous counts were inflated because of false counts at ridges and abyssal hills.

Chapter 4

Seamount Volcanism and Its Modulation by the Oceanic Lithosphere

4.1 Introduction

Being a key part of the great plate-tectonic conveyer belt, new seafloor is constantly formed at mid-ocean ridges while old seafloor is consumed at subduction zones. As the seafloor ages, subsides and moves away from its birthplace, it becomes littered with circular and elongated seamounts of all shapes and sizes. Much of this volcanism appears to be associated with excess magma production in the near-ridge-transform environment, while volumetrically a significant fraction is produced by intraplate volcanism. Because the existing seafloor has been formed at different times and produced during periods with different spreading rates, the population and volume distribution of the potential seamounts identified in Chapter 3 may reflect first-order temporal variations in seamount volcanism that may be correlated with such changes in the production of oceanic crust. In this chapter, I will examine the relationships between the distribution, shapes, orientations, and volumes of the potential seamounts with several aspects of the seafloor, such as crustal age, spreading rate at the time of crust formation, and seafloor fabric (here assumed to be the spreading direction) with respect to the orientations of elongated seamounts. To estimate the current seafloor age and past spreading rates beneath the potential seamounts, I use the improved

digital models of seafloor age and spreading rate [Müller et al., 2008]. The crustal age and spreading rate beneath 23,445 seamounts were obtained from these seafloor models (Figures 4.1 and 4.4).

4.2 Analysis and Discussion

First, I compare the spatial distribution of the global seamount population with the age of ocean crust (Figure 4.1). For this analysis, the total basal area of seamounts found for each age bin is obtained from their basal ellipses (see Chapter 3) and their total volume is estimated by assuming that all potential seamounts are an elliptical cone with a fixed truncation ratio of 0.31. The seamount count for each age bin (Figure 4.2a) shows that ∼43% of the potential seamounts are found on ocean crust younger than 40 Ma (covering about 40% of the dated seafloor) and 81% of these seamounts are of $h < 1$ km (see contrast between the narrow and wide columns). The number of large seamounts ($h > 1$ km) found on young seafloor (< 40 Myr) seem to reflect seamount chains produced by hotspots presently located near the East Pacific Rise, namely Pitcairn, Easter, and Macdonald [Steinberger, 2000] and other non-hotspot melt sources (e.g., mantle return flow) [White et al., 2006] (Figure 4.1), because the total volume of these large seamounts are more than twice than that of small seamounts (Figure 4.2c). However, the total basal area covered by the small seamounts is about twice that of the area covered by the large seamounts (Figure 4.2b).

If we assume that the majority of small seamounts found on young crust are volcanic products of near-ridge volcanism [White, 2005], the volume difference observed between the small ($h < 1$ km) and large ($h > 1$ km) seamounts (Figure 4.2c) strongly implies that intraplate volcanism is volumetrically a significant contributor to volcanic accretion of the young crust (< 40 Myr) apart from the seafloor-spreading process

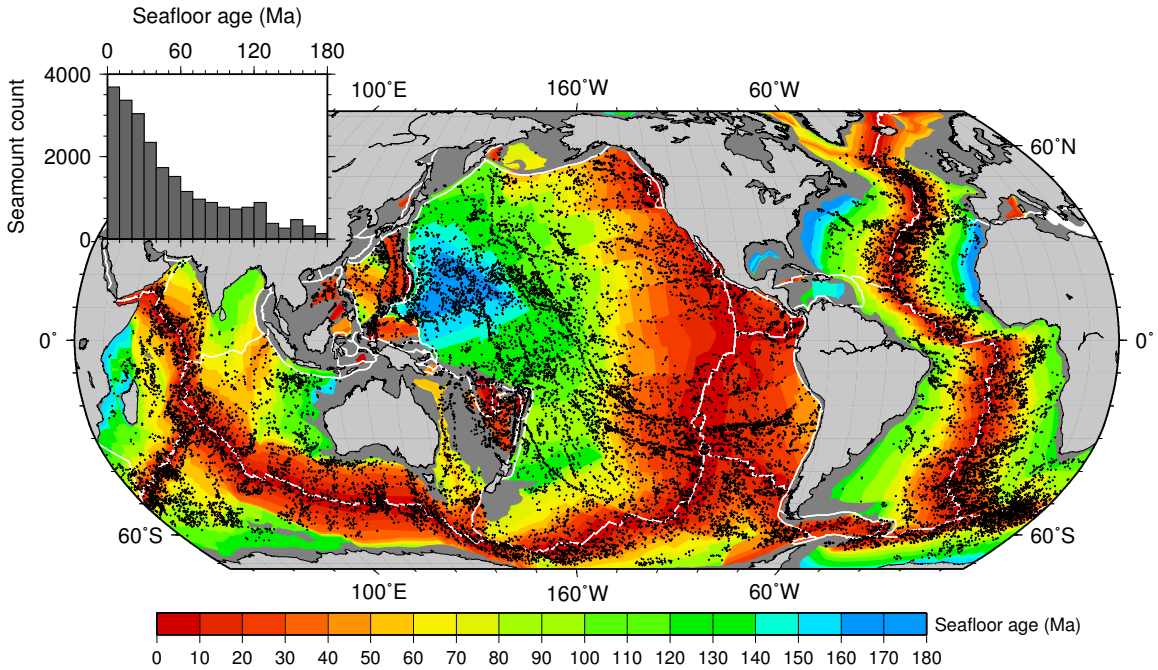

Figure 4.1: Potential seamounts (crosses) and seafloor age distribution. White lines are plate boundaries from Bird [2003]. The inset is a histogram of seamount counts versus seafloor age. The age grid version 3.2 is used [Müller et al., 2008]

itself. Interestingly, a linear growth in the total volume of the large seamounts (Figure 4.2c) starts at ∼70 Ma, which coincides with a typical onset age of small-scale sublithospheric convection [Fleitout & Yuen, 1984; Ballmer et al., 2007]. Although a detailed distinction between hotspot and non-hotspot seamounts has not yet been made for this first-order global analysis, the observed linear growth is nevertheless noteworthy. In addition, the total volume of the large seamounts found on the oldest plate segments of 170–150 Ma is comparable to that of the ocean crust that experienced the highest seamount production rates recorded by my data (130–100 Ma).

A more comprehensive and statistically unbiased picture of the age-seamount distribution can be obtained by normalizing the seamount counts (Figure 4.2a) by the total seafloor area of each age bin (Figure 4.2d). The area-age distribution shows an approximately linear fall-off from young crust to 160–180 Myr old seafloor (dashed line in Figure 4.2d). The density of seamount coverage per each age bin (Figure 4.2e) thus becomes the ratio of the seamount count to the corresponding seafloor area. The

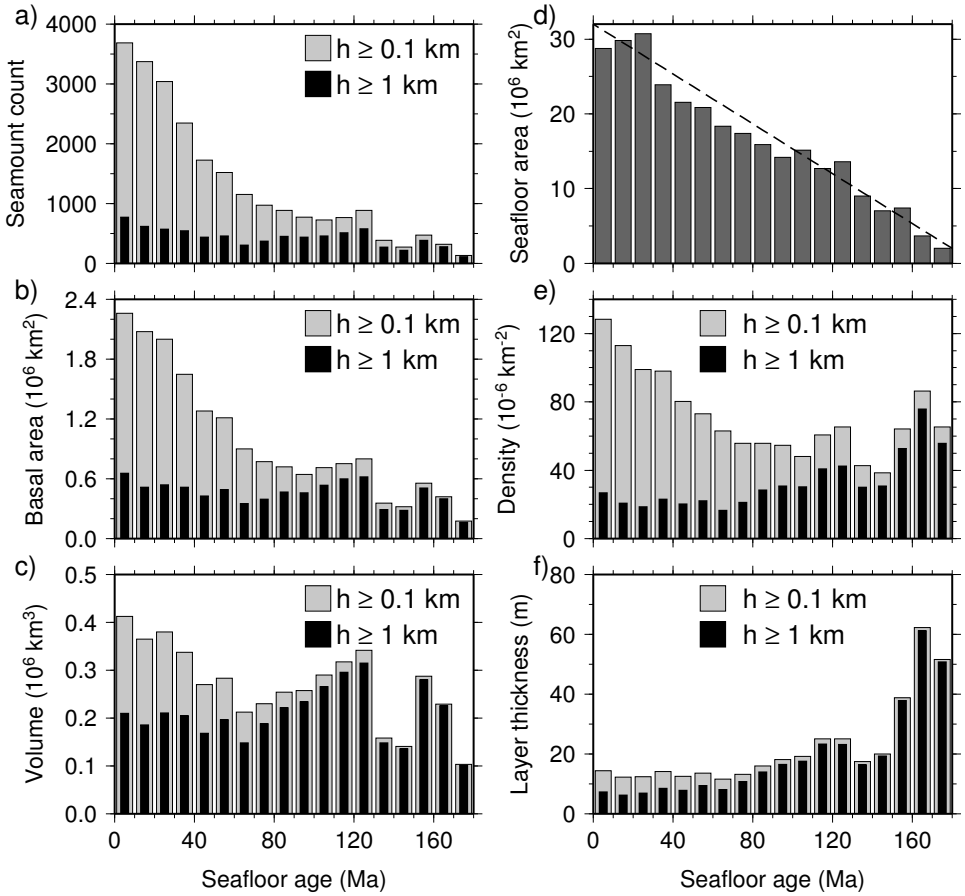

Figure 4.2: Histograms of seamounts, basal area, volume, seafloor area, seamount density, and layer thickness as a function of seafloor age. a) Number of seamounts as a function of seafloor age. Narrow columns (black) represent seamounts of $h > 1$ km while wide columns (gray) represent small ($h < 1$ km) seamounts. b) Total basal area of seamounts as a function of seafloor age. c) Total volume of seamounts as a function of seafloor age. An elliptical cone with a truncation ratio of 0.31 is assumed to compute the volume of a seamount. d) Seafloor area as a function of seafloor age. The total area of seafloor for each age bin is calculated globally and decreases linearly for older plates (dashed line). e) Seamount density as a function of seafloor age. The ratio of seamount counts (a) to seafloor area for each age bin yields seamount density. f) Equivalent layer thickness as a function of seafloor age. The ratio of seamount volume (e) to seafloor area (d) is the thickness of layer equivalent to that of oceanic crust layer.

density of the small seamounts ($h < 1$ km) decreases with plate age, whereas that of the large seamounts ($h > 1$ km) remains relatively steady and in fact increases from ∼70 Myr and beyond. This increase appears to be associated with both hotspot and non-hotspot volcanism. Although the highest density for 170 Ma crust is mostly an artificial signal caused by the very small seafloor area for that old age in the denominator, the higher density of large seamounts identified on crust of Cretaceous age, notably 130–110 and 160–150 Ma, is quite intriguing.

I also report the equivalent layer thickness (Figure 4.2e) determined from the ratio between the total seamount volume and the seafloor area, for each age bin. This layer thickness allows a comparison of the volumetric production from seamount volcanism to that of the volcanic crust produced by seafloor spreading. Even if I just consider oceanic layer 2 (typically ∼2 km thick) I see that seamount volcanism, on average, only amounts to only 1–3% of that volume. Furthermore, the total basal area of all the potential seamounts is just 6% of the total area of the dated seafloor.

From all of these histograms, I can draw the conclusion that the oceanic crust formed in the Cretaceous, especially the Early Cretaceous (130–110 Ma), has experienced a higher degree of seamount production than ocean crust of other ages. This global pulse is also observed by the previous seamount studies [Wessel, 2001; Hillier, 2007]. Wessel [2001] reported a similar trend but also found multiple local peaks at ∼40, ∼80, ∼120, and ∼160 Ma, which he suspected to be an intriguing but unlikely correlation with Pacific tectonic history. Hillier [2007] found two main peaks centered on 120–110 and 160–150 Ma Pacific crust and suggested that seamount production has been persistent on the same lithosphere. However, Hillier [2007] used 2,706 seamounts of $h > 1.5$ km (i.e., ∼2% of his actual seamount count for the Pacific plate) that matched the location of any of the Pacific seamounts found by Wessel & Lyons [1997], which formed the basis of the the Pacific results reported by Wessel [2001]. My first-order reconciliation of these disparate seamount databases in Chapter

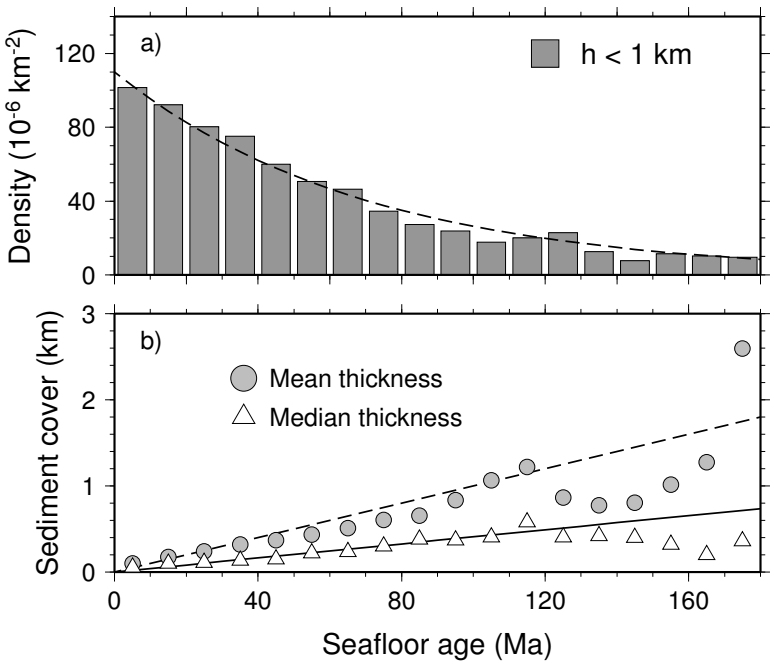

Figure 4.3: Variations of small seamount count and sediment thickness as a function of seafloor age. a) Number of small seamounts ($h < 1$ km) as a function of seafloor age. Dashed line shows the exponential decay of seamount counts for older plates (i.e., greater depth). b) Sediment thickness as a function of seafloor age. The average (circles and dashed line) and median (triangles and solid line) sediment thickness per each age bin are computed using the NGDC global sediment database [Divins, 2005].

3 demonstrated that both seamount databases have excessive counts from volcanic ridges. Therefore, the multiple peaks of Wessel [2001] reported from 40 and 80 Ma crust may indicate the volumetric contribution caused by included volcanic ridges. The lithospheric control on seamount location proposed by Hillier [2007] also requires a reassessment in terms of my new global seamount database (Chapter 3) and the dense core flexure model (Chapter 2) as he obtained apparent seamount ages inferred from the lithospheric strength underneath the seamounts.

The number of small seamounts ($h < 1$ km) identified in my study exponentially decreases for older crust (dashed line in Figure 4.3a). The approximately exponential decline in the number of small seamounts with increasing crustal age indicates that their gravity signals are significantly attenuated due to the greater depths of older crust [Parsons & Sclater, 1977]. As discussed in Chapter 3, the upward continuation

effect is an exponential decay term that depends on both depth and feature length scale, so even if small seamounts were being produced uniformly in time I would still expect to see an exponential decline with increasing age (i.e., depth). In Figure 4.3b, the sediment thickness appears to be linearly increasing for older seafloor. The difference between the linear trends of the average and median sediment thickness implies that the sediments are unevenly distributed over the seafloor. For example, the sediment thickness of the 180 Ma seafloor on the North America plate is more than 20 times thicker than that of the 180 Ma seafloor on the Pacific plate. Nonetheless, increasing age provides more opportunity for small seamounts to become buried completely by sediments [Wessel et al., 2010], a fate which significantly reduces the density contrast and hence the observed gravity anomalies.

Second, I examine how the seamount distribution is related with the half-spreading rate of the seafloor on which the potential seamounts are found (Figure 4.4). For this comparison, similar histograms to those I discussed above are constructed, this time as a function of spreading rate (Figure 4.5). About 64% of the identified seamounts are found on the seafloor formed with spreading rate less than 40 mm yr^{-1} that consists about 60% of the modeled seafloor (Figure 4.5d). The density of small seamounts ($h < 1$ km) are about three times more than that of the large seamounts for the same range of spreading rate (Figure 4.5e). Figure 4.4 indicates that seamounts in this range (< 40 mm yr^{-1}) are mainly from the Atlantic and Indian Oceans where spreading rates have been lower and more steady over time. In contrast, the seamounts found on the Pacific Ocean are spread over the entire range of spreading rates. For example, the small peak centered on 115 mm yr^{-1} in Figure (4.5c) is due to the Easter Seamount Chain. This focused distribution of small seamounts on the Atlantic and Indian Oceans implies that relatively scare melt supply and prevalent amagmatic extensional process at slow spreading system limit seamount production and growth.

Müller et al. [1998] proposed that asymmetric crustal accretion at mid-ocean ridges

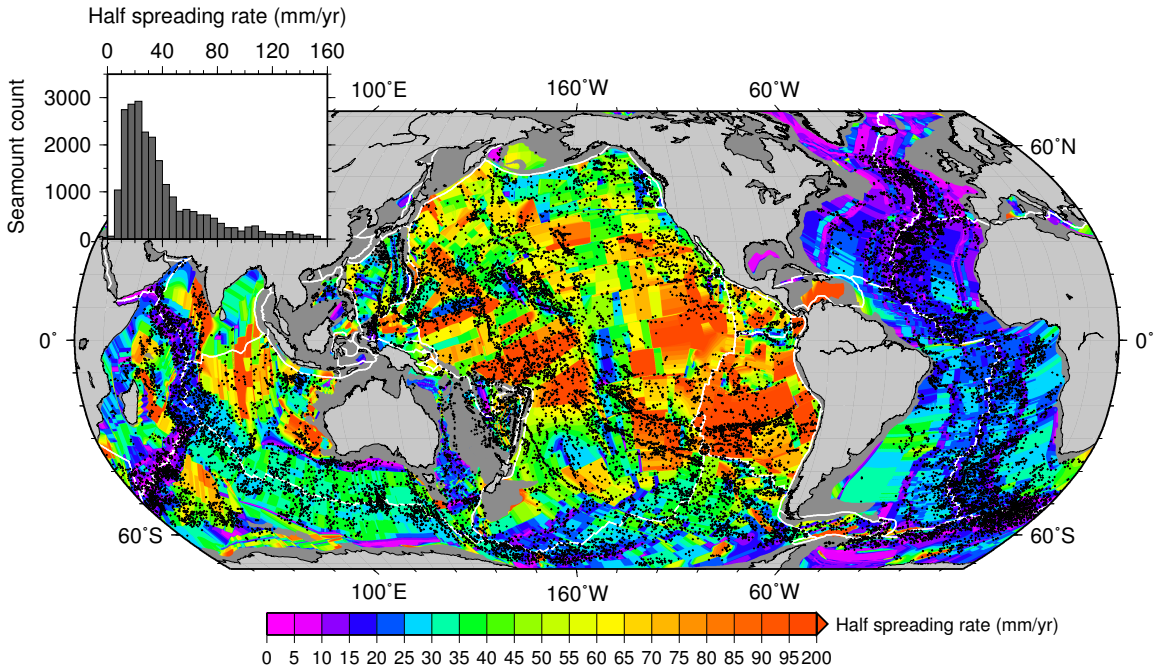

Figure 4.4: Potential seamounts (crosses) and half spreading rates. White lines are plate boundaries from Bird [2003]. The inset is a histogram of seamount counts as a function of half-spreading rate. The rate grid version 3.2 is used [Müller et al., 2008].

is caused by ridge migration toward mantle plumes or minor ridge jumps enforced by asthenospheric flow between mantle plumes and nearby ridges. In their study, the leading ridge flanks show excessive crustal accretion compared to the conjugate trailing flanks. According to Müller et al. [1998], the leading plates moves faster relative to the mantle than their conjugates. The conjugate trailing plates move relatively slower than the leading plates because they are underlain by one or several hotspots. In this respect, I assume a simple relationship between the spreading rate and the crustal accretion that the crust formed by fast spreading is more thicker than that by slow spreading. The wide distribution of small seamounts on crust formed by fast spreading (see the dashed line in Figure 4.5e), thus, may indicate that seamount production can be impeded by relatively thick ocean crust resulting from excessive accretion. If a given melt supply can feed a small seamount on the crust formed by slow spreading, the same supply system may not be able to produce a seamount on the crust formed by fast spreading because the crust is too thick for the given

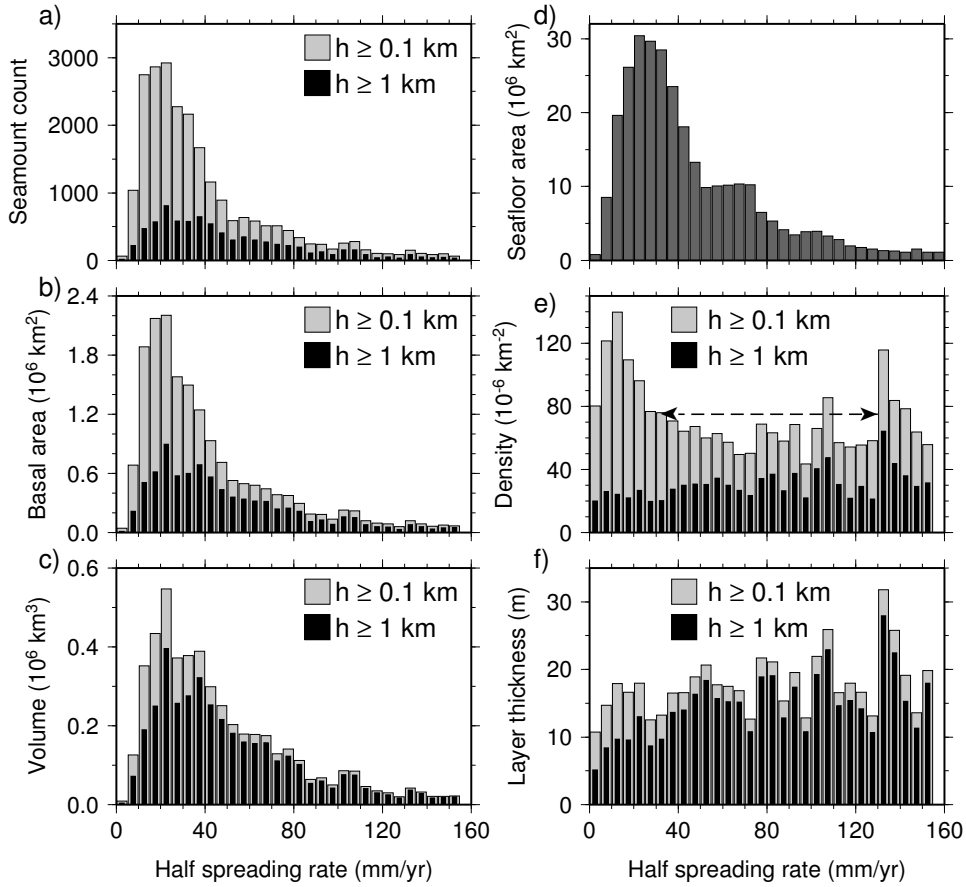

Figure 4.5: Histograms of seamounts, basal area, volume, seafloor area, seamount density, and layer thickness as a function of spreading rate. a) Number of seamounts as a function of spreading rate. b) Total basal area of seamounts as a function of spreading rate. c) Total volume of seamounts as a function of spreading rate. d) Seafloor area as a function of spreading rate. e) Seamount density as a function of spreading rate. f) Equivalent layer thickness as a function of seafloor age.

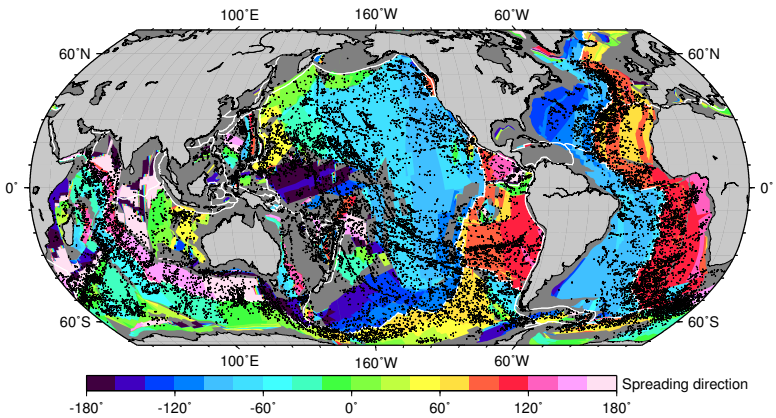

Figure 4.6: Potential seamounts (crosses) and spreading direction. White lines are plate boundaries from Bird [2003]. Spreading directions are one of the parameters that the reconstruction model of Müller et al. [2008] predicts. I used their linear interpolation method for data gaps between adjacent seafloor isochrons. However, the grid nodes where no adjacent isochrons are found were not interpolated to avoid artifacts from global gridding schemes. Northward spreading is indicated by 0°, eastward by 90°, westward by -90°, and southward by ±180°.

melt system to penetrate. Like the East Pacific Rise, the fast spreading system has relatively abundant melt supply than the slow spreading system so that this melt supply may be able to feed a seamount. However, its growth can be limited because the fast-moving plate carries away the seamount from its near-ridge feeding system. Thus, the small seamounts are more densely populated on the crust formed by slow spreading. For the large seamounts, additional melting given by upwelling plumes and non-hotspot processes is sufficient to produce and grow them on any crust. To strengthen this implication, however, I would need to limit my analysis to available conjugate plate segments. In addition, the seafloor area formed during periods when spreading rates exceeded 80 mm yr^{-1} is significantly smaller than other parts of the ocean crust, which leads to increase artificially the density of seamounts and layer thickness. The half spreading rates faster than 100 mm yr^{-1} can also be due to artifacts from the modeling and gridding processes of Müller et al. [1998] because the rate seems geologically unreasonable.

Lastly, I generate a grid of spreading direction using the model outputs from

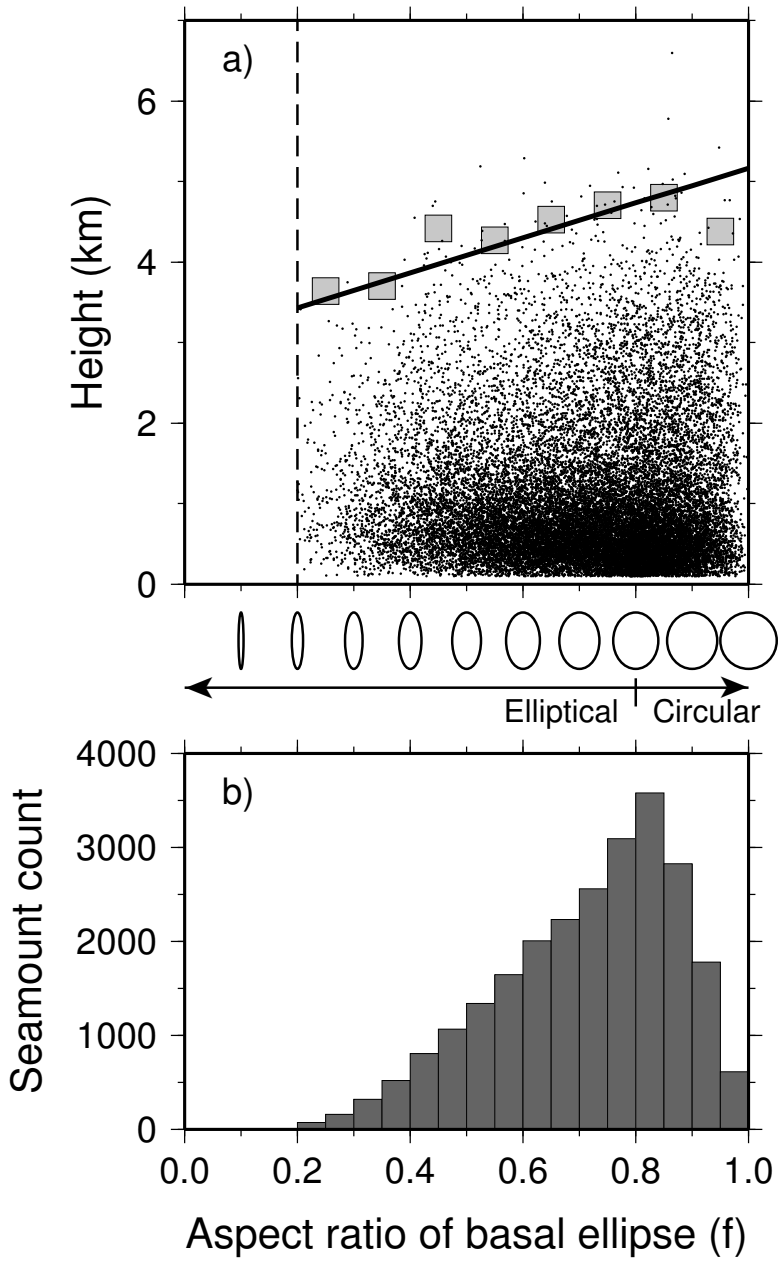

Figure 4.7: Distinction between circular and elliptical seamounts. a) Scatter plot of seamount height and aspect ratio of basal ellipse. Aspect ratio limit imposed by modeling in Chapter 3 is indicated as dashed line. A linear relationship between the aspect ratio and height (solid line) may indicate that circular seamounts grow taller than elliptical seamounts. The squares indicate 99% quartile height of the seamounts ($h > 2$ km) for each age bin. b) Histogram of seamounts as a function of aspect ratio. The aspect ratio larger than 0.8 can be regarded as circular seamounts (see text for detail).

the global plate reconstruction model of Müller et al. [2008] in order to examine if seamount orientation is related to or determined by existing seafloor fabric, presumably sub-parallel or perpendicular to spreading direction at the time of crust formation. My derived spreading direction grid, however, shows more data gaps than the published grids of age and spreading rate (Figures 4.1, 4.4, and 4.6) because I did not apply a global gridding scheme (e.g., continuous curvature spline in tension) to avoid unnecessary smoothing between adjacent spreading directions. As expected, east-west spreading is predominant along the East Pacific Rise and Mid-Atlantic Ridge, whereas north-south spreading dominates along the Southeast Indian Ridge (Figure 4.6).

Before comparing azimuth of the major axis of each basal seamount ellipse with the calculated spreading directions, it is first necessary to define a quantitative measure for the separation of circular and elliptical seamounts. The distribution of aspect ratios (i.e., $f = b/a$) between the minor (b) and major (a) axes is asymmetrical and centered on $f = 0.8$ (Figure 4.7b). However, the rapid decrease toward perfect circularity (i.e., $f = 1$) does not indicate that seamounts are unlikely to be circular. Recall that in the process of seamount characterization (Chapter 3), I first used the circular polynomial model to approximate the observed vertical gravity gradient (VGG) data and purposefully changed the model for VGG seamounts to the elliptical polynomial model. Although the circular model could be qualitatively adequate for some seamounts, the elliptical model was statistically preferred because of the presence of data noise. If the circular seamounts are closely spaced, the separation between the seamounts becomes less distinct in VGG signals. In this case, the elliptical model will be more preferred statistically over the circular model. Thus, based on a qualitative assessment I define circular seamounts to be the ones with $f > 0.8$ (Figure 4.7).

In addition, Figure 4.7a implies that circular seamounts can grow taller than elliptical seamounts. If the total volcanic output (i.e., volume) of a given magma

supply stays the same either for a circular or elliptical seamount and the radius of the circular seamount is equal to the minor axis of the elliptical seamount, the height of the elliptical seamount (h_e) will be less than that of the circular seamount (h_c) by a factor of the given aspect ratio (i.e., $h_e = fh_c$). The linear relationship observed in Figure 4.7a may reflect such a simple volumetric difference between the circular and elliptical seamounts.

Using this aspect threshold, I obtain spreading directions at 4,277 elliptical seamounts; this number is limited relative to actual counts mainly due to the data gaps in the spreading direction grid. While the spreading direction is given in the full circle (i.e., -180° to 180°), the azimuth comparison just needs the orientation (i.e., -90° to 90°). Thus, I examine absolute angular differences between the seafloor and seamount orientations and choose the smallest value as the angular difference for a given elliptical seamount. Somewhat surprisingly, this comparison indicates that there is no significant relationship between spreading direction and seamount orientation (Figure 4.8). Because the orientations of the seafloor fabric are the surface manifestation of the spreading direction at the formation of the ocean crust, this result further indicates that the pre-existing seafloor fabric by itself is less likely to dictate the orientation of seamounts, whether small or large (Figure 4.8a), during the formation of seamounts. In addition, it may imply that the orientation of individual seamount is mostly prescribed by the magma feeding system and continuous or sporadic development of intrusive and extrusive dikes. Another factor that might influence the orientation of such features is the state of stress in the oceanic lithosphere. Thus, it may be of considerable interest to examine the orientation of seamount chains and volcanic ridges [e.g., Lynch, 1999; White et al., 2006] with respect to temporal changes in plate motions and spreading directions, assuming these may be considered proxies for stress directions.

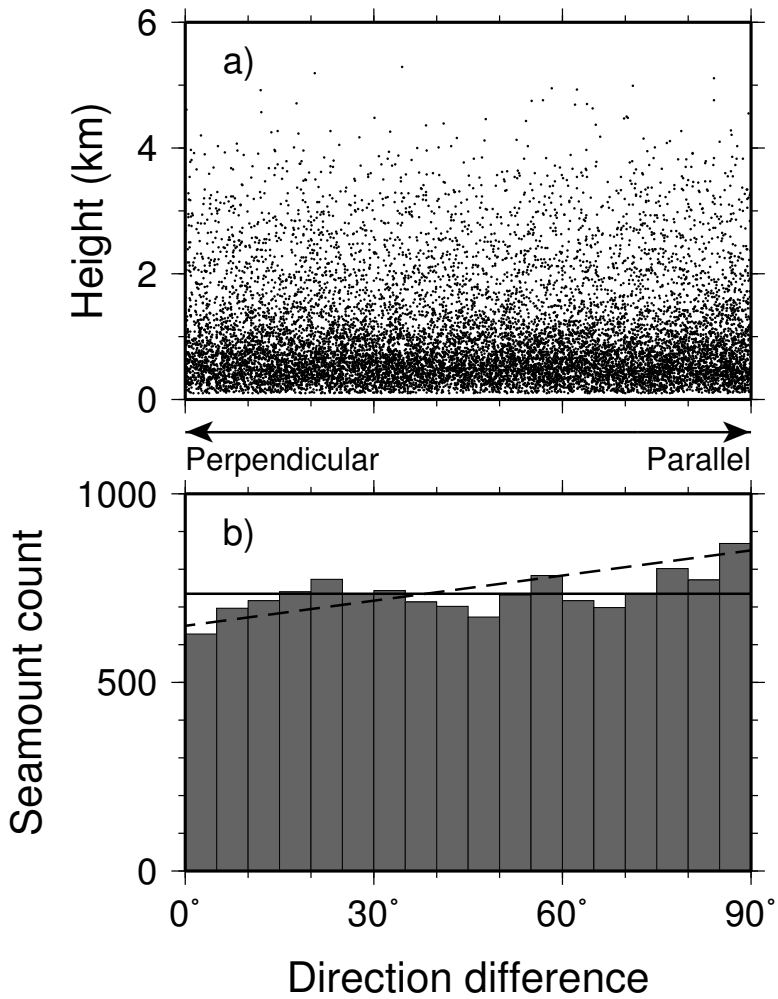

Figure 4.8: Comparison between azimuth of basal ellipse and spreading direction. a) Scatter plot of seamount heights and angular difference between seamount orientation and spreading orientation. Only seamounts having basal ellipses with aspect ratio < 0.8 (Figure 4.8) are considered for this comparison. The angular difference is the smallest difference between seamount and seafloor spreading orientations. b) Histogram of seamounts as a function of direction difference. The mean trend is represented by solid line. Although no significant relationship between spreading direction and azimuth is apparent, the difference seems to increase linearly (dashed line).

4.3 Conclusions

I have compared the population and volume derived from my global seamount database with the several aspects of the world's ocean crust, such as crustal age, half-spreading rate at the time of crust formation, and seafloor fabric, in order to investigate the first-order temporal variations in underwater volcanism. From the volume distribution as a function of crustal age, I have concluded that intraplate volcanism is volumetrically a significant contributor to the volcanic accretion of young crust (< 40 Myr) apart from the seafloor-spreading process itself, based on the observed difference between the total volumes from small ($h < 1$ km) and large ($h > 1$ km) seamounts. The density of seamount coverage per each age bin suggests that the ocean crust formed in the Cretaceous, especially the Early Cretaceous (130–110 Ma), has experienced a higher degree of seamount production than ocean crust of other ages. Comparison between the half-spreading rate of the seafloor and the new seamount database have determined that about 64% of the identified seamounts are located on seafloor formed during periods with spreading rates less than 40 mm yr^{-1}. Lastly, the absolute angular differences between the seafloor fabric and seamount orientations have indicated that there is no significant relationship between spreading direction and the seamount orientations. Thus, it may instead be of considerable interest to examine the orientation of seamounts and volcanic ridges with any temporal changes in plate motions and spreading directions, making the assumption that such changes influence the magnitude and direction of stresses in the oceanic lithosphere.

Chapter 5

Summary and Future Research Directions

In this dissertation, I have examined the following geophysical and statistical aspects of seamounts and their implications for underwater volcanism:

1. Using various synthetic and real examples, I have demonstrated that the uniform seamount density model underestimates T_e (i.e., elastic thickness of the lithosphere) and hence overestimates the flexural deformation caused by the loading of a seamount. When gravity data are the only available data to constrain flexure modeling, the biases in flexural deformation can go unnoticed because the predicted gravity with an underestimated T_e (and hence overestimated deflections) can nevertheless be the best fit to the observed gravity data. This well-known non-uniqueness of solutions to the gravity field can be circumvented by using additional observations (e.g., seismic profiles) or mitigated by a more rigorous analysis. In this study, I have shown that the inclusion of a dense core is important when approximating the first-order inhomogeneous internal seamount structure. This approximation has been tested with a new analytic solution for the flexural deformation due to axisymmetric dense core loads (i.e., disc and parabolic forms). Next, I approximated the analytic dense core model by converting it into a uniform density model with same mass as the dense core load, which allowed me to compute flexural deflections and gravity anomalies over a seamount in the wavenumber domain. As a real example, I have applied the dense core model approximation in predicting the lithospheric flexure

beneath Howland Island in the Tokelau seamount chain and compared it with the predictions of the uniform density model. Based on published ages of Howland and the age of the underlying seafloor, traditional relationships between T_e and plate age predicts the elastic plate thickness beneath the seamount to be 20–23 km, which is comparable to the best dense core model of $T_e = 26$ km. However, the best uniform density model is found at $T_e = 12$ km, which is significantly less than the predicted since flexural rigidity is proportional to T_e cubed. Therefore, I conclude that the dense core model approximates the true mass distribution of a seamount better than the uniform density model.

2. In order to detect and characterize seamounts in the altimetry-derived vertical gravity gradient (VGG) data, I have formulated a non-linear inversion that minimizes the misfit between an elliptical polynomial seamount model and observed VGG data at potential seamounts. The inversion calculations are entirely automated and guided by two model selection criteria (i.e., Akaike Information Criteria and F-tests) used to examine the statistical significance of potential seamounts. Following a global search for seamounts using this inversion approach and automatic and manual inspections of the model parameters determined by the inversion, I have obtained bathymetric morphology parameters (i.e., height h, geographical location, major and minor axes of basal ellipse, and azimuth of the major axis) for 24,643 potential seamounts of $h > 0.1$ km. Although this number is significantly lower than many previous predictions, a first-order reconciliation of my results with the size-frequency statistics obtained from those studies reveals that the previous counts are systematically over-estimated due to multiple peaks at volcanic ridges and misidentification of abyssal hills as seamounts. With taking account of the ambiguity of gravity signals due to small seamounts of $h < 1$ km and the overlap in scale with abyssal hills, I have tentatively estimated a new global seamount census ($h > 0.1$ km)

to lie in the 30,000–63,000 range.

3. I have compared the population and volume derived from my global seamount database with the several aspects of the world's ocean crust, such as crustal age, half-spreading rate at the time of crust formation, and seafloor fabric, in order to investigate the first-order temporal variations in underwater volcanism. From the volume distribution as a function of crustal age, I have concluded that intraplate volcanism is volumetrically a significant contributor to the volcanic accretion of young crust (< 40 Myr) apart from the seafloor-spreading process itself, based on the observed difference between the total volumes from small ($h < 1$ km) and large ($h > 1$ km) seamounts. The density of seamount coverage per each age bin suggests that the ocean crust formed in the Cretaceous, especially the Early Cretaceous (130–110 Ma), has experienced a higher degree of seamount production than ocean crust of other ages. Comparison between the half-spreading rate of the seafloor and the new seamount database have determined that about 64% of the identified seamounts are located on seafloor formed during periods with spreading rates less than 40 mm yr^{-1}. Lastly, I have examined if elongated seamount orientations are related to or determined by existing seafloor fabric. The absolute angular differences between the seafloor fabric and seamount orientations have indicated that there is no significant relationship between spreading direction and the seamount orientations. Thus, it may instead be of considerable interest to examine the orientation of seamounts and volcanic ridges with any temporal changes in plate motions and spreading directions, making the assumption that such changes influence the magnitude and direction of stresses in the oceanic lithosphere.

In order to obtain a comprehensive understanding of underwater volcanism, it may be necessary to estimate volume contributions from volcanic ridges and seamounts separately because the former can mask or bias the volume flux associated with

seamounts. In this respect, the new global seamount database can serve as a starting point to differentiate between these two volcanic processes, as the data processing used to detect seamounts could be extended to characterize volcanic ridges. Given the limited number of radiometrically dated seamounts (< 300), lithospheric strength estimates at seamounts can be crucial for investigating the true temporal variation of seamount volcanism. The global pulses observed in the seamount density distribution only indicate that the ocean crust formed in the Cretaceous has been subject to intense seamount volcanism. Because the seamounts must have formed later than the oceanic crust beneath them, the apparent ages of seamounts derived from lithospheric strength at the time of seamount formation can be useful in understanding the duration of underwater volcanism. Systematic flexure modeling with the dense core model may become possible given the new seamount database. Finally, the seamount database with additional geophysical and geochemical databases may be used to differentiate between hotspot and non-hotspot volcanism. Hotspot-originated seamounts serve as useful constraints when refining absolute plate motion models and hotspot locations, while the non-hotspot seamounts can be important for testing various hypotheses on intraplate volcanic processes (e.g., lithospheric cracks, small-scale convection, and asthenospheric flow). Such future research developments may build on the foundation laid down by the research described in this dissertation.

Bibliography

Abers, G. A., Parsons, B., & Weissel, J. K., 1988. Seamount abundance and distributions in the southeast Pacific, *Earth Planet. Sci. Lett.*, **87**, 137–151.

Abramowitz, M. & Stegun, I. A., 1970. *Handbook of Mathematical Functions*, Dover Publications, Inc., New York, 9th edn.

Adam, C. & Bonneville, A., 2008. No thinning of the lithosphere beneath northern part of the Cook-Austral volcanic chains volcanic chains, *J. Geophys. Res.*, **113**, B10104, doi:10.1029/2007JB005313.

Al-Chalabi, M., 1971. Some studies relating to nonuniqueness in gravity and magnetic inverse problems, *Geophysics*, **36**(5), 835–855.

Ali, M. Y., Watts, A. B., & Hill, I., 2003. A seismic reflection profile study of lithospheric flexure in the vicinity of the Cape Verde Islands, *J. Geophys. Res.*, **108**(B5), 2239, doi:10.1029/2002JB002155.

Araña, V., Camacho, A. G., Garcia, A., Montesinos, F. G., Blanco, I., Vieira, R., & Felpeto, A., 2000. Internal structure of Tenerife (Canary Islands) based on gravity, aeromagnetic and volcanological data, *J. Volcanol. Geotherm. Res.*, **103**, 43–64.

Ballmer, M. D., van Hunen, J., Ito, G., Tackley, P. J., & Bianco, T. A., 2007. Non-hotspot volcano chains originating from small-scale sublithospheric convection, *Geophys. Res. Lett.*, **34**, L23310.

Baptista, E. C., Belati, E. A., & da Costa, G. R. M., 2005. Logarithmic barrier-augmented Lagrangian function to the optimal power flow problem, *Electrical Power Energy Syst*, **27**(7), 528–532.

Batiza, R., 1982. Abundances, distribution and sizes of volcanoes in the Pacific Ocean and implications for the origin of non-hotspot volcanoes, *Earth Planet. Sci. Lett.*, **60**, 195–206.

Batiza, R. & Vanko, D., 1983. Volcanic development of small oceanic central volcanoes on the flanks of the East Pacific Rise inferred from narrow-beam echo-sounder surveys, *Mar. Geol.*, **54**, 53–90.

BBC, 2005. Crew blamed for grounding US sub, http://news.bbc.co.uk/2/hi/americas/4527459.stm.

Becker, J. J., Sandwell, D. T., Smith, W. H. F., Braud, J., Binder, B., Depner, J., Fabre, D., Factor, J., Ingalls, S., Kim, S.-H., Ladner, R., Marks, K., Nelson, S., Pharaoh, A., Sharman, G., Trimmer, R., Rosenburg, J. V., Wallace, G., & Weatherall, P., 2009. Global bathymetry and elevation data at 30 arc seconds resolution: SRTM30_PLUS, *Marine Geodesy*, **32**(4), 355–371.

Behn, M. D., Sinton, J. M., & Detrick, R. S., 2004. Effect of the Galápagos hotspot on seafloor volcanism along the Galápagos Spreading Center (90.9-97.6° W), *Earth Planet. Sci. Lett.*, **217**, 331–347.

Bird, P., 2003. An updated digital model of plate boundaries, *Geochem. Geophys. Geosyst.*, **4**(3), 1027.

Blakely, R. J., 1996. *Potential Theory in Gravity and Magnetics Applications*, Cambridge Univ. Press, Cambridge, UK, 1st edn.

Bodine, J. H., 1980. Numerical computation of plate flexure in marine geophysics, Tech. Rep. CU-1-80, Columbia University.

Brotchie, J. F., 1971. Flexure of a liquid-filled spherical shell in a radial gravity field, *Modern Geology*, **3**, 15–23.

Brotchie, J. F. & Silvester, R., 1969. On crustal flexure, *J. Geophys. Res.*, **74**(22), 5240–5252.

Calmant, S., 1987. The elastic thickness of the lithosphere in the Pacific Ocean, *Earth Planet. Sci. Lett.*, **85**, 277–288.

Calmant, S. & Cazenave, A., 1986. The effective elastic lithosphere under the Cook-Austral and Society Islands, *Earth Planet. Sci. Lett.*, **77**, 187–202.

Calmant, S., Francheteau, J., & Cazenave, A., 1990. Elastic layer thickening with age of the oceanic lithosphere: a tool for prediction of the age of volcanoes or oceanic crust, *Geophys. J. Int.*, **100**(1), 59–67.

Camacho, A. G., Fernández, J., González, P. J., Rundle, J. B., Prieto, J. F., & Arjona, A., 2009. Structural results for La Palma Island using 3-D gravity inversion, *J. Geophys. Res.*, **114**, B05411, doi:10.1029/2008JB005628.

Chandler, M. T. & Wessel, P., 2008. Improving the quality of marine geophysical track line data: Along-track analysis, *J. Geophys. Res.*, **113**, B02102.

Clouard, V. & Bonneville, A., 2005. Ages of seamounts, islands, and plateaus on the Pacific plate, in *Plates, Plumes and Paradigms*, pp. 71–90, eds Foulger, G. R., Natland, J. H., Presnall, D. C., & Anderson, D. L., Geological Society of America Special Paper 388.

Collier, J. S. & Watts, A. B., 2001. Lithospheric response to volcanic loading by the Canary Islands: constraints from seismic reflection data in their flexural moat, *Geophys. J. Int.*, **147**, 660–676.

Contreras-Reyes, E., Grevemeyer, I., Watts, A. B., Planert, L., Flueh, E. R., & Peirce, C., 2010. Crustal intrusion beneath the Louisville hotspot track, *Earth. Planet. Sci. Lett.*, **289**, 323–333.

Courtillot, V., Davaille, A., Besse, J., & Stock, J., 2003. Three distinct types of hotspots in the Earth's mantle, *Earth Planet. Sci. Lett.*, **205**, 295–308.

Craig, C. H. & Sandwell, D. T., 1988. Global distribution of seamounts from Seasat profiles, *J. Geophys. Res*, **93**(B9), 10,408–10,420.

Crough, S. T., 1983. Hotspot swells, *Ann. Rev. Earth Planet. Sci*, **11**, 165–193.

Dalloubeix, C. & Fleitout, L., 1989. Convective thinning of the lithosphere: a model constrained by geoid observations, *Phys. Earth Planet. Int.*, **57**(3-4), 330–343.

Dettmer, J., 2006. *Geoacoustic reflectivity inversion: A Bayesian approach*, Ph. D., University of Victoria.

Divins, D., 2009. NGDC Total sediment thickness of the world's oceans and marginal seas, http://www.ngdc.noaa.gov/mgg/sedthick/sedthick.html.

Dixon, T. H., Naraghi, M., McNutt, M. K., & Smith, S. M., 1983. Bathymetric prediction from SEASAT altimeter data, *J. Geophys. Res.*, **88**, 1563–1571.

Dosso, S. E., Nielsen, P. L., & Wilmut, M. J., 2006. Data error covariance in matched-field geoacoustic inversion, *J. Acous. Soc. Am.*, **119**(1), 208–219.

Fleitout, L. & Yuen, D. A., 1984. Secondary convection and the growth of the oceanic lithosphere, *Phys. Earth Planet. Int.*, **36**, 181–212.

Fornari, D. J., Batiza, R., & Luckman, M. A., 1987. Seamount abundances and distribution near the East Pacific Rise 0°-24° N based on seabeam data, in *Seamounts, Islands, and Atolls*, vol. 43 of **Geophysical Monograph**, pp. 13–21, eds Keating, B. H., Freyer, P., Batiza, R., & Boehlert, G. W., AGU, Washington, D. C.

Fornari, D. J., Perfit, M. R., Allan, J. F., & Batiza, R., 1988. Small-scale heterogeneities in depleted mantle sources: near-ridge seamount lava geochemistry and implications for mid-ocean-ridge magmatic processes, *Nature*, **331**, 511–513.

Forsyth, D. W., Harmon, N., Scheirer, D. S., & Duncan, R. A., 2006. Distribution of recent volcanism and the morphology of seamounts and ridges in the GLIMPSE study area: Implications for the lithospheric cracking hypothesis for the origin of intraplate, nonhot spot volcanic chains, *J. Geophys. Res.*, **111**, B11407.

Friedrich, G. & Schmitz-Wiechowski, A., 1980. Mineralogy and chemistry of a ferromanganese crust from a deep-sea hill, Central Pacific, 'Valdivia' Cruise 13/2, *Mar. Geol.*, **37**, 71–90.

Gallart, J., Driad, L., Charvis, P., Sapin, M., Hirn, A., Diaz, J., de Voogd, B., & Sachpazi, M., 1999. Perturbation to the lithosphere along the hotspot track of La Reunion from an offshore-onshore seismic transect, *J. Geophys. Res.*, **104**(B2), 2895–2908.

Gille, S. T., Metzger, E. J., & Tokmakian, R., 2004. Seafloor topography and ocean circulation, *Oceanography*, **17**(1), 47–54.

Grevemeyer, I., Weigel, W., Schussler, S., & Avedik, F., 2001. Crustal and upper mantle seismic structure and lithospheric flexure along the Society Island hotspot chain, *Geophys. J. Int.*, **147**, 123–140.

Grigg, R. W., Malahoff, A., Chave, E. H., & Landahl, J., 1987. Seamount benthic ecology and potential environmental impact from manganese crust mining in Hawaii, in *Seamounts, Islands, and Atolls*, vol. 43, pp. 379–390, eds Keating, B. H., Freyer, P., Batiza, R., & Boehlert, G. W., AGU, Washington, D. C.

Hammer, P. T. C., Hildebrand, J. A., & Parker, R. L., 1991. Gravity inversion using seminorm minimization: density modeling of Jasper seamount, *Geophysics*, **56**(1), 68–79.

Haxby, W. F. & Weissel, J. K., 1986. Evidence for small-scale mantle convection from Seasat altimeter data, *J. Geophys. Res.*, **91**(B3), 3507–3520.

Haxby, W. F., Karner, G. D., LaBrecque, J. L., & Weissel, J. K., 1983. Digital images of combined oceanic and continental data sets and their use in tectonic studies, *Eos Trans. AGU*, **64**(52), 995–1004.

Heiskanen, W. A. & Moritz, H., 1967. *Phyiscal Geodesy*, W. H. Freeman Co., San Francisco, CA.

Hildebrand, J. A., Dorman, L. M., Hammer, P. T. C., Schreiner, A. E., & Cornuelle, B. D., 1989a. Seismic tomography of Jasper seamount, *Geophys. Res. Lett.*, **16**(12), 1355–1358.

Hildebrand, J. A., Dorman, L. M., Hammer, P. T. C., Schreiner, A. E., & Cornuelle, B. D., 1989b. Seismic tomography of Jasper seamount, *Geophys. Res. Lett.*, **16**(12), 1355–1358.

Hillier, J. K., 2007. Pacific seamount volcanism in space and time, *Geophys. J. Int.*, **168**(2), 877–889, doi:10.1111/j.1365–246X.2006.03250.x.

Hillier, J. K. & Watts, A. B., 2007. Global distribution of seamounts from ship-track bathymetry data, *Geophys. Res. Lett.*, **34**, L13304.

Ishihara, T., 1987. Gravimetric determination of densities of seamounts along the Bonin Arc, in *Seamounts, Islands, and Atolls*, vol. 43, pp. 97–113, eds Keating, B. H., Freyer, P., Batiza, R., & Boehlert, G. W., AGU, Washington, D. C.

Ito, G., McNutt, M., & Gibson, R. L., 1995. Crustal structure of the Tuamotu Plateau, 15°s, and implications for its origin, *J. Geophys. Res.*, **100**(B5), 8097–8114.

Jarrard, R. D. & Clague, D. A., 1977. Implications of pacific islands and seamount ages for the origins of volcanic chains, *Rev. Geophys.*, **15**(57-76).

Jordan, T. H., Menard, H. W., & Smith, D. K., 1983. Density and size distribution of seamounts in the eastern Pacific inferred from wide-beam sounding data, *J. Geophys. Res.*, **88**(B12), 10,508–10,518.

Kellogg, J. N., Wedgeworth, B. S., & Freymueller, J., 1987. Isostatic compensation and conduit structures of western Pacific seamounts: Results of three-dimensional gravity modeling, in *Seamounts, Islands, and Atolls*, vol. 43 of **Geophys. Monogr. Ser.**, pp. 85–96, eds Keating, B. H., Freyer, P., Batiza, R., & Boehlert, G. W., AGU, Washington, D. C.

Kim, S.-S. & Wessel, P., 2008. Directional median filtering for regional-residual separation of bathymetry, *Geochem. Geophys. Geosyst.*, **9**, Q03005, doi:10.1029/2007GC001850.

Kim, S.-S. & Wessel, P., 2010. Flexure modelling at seamounts with dense cores, *Geophys. J. Int.*, **182**, 583–598.

Kitchingman, A. & Lai, S., 2004. Inferences of potential seamount locations from mid-resolution bathymetric data, in *Seamounts: Biodiversity and Fisheries*, vol. 12(5), pp. 7–12, eds Morato, T. & Pauly, D., Fisheries Centre Research Reports.

Kopp, H., Flueh, E. R., Papenberg, C., & Klaeschen, D., 2004. Seismic investigations of the O'Higgins Seamount Group and Juan Fernández Ridge: Aseismic ridge emplacement and lithosphere hydration, *Tectonics*, **23**, TC2009, doi:10.1029/2003TC001590.

Koppers, A. A. P. & Staudigel, H., 2005. Asynchronous bends in Pacific seamount trails: A case for extensional volcanism?, *Science*, **307**, 904–907.

Koppers, A. A. P. & Watts, A. B., 2010. Intraplate seamounts as a window into deep Earth processes, *Oceanography*, **23**(1), 42–57.

Koppers, A. A. P., Staudigel, H., Morgan, J. P., & Duncan, R. A., 2007. Nonlinear $^{40}Ar/^{39}Ar$ age systematics along the Gilbert Ridge and Tokelau Seamount Trail and the timing of the Hawaii-Emperor Bend, *Geochem. Geophys. Geosyst.*, **8**, Q06L13, doi:10.1029/2006GC001489.

Kruse, S. E., Liu, Z. J., Naar, D. F., & Duncan, R. A., 1997. Effective elastic thickness of the lithosphere along the Easter Seamount Chain, *J. Geophys. Res.*, **102**(B12), 27,305–27,317.

Lambeck, K., 1981a. Flexure of the oceanic lithosphere from island uplift, bathymetry, and geoid height observations: the Society Islands, *Geophys. J. R. Astron. Soc.*, **67**, 91–114.

Lambeck, K., 1981b. Lithospheric response to volcanic loading in the southern Cook Islands, *Earth Planet. Sci. Lett.*, **55**, 482–496.

Lambeck, K. & Nakiboglu, S. M., 1980. Seamount loading and stress in the ocean lithosphere, *J. Geophys. Res.*, **85**(B11), 6403–6418.

Li, Y. & Oldenburg, D. W., 1996. 3-D inversion of magnetic data, *Geophysics*, **61**(2), 394–408.

Lynch, M. A., 1999. Linear ridge groups: Evidence for tensional cracking in the pacific plate, *J. Geophys. Res.*, **104**(B12), 29,321–29,333.

Lyons, S. N., Sandwell, D. T., & Smith, W. H. F., 2000. Three-dimensional estimation of elastic thickness under the Louisville Ridge, *J. Geophys. Res.*, **105**(B6), 13,239–13,252.

Mammerickx, J., 1992. The Foundation seamounts: tectonic setting of a newly discovered seamount chain in the south Pacific, *Earth Planet. Sci. Lett.*, **113**, 293–306.

Marks, K. M., 1996. Resolution of the Scripps/NOAA marine gravity field from satellite altimetry, *Geophys. Res. Lett.*, **23**(16), 2069–2072.

Marks, K. M. & Smith, W. H. F., 2007. Some remarks on resolving seamounts in satellite gravity, *Geophys. Res. Lett.*, **34**, L03307, doi:10.1029/2006GL028857.

Maus, S., Green, C. M., & Fairhead, J. D., 1998. Improved ocean-geoid resolution from retracked ERS-1 satellite altimeter waveforms, *Geophys. J. Int.*, **134**, 243–253.

McNutt, M. K., 1984. Lithospheric flexure and thermal anomalies, *J. Geophys. Res.*, **89**(B13), 11,180–11,194.

McNutt, M. K. & Menard, H. W., 1978. Lithospheric flexure and uplifted atolls, *J. Geophys. Res.*, **83**(B3), 1206–1212.

Menard, H. W., 1964. *Marine Geology of the Pacific*, McGraw-Hill, New York.

Menke, W., 1981. The effect of load shape on the deflection of thin elastic plates, *Geophys. J. R. Astron. Soc.*, **65**, 571–577.

Minshull, T. A. & Charvis, P., 2001. Ocean island densities and models of lithospheric flexure, *Geophys. J. Int.*, **145**, 731–739.

Mitchell, N. C., 2001. Transition from circular to stellate forms of submarine volcanoes, *J. Geophys. Res.*, **106**(B2), 1987–2003.

Mofjeld, H. O., Symons, C. M., Lonsdale, P., González, F. I., & Titov, V. V., 2004. Tsunami scattering and earthquake faults in the deep Pacific ocean, *Oceanography*, **17**(1), 38–46.

Montgomery, D. C. & Peck, E. A., 1992. *Introduction to Linear Regression Analysis*, Wiley, New York.

Müller, R. D., Roest, W. R., & Royer, J.-Y., 1998. Asymmetric sea-floor spreading caused by ridge-plume interactions, *Nature*, **396**, 455–459.

Müller, R. D., Sdrolias, M., Gaina, C., & Roest, W. R., 2008. Age, spreading rates, and spreading asymmetry of the world's ocean crust, *Geochem. Geophys. Geosyst.*, **9**(4), Q04006, doi:10.1029/2007GC001743.

Nagy, D., 1966. The gravitational attraction of a right rectangular prism, *Geophysics*, **31**, 361–371.

NGDC, 2006. 2-minute Gridded Global Relief Data (ETOPO2v2), http://www.ngdc.noaa.gov/mgg/fliers/06mgg01.html.

Parker, R. L., 1972. The rapid calculation of potential anomalies, *Geophys. J. R. Astron. Soc.*, **31**, 447–455.

Parsons, B. & Sclater, J. G., 1977. An analysis of the variation of ocean floor bathymetry and heat flow with age, *J. Geophys. Res.*, **82**, 803–827.

Plouff, D., 1976. Gravity and magnetic fields of polygonal prisms and application to magnetic terrain corrections, *Geophysics*, **41**, 727–741.

Press, W. H., Teukolsky, S. A., Vetterling, W. T., & Flannery, B. P., 1992. *Numerical recipes in C: the art of scientific computing*, Cambridge Univ. Press, London, 2nd edn.

Ramillien, G. & Mazzega, P., 1999. Non-linear altimetric geoid inversion for lithospheric elastic thickness and crustal density, *Geophys. J. Int.*, **138**(3), 667–678.

Rappaport, Y., Naar, D. F., Barton, C. C., Liu, Z. J., & Hey, R. N., 1997. Morphology and distribution of seamounts surrounding Easter Island, *J. Geophys. Res.*, **102**(B11), 24,713–24,728.

Robertson, E. I., 1967. Gravity survey in the Cook Islands, *N. Z. J. Geol. Geophys.*, **10**, 1484–1498.

Sandwell, D. T. & Smith, W. H. F., 1997. Marine gravity anomaly from Geosat and ERS-1 satellite altimetry, *J. Geophys. Res.*, **102**(B5), 10,039–10,054.

Sandwell, D. T. & Smith, W. H. F., 2005. Retracking ERS-1 altimeter waveforms for optimal gravity field recovery, *Geophys. J. Int.*, **163**, 79–89.

Sandwell, D. T. & Smith, W. H. F., 2009. Global marine gravity from retracked Geosat and ERS-1 altimetry: Ridge segmentation versus spreading rate, *J. Geophys. Res.*, **114**, B01411, doi:10.1029/2008JB006008.

Sandwell, D. T. & Wessel, P., 2010. Box 3: Seamount discovery tool aids navigation to uncharted seafloor features, *Oceanography*, **23**(1), 34–36.

Small, C. & Sandwell, D. T., 1994. Imaging mid-ocean ridge transitions with satellite gravity, *Geology*, **22**, 123–126.

Smith, D. K. & Cann, J. R., 1990. Hundreds of small volcanoes on the median valley floor of the Mid-Atlantic Ridge at 24-30° N, *Nature*, **348**, 152–155.

Smith, W. H. F., 1990. *Marine geophysical studies of seamounts in the Pacific Ocean basin*, Ph. D., Columbia Univ.

Smith, W. H. F. & Sandwell, D. T., 1994. Bathymetric prediction from dense satellite altimetry and sparse shipboard bathymetry, *J. Geophys. Res*, **99**(B11), 21,803–21,824.

Smith, W. H. F. & Sandwell, D. T., 1997. Global sea floor topography from satellite altimetry and ship depth soundings, *Science*, **277**(5334), 1956–1962.

Smith, W. H. F., Staudigel, H., Watts, A. B., & Pringle, M. S., 1989. The Magellan seamounts: Early Cretaceous record of the South Pacific isotopic and thermal anomaly, *J. Geophys. Res.*, **94**(B8), 10,501–10,523.

Smoot, N. C., 1982. Guyots of the Mid-Emperor Chain mapped with multibeam sonar, *Mar. Geol.*, **47**, 153–163.

Staudigel, H. & Schmincke, H.-U., 1984. The Pliocene seamount series of La Palma/Canary Islands, *J. Geophys. Res.*, **89**(B13), 11,195–11,215.

Staudigel, H., Koppers, A. A. P., Lavelle, J. W., Pitcher, T. J., & Shank, T. M., 2010. Box 1: Defining the word "seamount", *Oceanography*, **23**(1), 20–21.

Stein, S. & Gordon, R. G., 1984. Statistical tests of additional plate boundaries from plate motion inversions, *Earth Planet. Sci. Lett.*, **69**, 401–412.

Steinberger, B., 2000. Plumes in a convecting mantle: Models and observations for individual hotspots, *J. Geophys. Res.*, **105**, 11,127–11,152.

Stern, R. J., 2002. Subduction zones, *Rev. Geophys.*, **40**(4), 1012.

Stocks, K., 2005. SeamountsOnline: an online information system for seamount biology, http://seamounts.sdsc.edu.

Talwani, M. & Ewing, M., 1960. Rapid computation of gravitational attraction of three-dimensional bodies of arbitrary shape, *Geophysics*, **25**, 203–225.

Tatsumi, Y., 2005. The subduction factory: How it operates in the evolving Earth, *GSA Today*, **15**(7), 4–10.

Tsai, C.-L. & McQuarrie, A. D. R., 1999. *Regression and time series model selection*, World Scientific Publishing Co., Singapore, 1st edn.

Van Wyckhouse, R. J., 1973. Synthetic bathymetric profiling system (SYNBAPS), Tech. Rep. TR 233, U.S. Natl. Oceanogr. Office.

Vogt, P. R., 1974. Volcano height and plate thickness, *Earth Planet. Sci. Lett.*, **23**, 337–348.

Vogt, P. R. & Jung, W.-Y., 2000. GOMaP: A matchless resolution to start the new millennium, *Eos Trans. AGU*, **81**(23), 254, 258.

Walcott, R. I., 1970. Flexural rigidity, thickness, and viscosity of the lithosphere, *J. Geophys. Res.*, **75**, 3941–3953.

Watts, A. B., 1978. An analysis of isostasy in the world's oceans, 1, Hawaiian-Emperor seamount chain, *J. Geophys. Res.*, **83**(B12), 5989–6004.

Watts, A. B., 2001. *Isostasy and Flexure of the Lithosphere*, Cambridge Univ. Press, London, 1st edn.

Watts, A. B., Cochran, J. R., & Selzer, G., 1975. Gravity anomalies and flexure of the lithosphere: A three-dimensional study of the Great Meteor Seamount, northeast Atlantic, *J. Geophys. Res.*, **80**(11), 1391–1398.

Watts, A. B., Pierce, C., Collier, J., Dalwood, R., Canales, J. P., & Henstock, T. J., 1997. A seismic study of lithospheric flexure in the vicinity of Tenerife, Canary Islands, *Earth Planet. Sci. Lett.*, **146**, 431–447.

Watts, A. B., Sandwell, D. T., Smith, W. H. F., & Wessel, P., 2006. Global gravity, bathymetry, and the distribution of submarine volcanism through space and time, *J. Geophys. Res.*, **111**, B08408, doi:10.1029/2005JB004083.

Weigel, W. & Grevemeyer, I., 1999. The Great Meteor seamount: seismic structure of a submerged intraplate volcano, *J. Geodyn.*, **28**, 27–40.

Wessel, P., 1992. Thermal stresses and the bimodal distribution of elastic thickness estimates of the ocean lithosphere, *J. Geophys. Res.*, **97**(B10), 14,177–14,193.

Wessel, P., 1993. A reexamination of the flexural deformation beneath the Hawaiian Islands, *J. Geophys. Res.*, **98**(B7), 12,177–12,190.

Wessel, P., 1996. Analytic solutions for 3-D flexural deformation of semi-infinite elastic plates, *Geophys. J. Int.*, **124**, 907–918.

Wessel, P., 1997. Sizes and ages of seamounts using remote sensing: Implications for intraplate volcanism, *Science*, **277**(5327), 802–805.

Wessel, P., 1998. An empirical method for optimal robust regional-residual separation of geophysical data, *J. Math. Geol.*, **30**(4), 391–408.

Wessel, P., 2001. Global distribution of seamounts inferred from gridded Geosat/ERS-1 altimetry, *J. Geophys. Res.*, **106**(B9), 19,431–19,441.

Wessel, P., 2007. Seamount characteristics, in *Seamounts: Ecology, Fisheries and Conservation*, pp. 3–25, eds Pitcher, T. J., Morato, T., Hart, P. J. B., Clark, M. R., Haggan, N., & Santos, R. S., Blackwell, Oxford, UK.

Wessel, P. & Chandler, M. T., 2010. The spatial and temporal distribution of marine geophysical surveys, *Acta Geophysica.*, **in press**, doi:10.2478/s11600–010–0038–1.

Wessel, P. & Kroenke, L. W., 1997. Relocating Pacific hot spots and refining absolute plate motions using a new geometric technique, *Nature*, **387**, 365–369.

Wessel, P. & Lyons, S., 1997. Distribution of large pacific seamounts from Geosat/ERS-1: Implications for the history of intraplate volcanism, *J. Geophys. Res.*, **102**(B10), 22,459–22,476.

Wessel, P., Sandwell, D. T., & Kim, S.-S., 2010. The global seamount census, *Oceanography*, **23**(1), 24–33.

White, S. M., 2005. Seamounts, in *Encyclopedia of Geology*, vol. 4, pp. 475–484, eds Selley, R. C., Cocks, L. R., & Plimer, I. R., Elsevier, Oxford.

White, S. M., Umino, S., & Kumagai, H., 2006. Transition from seamount chain to intraplate volcanic ridge at the East Pacific Rise, *Geology*, **34**(4), 293–296.

Wolfe, C. J. & McNutt, M. K., 1991. Compensation of Cretaceous seamounts of the Darwin Rise, northwest Pacific ocean, *J. Geophys. Res.*, **96**(B2), 2363–2374.